Development of Alkaline Fuel Cell Gas Diffusion Cathodes using new Substrate Materials

A thesis submitted for the degree of doctor of philosophy of Imperial College London.

By

Fabrice Bidault

March 2010



Fuel Cell Group
Department of Earth Science and Engineering
Imperial College London

Abstract

Hydrogen, as a clean and renewable fuel, may play a key role in the near future because of the increasing cost of fossil fuels and the impact of CO_2 on the climate. Fuel cells are electrochemical devices which directly convert chemical energy stored in hydrogen into electrical energy at high efficiency with only water and heat as by-products.

A leading candidate fuel cell technology for operation on hydrogen fuels is the proton exchange membrane fuel cell (PEMFC). But today its commercialization remains limited, mainly because of the price of the materials used for electrode manufacture. Catalysts based on precious metals such as platinum, which are currently inherent to PEMFCs, preclude inexpensive mass production. In contrast an alternate fuel cell technology well suited to hydrogen fuels, the alkaline fuel cell (AFC), offers the potential for low cost, mass producible fuel cells, without the need for platinum based catalysts, but has received less attention in recent years.

The aim of this work is to develop AFC gas diffusion cathodes using new substrate materials (nickel foam and porous silver membranes) which ally mechanical support, current collection and catalyst support so as to reduce the cost of the electrode. Silver, which is one of the most active materials for the oxygen reduction reaction (ORR) and which is 100 times cheaper than platinum, has been used as the catalyst in this work. The effect of optimising the cathode performance has been monitored using DC polarization curves and electrochemical impedance spectroscopy.

Both the nickel foam and porous silver membrane substrates have been successfully developed as the gas diffusion medium in aqueous alkaline media. Silver plated nickel foam showed a decrease in both the Ohmic and charge transfer resistance compared to uncoated nickel foam, leading to improved performance. The porous silver membrane showed good performance in a passive air-breathing cell (50 mW cm^{-2} at 25 ^{o}C) due to its high surface area and optimised hydrophobic properties.

Acknowledgements

Firstly, I would like to thank in a general manner all my supervisors; Prof. Nigel Brandon, Dr. Dan Brett, Prof. Hugh Middleton and Prof. Anthony Kucernak for their support, advice and guidance throughout the course of this work.

I would like to thank Prof. Hugh Middleton as the first one believing in me and for encouraging me to do a Ph.D.

I would also like to thank Nicholas Abson for introducing me to the world of alkaline fuel cells.

I am greatly obliged to Prof. Nigel Brandon who has been so supportive when I lost my funding and without whom I would have not continued this work. Nigel is a true gentleman and will stay in my mind as a model.

I am very grateful to Dr. Dan Brett who has been so helpful and patient with my French accent. I must say that I have never met someone with such a big heart. I will never forget our pub sessions…

I feel very lucky to work with Prof. Anthony Kucernak with whom I learn a lot about electrochemistry and I wish that our future collaboration would be successful.

I must express my gratitude to people from Diverse Energy with whom I have worked for two years.

To all the members of the Fuel Cell Group, especially Paul, Denis, Michael and of course Mardit, thanks for sharing ideas, thoughts, time and beers.

I also must thank my family and friends back in Paris for their support. I know that they been worried for me but finally everything worked out.

Finally, I would like to dedicate this thesis to my father which has been the source of my motivation. I would not have done half of what I have accomplished today without him. I wish he could have seen me today…

Dedicated to the memory of my father
Guy Bidault

Table of Contents

Abstract……2

Acknowledgements……..3

Table of Contents……6

List of Figures……..……11

List of Tables……16

Dissemination……17

Introduction.....18

1. Fuel cell principles……....20

1.1. Abstract……..…...20

1.2. Introduction to fuel cells……...20

1.2.1.What is a fuel cell?.....20
1.2.2.Fuel cell advantages/disadvantages……..…..20
1.2.3.Fuel cell types……....21
1.2.4.Basic fuel cell construction and operation……..…22
1.2.5.Fuel cell performance……..…25

1.3. Fuel cell thermodynamics……..……..27

1.3.1.Reversible open circuit voltage (OCV)…….....27
1.3.2.Reversible voltage variation with temperature……..29
1.3.3.Reversible voltage variation with pressure and concentration……..……...29
1.3.4.Fuel cell efficiency……..…..30
1.3.4.1 Ideal fuel cell efficiency……31
1.3.4.2 Real fuel cell efficiency……31

1.4. Fuel cell voltage losses……...…….32

1.4.1.Fuel cell reaction kinetics…….…….32
1.4.2.Fuel cell charge transport……..……35
1.4.3.Fuel cell mass transport…….36

1.5. Conclusions……..……37

1.6. References……38

2. Review of gas diffusion cathodes for alkaline Fuel cells….39

2.1. Abstract……..……39

2.2. Introduction……....39

2.3. AFC technical review…….…41

2.4. AFC gas diffusion cathode…….....46

2.4.1. Electrode design……46
2.4.2. Materials used in electrode fabrication……..…..48
2.4.3. Operational mechanism…….....….50
2.4.4. Electrode modelling…….....51
2.4.5. Electrode fabrication…….....53
2.4.6. Oxygen reduction reaction (ORR) in alkaline Media.....54
2.4.7. Cathode catalyst materials……56
2.4.7.1. Noble metal catalyst……..57
2.4.7.2. Non-noble metal catalyst……...58
2.4.8. Performance……..……61
2.4.9. Electrode durability…….…..……63
2.4.9.1. CO_2 effect…….…….63
2.4.9.2. Corrosion effect…….64
2.4.9.3. Weeping and flooding effects……64

2.5. Conclusions……..……...65

2.6. References……..….66

3. Experimental procedures and characterisation techniques…75

3.1. Abstract ……..……75

3.2. General electrochemistry……75

3.3. Test rig setup for nickel substrate cathodes……76

3.4. Testing cell for porous silver membrane cathodes…….…80

3.5. Electrochemical impedance spectroscopy (EIS) technique…….……...81

3.6. Other characterization techniques……...84

3.7. References……...……86

4. Development of a cathode using nickel foam as a substrate material.....87

4.1. Abstract……..……..…87

4.2. Introduction…….87

4.3. Experimental……...89

4.3.1. Electrode preparation…….……...89
4.3.2. Electrode characterization…….……92

4.4. Results and discussion……..……..92

4.4.1. Nickel mesh vs. nickel foam……92
4.4.2. Characterization of nickel foam……94
4.4.3. Characterization of silver plated nickel foam……..95
4.4.4. Characterization of fuel cell gas diffusion cathodes……100

4.5. Conclusions……104

4.6. References……105

5. Effet of an additional active layer on cathode performance using nickel foam as a substrate material .... ……108

5.1. Abstract ……108

5.2. Introduction……108

5.3. Experimental……108
5.3.1. Electrode preparation……108

5.4. Results and discussion……110

5.4.1. Cathode performance and optimization……110
5.4.2. Electrochemical impedance spectroscopy study….115

5.5. Conclusions……119

5.6. References……120

6. A Novel Cathode for Alkaline Fuel Cells based on a Porous Silver Membrane……121

6.1. Abstract……121

6.2. Introduction……121

6.3. Experimental……123

6.3.1. Electrode preparation……..123
6.3.2. Electrode characterization……...124
6.3.3. Fuel cell operation…….……..124

6.4. Results and discussion…….….125

6.4.1. Characterization of silver membranes…….125
6.4.2. Characterization of silver membranes cathodes…..126
6.4.3. Assessment of performance under different Conditions…… 131
6.4.4. Optimisation of PTFE loading……136
6.4.5. Testing membranes within a fuel cell…….…...143

6.5. Conclusions……...146

6.6. References…….147

7. Conclusions and future work……...148

List of Figures

Figure 1.1: Basic fuel cell construction……...24

Figure 1.2: Typical low temperature fuel cell I-V curve…….26

Figure 1.3: Plot of the Butler-Volmer equation……..34

Figure 2.1: Diagram showing the fundamentals of an alkaline fuel cell…….41

Figure 2.2: Schematic of a circulating electrolyte alkaline system…….44

Figure 2.3: Picture of a monopolar Zetek stack (University of Agder)……..…45

Figure 2.4: Evolution in AFC system performance: H2/air performance is shown as solid lines and H2/O2 performance is shown as dashed lines …...……..46

Figure 2.5: Design of a double layer electrode for a bipolar stack design……..47

Figure 2.6: Schematic illustration of the carbon macro and micro structure within the active layer…….……..51

Figure 2.7: Schematic illustration of the 'flooded agglomerate' model……..52

Figure 2.8: Electrode fabrication: The rolling method……54

Figure 2.9: TEM photograph for reduced carbon-supported silver nanoparticles…..58

Figure 3.1: Schematic illustration of the test assembly for half-cell measurements: (a) cross section and (b) front view……...76

.

Figure 3.2: Picture of the circulating electrolyte test rig…….77

Figure 3.3: Flow diagram of the circulating electrolyte test rig.....78

Figure 3.4: Effect of KOH flow rate on Cath4 performance.....79

Figure 3.5: Effect of air flow rate on Cath4 performance.....79

Figure 3.6: Three-compartment electrochemical cell……..80

Figure 3.7: Fuel cell testing set up.....81

Figure 3.8: Schematic illustration of the Nyquist plot……82

Figure 3.9: Equivalent circuit: the Randles circuit……..84

Figure 3.10: Schematic drawing of the SEM……..……....85

Figure 4.1: Scanning electron microscope image showing the open structure of the nickel foam……..……..90

Figure 4.2: Amount of deposited silver as a function of electroplating time in the heavy bath (plating conditions 2 V, 5.8 A)……..91

Figure 4.3: Polarization curves of nickel foam and nickel mesh in aerated 32 wt% KOH solution…….……..92

Figure 4.4: Impedance diagram of nickel foam and nickel mesh in aerated 32 wt% KOH solution at 0.6 V (cell voltage) frequency range 10 kHz to 0.01 Hz…….….93

Figure 4.5: Equivalent circuit of the nickel mesh and foam electrode for the impedance spectra……93

Figure 4.6: SEM pictures of (a) the Ni foam surface and (b) the Ni foam surface after silver plating (Silver loading: 11 mg cm^{-2})……..95

Figure 4.7: XRD of nickel foam (bottom) and silver plated nickel foam (top)……..95

Figure 4.8: Cyclic voltammogram for UPD formation of Pb on nickel foam, υ = 1 mV s^{-1}; 12 mM Pb $(NO_3)_2$ and 100 mM HCl solution……96

Figure 4.9: Cyclic voltammogram for UPD formation of Pb/Ag on silver plated nickel foam (silver loading: 11 mg cm^{-2}), υ = 1 mV s^{-1}; 12 mM $Pb(NO_3)_2$ and 100 mM HCl solution……96

Figure 4.10: Current-voltage lines showing the electrical resistivity of the uncoated nickel foam, and the silver plated nickel foam with different silver loadings…….97

Figure 4.11: Effect of silver loading on the electrochemical performance of nickel foam in aerated 32 wt. % KOH solution……..98

Figure 4.12: SEM pictures of the Ni foam surface after silver plating (Silver loading: 6.5 mg cm^{-2}).....98

Figure 4.13: Comparison between the EIS response for nickel foam and silver plated nickel foam (11 mg cm^{-2}) at 0.6 V (cell voltage) in 32 wt. % KOH solution from 10 kHz to 0.01 Hz……..……...99

Figure 4.14: Polarization curves of cathodes made of nickel foam and silver plated nickel foam (loading: 11 mg cm^{-2}) under air at 25°C in 32 wt. % KOH solution….100

Figure 4.15: Impedance measurements over a range of electrode voltages of a cathode made of silver plated nickel foam (loading: 11 mg cm^{-2}) under air at 25°C in 32 wt. % KOH solution from 10 kHz to 0.01 Hz……...…101

Figure 4.16: Impedance measurements over a range of electrode voltages of a cathode made of nickel foam under air at 25°C in 32 wt. % KOH solution from 10 kHz to 0.01 Hz……..……..103

Figure 4.17: Comparison between the EIS response from the nickel foam and silver plated nickel foam based cathodes at 0.6 V (cell voltage) from 10 kHz to 0.01 Hz……...104

Figure 5.1: Scheme of the new cathode design using nickel foam as the substrate……..110

Figure 5.2: Polarization curves showing performance of Cath0 and Cath2 with air in 30 wt. % KOH solution at different temperatures. Inset: potential vs. log current density at high potential…….111

Figure 5.3: Polarization curves showing improved performance of Cath2 by optimization of the GDL thickness under air in 30 wt. % KOH solution……..112

Figure 5.4: Polarization curves showing the improved performance of the different cathode generation under air at 25°C in 30 wt. % KOH solution……..113

Figure 5.5: Polarization curves showing the performance of Cath3 after 1 and 50 hrs of operation as well as the operation of improved Cath3 containing a higher hydrophobic composition after 200 hours on air at 25°C in 30 wt. % KOH solution…….……..114

Figure 5.6: Polarization curves showing the reproducibility of the performance of Cath2 under air at 20°C in 30 wt. % KOH solution…….……..…115

Figure 5.7: Impedance measurements of Cath4 under air and oxygen at 25°C in 30 wt. % KOH solution at 0.9 V (cell voltage) from 10 kHz to 0.01 Hz……116

Figure 5.8: Impedance measurements of Cath4 under air at 25°C in 30 wt. % KOH solution at different cell voltages from 10 kHz to 0.01 Hz……....116

Figure 5.9: Impedance measurements of Cath4 under air at 25°C in different KOH concentration solutions at 0.9 V from 10 kHz to 0.01 Hz (symbol: experimental, line: fitting)…….……117

Figure 5.10: Equivalent circuit used to fit the high and low frequency semi-circles observed for Cath4…….....118

Figure 6.1: a) Optical Image of silver membranes; Scanning electron microscope image showing the porous structure of silver membranes without (b) and with PTFE (c)……123

Figure 6.2: Polarization curves and impedance results for cathodes made of silver membrane (1.2 μm) with and without PTFE (12.3 mg cm^{-2} total amount deposited) under oxygen at 20°C in 30 wt. % KOH solution. (a). Polarisation results; (b) Impedance measurements at 0.8 V (cell voltage) from 10 kHz to 0.1 Hz. Inset is the same plot scaled to show the details of the scans at low Z…….……127

Figure 6.3: Polarization curves (a) and impedance measurements (b) of cathodes made of silver membranes with different pore sizes under air at 20°C in 30 wt. % KOH solution…….……129

Figure 6.4: Current density at 0.70 and 0.80 V (a) [Data taken from Fig. 6.3(a)]; and PTFE loading (b) as a function of membrane pore size for a consistently applied PTFE treatment……...…131

Figure 6.5: Impedance measurements of silver membrane cathode (1.2 μm) at 20°C in 30 wt. % KOH solution from 10 kHz to 0.1 Hz. (a) Nyquist plot at 0.8 V showing the effect of reactant - oxygen and air ; (b) Bode phase-plot spectra under oxygen showing the effect of polarisation potential……...132

Figure 6.6: Impedance measurements of silver membrane cathode (1.2 μm) under oxygen at 20°C in different KOH concentration solutions at 0.8 V (cell voltage) from 10 kHz to 0.1 Hz.....133

Figure 6.7: Equivalent circuit of the silver membrane cathode used to fit both the high frequency and low semi-circles……..133

Figure 6.8: Bode plot spectrum of silver membrane cathode (1.2 μm) under oxygen at different temperature in 30 wt. % KOH solution at 0.8 V (cell voltage) from 10 kHz to 0.1
Hz.....135

Figure 6.9: Cartoon showing the deposition of PTFE on the silver membrane and how this may affect wetting of the electrolyte. The first PTFE layer is deposited throughout the entire membrane structure whereas the second deposition occurs only on the surface. The catalytically active area immediately beneath the outer PTFE layer is highlighted…….…….136

Figure 6.10: Effect of first PTFE deposition step on silver membrane performance under oxygen at 20°C in 30 wt. % KOH solution. No second PTFE deposition step was performed. (a) Polarization curve showing pore size effect for constant PTFE loading from the first deposition step (b) Polarization curves for 0.8 μm silver membranes showing the effect of the PTFE loading from the first deposition step; (c) impedance spectra for the membranes in (b) obtained at at 0.8 V (cell voltage) from 10 kHz to 0.1 Hz……...……..138

Figure 6.11: Performance of silver membranes after optimised first and second PTFE deposition steps. Polarization curves showing optimised 0.8 μm and 1.2 μm pore electrodes and for comparison a 0.8 μm pore size electrode with only the optimised first ptfe loading, (a). Electrochemical impedance results for cathodes made of silver membranes (0.8 and 1.2 μm) under oxygen at 20°C in 30 wt. % KOH solution, (b). Impedance data obtained at 0.8 V, from 10 kHz to 0.1 Hz (symbol: experimental data, line: fit). Total PTFE loadings are displayed for each electrode (first PTFE deposition step leads to a loading of 4.2±0.1 mg cm^{-2})…….…..140

Figure 6.12: Current density decay at different half cell voltages of a cathode made of silver membrane (0.8 μm, PTFE: 5.25 mg cm^{-2}) under oxygen at 20°C in 30 wt. % KOH solution.....142

Figure 6.13: Equivalent circuit parameters fitted from impedance measurement of a silver membrane cathode (0.8 μm, PTFE: 5.25 mg cm^{-2}) under oxygen at 20°C in 30 wt. % KOH solution from 10 kHz to 0.1 Hz.....143

Figure 6.14: (a) Half-cell polarization curves of cathodes made of silver membrane (0.8 μm) and silver membrane with 10 nm of Pt (20 μg cm^{-2}) under oxygen at 20°C. Inset – Electrochemical Impedance spectroscopy of each electrode at 0.90 V from 10 kHz to 0.1 Hz. (b) Hydrogen-air fuel cell test of silver membrane with 10 nm of Pt (21 μg cm^{-2}) utilising 30 wt. % KOH solution as electrolyte and 1 mm electrode separation. Pt on carbon paper (0.4 mg cm^{-2}) used as anode. For comparison, the same cathode operating under half-cell operation in the same cell is shown……..…144

List of Tables

Table 1.1: Different type of fuel cells.....22

Table 2.1: Cathode performance using different catalysts with O_2.....61

Table 2.2: Cathode performance using different catalysts with air.....62

Table 4.1: Weight and price comparison of nickel mesh and nickel foam.....88

Table 4.2: Silver electroplating conditions.....91

Table 4.3: Values of equivalent circuit parameters for nickel foam and nickel mesh.....94

Table 4.4: Key characteristics of the nickel foam at 20°C.....94

Table 4.5: Values of equivalent circuit parameters for nickel foam and silver plated nickel foam (11 mg cm^{-2}).....99

Table 5.1: Composition and performances of each kind of cathode.....110

Table 5.2: Fitted values of equivalent circuit parameters of the Cath4 impedance spectra in different KOH concentration.....119

Table 6.1: Key characteristics of silver membranes.....126

Table 6.2: Fitted values of equivalent circuit parameters of the high frequency semi-circle for silver membrane cathode in different KOH concentration.....134

Table 6.3: Fitted values of equivalent circuit parameters (Fig. 6.6) for curves in Fig. 6.9(b).....141

Table 6.4: Estimates of the electrode surface area and double layer capacitance from Impedance data in Fig. 6.9.....141

Dissemination

Refereed journal papers:

2005 Study of porous silicon nanostructures as hydrogen reservoirs
V. Lysenko, F. Bidault, S. Alekseev, V. Zaitsev and D. Barbier
Journal of Physical Chemistry B 109 (2005) 19711-19718

2009 Review of gas diffusion cathodes for alkaline fuel cells
F. Bidault, D.J.L. Brett, P.H. Middleton and N.P. Brandon
Journal of Power Sources 187 (2009) 39-48

2009 A new application for nickel foam in alkaline fuel cells
F. Bidault, D.J.L. Brett, P.H. Middleton, N.Abson and N.P. Brandon
International Journal of Hydrogen Energy 34 (2009) 6799-6808

2010 Novel Cathode for Alkaline Fuel Cells based on a Porous Silver Membrane
F. Bidault and A. Kucernak
Journal of Power Sources 195 (2010) 2549-2556

2010 An improved cathode for alkaline fuel cells
F. Bidault, D.J.L. Brett, P.H. Middleton, N.Abson and N.P. Brandon
International Journal of Hydrogen Energy 35 (2010) 1783-1788.

Conference paper:

2008 A New Cathode Design for Alkaline Fuel Cells
F. Bidault, D.J.L. Brett, P.H. Middleton and N.P. Brandon
Fundamentals and Developments of Fuel Cells (Nancy/France)

Poster presentation:

2009 New catalysts support for alkaline fuel cell
F. Bidault, D.J.L. Brett, P.H. Middleton and N.P. Brandon
European Fuel Cell Forum (Lucerne/Switzerland)

Introduction

Today, the commercialization of low temperature fuel cells is mainly limited because of the price of the materials incorporated in electrode manufacture. Catalyst materials, which are necessary for the reactions to occur, are the biggest part of this cost. For Proton Exchange Membrane Fuel Cells (PEMFCs), noble metal catalysts such as platinum are essential to obtain good performance but they preclude inexpensive mass production. In contrast Alkaline Fuel Cells (AFCs), in which reaction kinetics are more facile, enable the use of alternative catalyst materials such as silver, manganese oxide, perovskyte and spinel oxides..., these materials being much cheaper than the platinum group metals required in acidic media. The use of KOH solution as the electrolyte, and the possibility to build the stack in a monopolar configuration (eliminating the need for expensive bipolar plates) further strengthen the potential for AFCs to be a low cost and mass producible fuel cell technology.

In general, AFC electrodes consist of several PTFE-bonded carbon-black layers deposited onto a substrate material. This substrate material should fulfil different functions such as high permeability to gases, high structural strength, good corrosion resistance and high electronic conductivity. In a monopolar design, it also serves as the current collector, so metal screens and meshes usually made of nickel have been generally used. Recently, new mass production techniques have made nickel foam more attractive because it has become cheaper than the commonly used nickel mesh.

The physical properties of reticulated metal foam are very well suited to their use in fuel cells. They possess high surface area, high electronic conductivity, high thermal conductivity and very low resistance to fluid flow. Metal foam is flexible, easily cut and malleable, light weight (low density) and is becoming increasingly cost effective. Nickel foam was also chosen as a promising electrode matrix in this study because of the possibility of using electroplating to apply the catalyst which is an easy and inexpensive processing route to the manufacture of electrodes, and lends itself to mass production.

The main objective of this work is the development of AFC gas diffusion cathodes, using nickel foam as a substrate material, which ally mechanical support, current collection and catalyst support so as to reduce the cost of the electrode. The choice of materials and techniques to fabricate the electrode is to be low cost, and enable scale up using standard production techniques such as the rolling machine method to apply the different layers onto the substrate. The aim of each step of the development is to maximise current density and minimise voltage drop, whilst avoiding the use of expensive materials and manufacturing steps. The ultimate goal is to develop a low cost, mass producible cathode for a circulating alkaline fuel cell which can be used in both bipolar and monopolar stacks.

Another objective of this work is the development of cathodes using porous silver membranes as substrate materials, linking electrode performance to structural properties such as mean porosity, pore size, and surface area. The effect of the wettability of the electrode structure on performance is also important and is therefore considered. Through improved understanding of this relativle simple electrode design, this study aims to develop improved understanding of the more complex electrode structures often found in commercial AFCs.

Chapter 1: Fuel Cell Principles

1.1. Abstract

In this chapter, a short introduction to fuel cell technology is given where advantages and drawbacks are listed. The different fuel cell types are briefly described. The basic fuel cell construction is explained. Thermodynamic principals are given where it is shown how ideal potentials (alongside efficiencies) can be calculated, knowing temperature, pressure and reactant concentration. Finally, it is explained how irreversibilities, which cause voltage drop, occur. Finally the irreversibilities leading to voltage drops in performance are explained.

1.2. Introduction to fuel cells

1.2.1. What is a fuel cell?

A fuel cell is an electrochemical device which converts chemical energy into electrical energy. While a combustion engine converts chemical energy via heat into useful mechanical work, a fuel cell converts chemical energy stored in fuels directly into electrical energy, providing power generation with high efficiency. Electricity is produced as long as raw materials (fuel/oxidant) are supplied, which is the main difference between a fuel cell and a battery.

1.2.2. Fuel cell advantages/disadvantages

The fundamental fuel cell advantages are listed below:

- High operating efficiency for power plants scalable to a range of sizes
- If hydrogen is used as fuel, pollution emissions are strictly a result of the production process of the hydrogen.

- No moving parts, with the exception of pumps, compressors and blowers to drive the fuel and oxidant (usually air).
- Multiple choices of potential fuel feedstock, from existing petroleum, natural gas, or coal reserves to renewable ethanol or biomass hydrogen production.
- Near instantaneous 'recharge' capability compared to batteries.

However, technical limitations of fuel cell systems remain to be overcome:

- Fuel cell component cost must be reduced via the development of mass production technology to compare with actual power plants (~$30/kW for automotive applications and ~$1000/kW for stationary applications [1]).
- Suitable reliability and durability of fuel cell and system components must be achieved (5500 h for automotive and 40,000 h for stationary applications [1]).
- Suitable system power density must be achieved (650 W/kg for automotive (50 kW) applications, 150 W/kg for auxiliary (5-10 kW) applications and 100 W/kg for portable (milliwatt to 50 W) applications [1]).
- Storage, generation and delivery of hydrogen technology must be improved if pure hydrogen is to be used.

1.2.3. Fuel cell types

A number of fuel cells have been developed which can be differentiated by their electrolyte. For instance, a solid oxide fuel cell (SOFC) uses ceramic oxides as the electrolyte while a proton exchange membrane fuel cell (PEMFC) uses a solid proton conducting polymer. Fuel cells can also differ in terms of fuel used (e.g., hydrogen PEMFC or direct methanol PEMFC) or operating temperature (Table 1.1). Whereas low temperature fuel cells such as alkaline fuel cells (AFC) and PEMFC have the advantages of faster start-up and higher efficiency (using hydrogen as fuel), slow reaction rates occur, which must be addressed by using costly catalysts and sophisticated electrode designs. High temperature fuel cells such as the SOFC achieve high reaction rate without expensive catalysts and moreover, natural gas which is 'internally reformed' can be used directly within the fuel cell without the need for a

separate unit. SOFCs address many of the problems related to fuel cells; however, the ceramic materials used in the cell fabrication can be difficult to handle and expensive to manufacture. The system to run the SOFC is also more complex and not easy to start up compare with low temperature fuel cell systems [1].

Fuel cell type	**Electrolyte Charge carrier**	**Catalyst**	**Operating temperature**	**Fuel Compatibility**	**Primary Contaminant**
PEMFC (Proton Exchange Membrane)	Solid polymer membrane H^+	Platinum	50-100 ^oC	H_2, methanol	CO, Sulphur and NH_3
AFC (Alkaline)	KOH Solution OH^-	Platinum Silver Nickel	50-250 ^oC	H_2	CO, CO_2 and sulphur
PAFC (Phosphoric Acid)	H_3PO_4 solution H^+	Platinum	150-210 ^oC	H_2	CO <1%, sulphur
MCFC (Molten Carbonate)	Molten Carbonate CO_3^{2-}	Nickel	650-800 ^oC	H_2, CH_4	Sulphur
SOFC (Solid Oxide)	Ceramic O_2^-	Nickel Perovskites	500-1000 ^oC	H_2, CH_4, CO	Sulphur

Table 1.1: Different type of fuel cells [1].

1.2.4. Basic fuel cell construction and operation

In a fuel cell, hydrogen is electrochemically oxidized at the anode, which produces electrons. Conversely oxygen is supplied to the cathode, usually in the form of air, where it is reduced to ultimately form product water. These reactions have a finite rate and occur at the interfacial area where the electrode, the gas, and the electrolyte meet, i.e. at the so-called three phase boundary (TPB). This interfacial area is scalable; the

larger the surface area or interfacial area the larger the current produced at a given electrode overpotential. To provide large reaction surfaces, fuel cells are commonly made into planar structures with morphologies tailored with high porosity and/or surface roughness, as shown in Fig. 1.1. The basic structure of a fuel cell consists of a thin electrolyte layer in contact with electrodes on either side, both in contact with bipolar plates.

In the case of low temperature fuel cells with hydrogen as fuel, the hydrogen oxidation reaction (HOR) occurs, which liberates electrons as shown in Equation (1.1):

$$H_2 \rightarrow 2H^+ + 2e^- \quad (1.1)$$

Electrons produced at the anode (negative terminal), flow across the external circuit to the cathode (positive terminal), where the oxygen reduction reaction occurs as shown in Equation (1.2):

$$O_2 + 4e^- + 4H^+ \rightarrow 2H_2O \quad (1.2)$$

The overall reaction (1.3) produces water and heat as by-products.

$$H_2 + 1/2O_2 \rightarrow H_2O \quad (1.3)$$

The ionic conduction of the H^+ is ensured by the electrolyte, which is especially engineered for this purpose. The acidic fuel cell is taken here as an example but the operation with other fuel cell types works similarly taking into account their respective charge carriers.

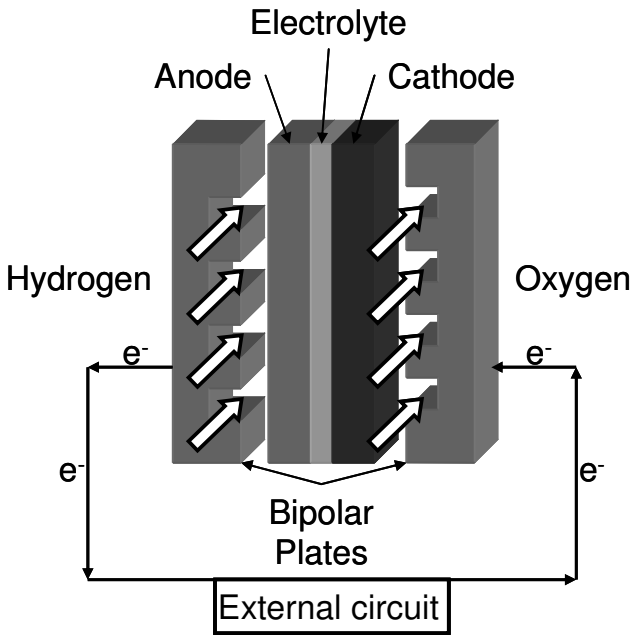


Figure 1.1: Basic fuel cell construction.

The voltage of a single cell when under load i.e, when useful current is drawn, is about 0.7 V. Thus, cells have to be connected in series in order to increase the voltage to a practical level, This interconnection of cells is called a 'stack' and is performed usually by means of bipolar plates which are placed between the cathode of one cell and the anode of the following cell. The bipolar plate has to be especially designed to provide the gas for both electrodes and to make good electronic contact with the electrodes. Flow channels are machined (or formed) on both sides of the bipolar plate, which is commonly made of graphite (especially for PEM) or stainless steel (especially fro AFC). For a series stack, the current is proportional to the active surface area of the electrode and is the same for all cells in the stack. The stack voltage is the sum of each component cell voltage. Conversely, for an array of cells connected in parallel, the current is additive and the voltage is the same in each cell. In some configurations a combination of series connected and parallel connected modules in used, particularly in some designs of AFCs.

1.2.5. Fuel cell performance

The performance of a fuel cell is closely dependent on the ability of the fuel and oxygen to react on the catalytic surfaces of their respective electrodes at the TPB. The magnitude of the TPB is very dependent on the morphology and microstructure of the electrode. The reaction rate is proportional to the electrode active surface area. The high porosity of the materials used (e.g., carbon black) greatly increases the effective surface area of the electrode and thus its performance. In addition to the surface area, the incorporation of catalysts into the electrode further increases the rate of the reaction. The microstructure of the electrode should incorporate sufficient porosity to achieve adequate gas diffusion. The electrolyte and electrode conductivity also play an important part in determining fuel cell performance [2].

A commonly used indicator of the fuel cell performance is the current-voltage (*I-V*) characteristic curve which displays current on the x-axis and voltage on the y-axis. It should be noted that the current is usually normalized by the geometric active area of the electrode (giving a current density) in order to compare results from electrodes with different surface areas. A complementary power curve is often plotted alongside the I-V curve. An example of an *I-V* curve for a typical low temperature fuel cell is given Fig.1.2. The theoretical voltage of the fuel cell, which can be calculated by thermodynamic considerations, is a function of the Gibb's free energy of the overall reaction; however, in practise the voltage of the fuel cell is less than the predicted voltage due to irreversible losses. As can be seen, the more current that is produced the lower the voltage of the cell, limiting the total power that can be delivered. The current supplied by a fuel cell is directly proportional to the amount of fuel consumed; therefore, the decrease of the fuel cell voltage also decreases the electric power per unit of fuel. Thus, the fuel cell voltage can be seen as a measure of the fuel cell efficiency. The higher the voltage at a given current density the better. The point of maximum power is often used as an indicator of the outright performance of the fuel cell [2].

Three key areas can be noticed in Fig. 1.2. A brief description is as follows:

- Activation region: There is initially an exponential decrease of voltage with increasing current which corresponds to activation losses (η_{act}) associated with the electrokinetics of the reactions occurring at the electrode surfaces.
- Ohmic region: At higher current densities there is a linear voltage fall which is related to Ohmic losses (η_{ohmic}) caused by the resistance to the flow of electrons through the electrode and interconnects, as well as the resistance to the flow of ions through the electrolyte. This is the region that the normal operating point lays.
- Mass transport region: There is a final rapid drop in the voltage at higher current density which is related to the mass transport or concentration losses (η_{conc}) caused by the change in concentration of the reactant and the failure to transport it sufficiently quickly to the electrode surface.

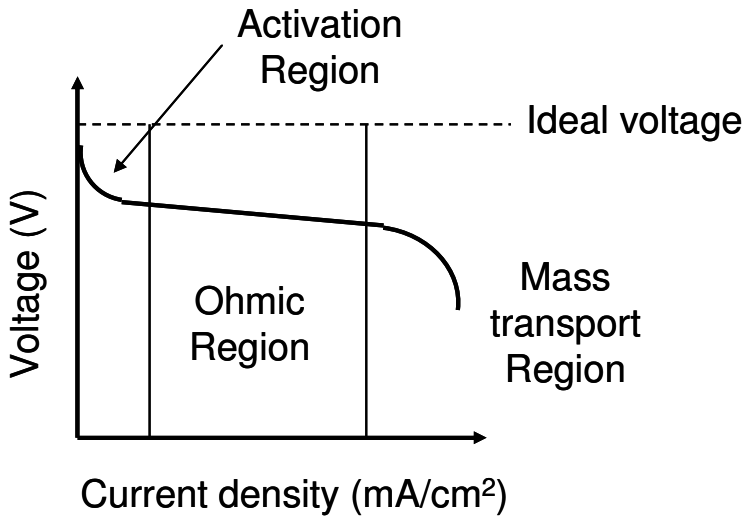


Figure 1.2: Typical low temperature fuel cell *I-V* curve [2].

The real voltage (V) of a fuel cell can be written by subtracting all the voltage losses from the thermodynamically predicted voltage (E_{thermo}) as follows:

$$V = E_{thermo} - \eta_{act} - \eta_{ohmic} - \eta_{conc} \quad (1.4)$$

1.3. Fuel Cell Thermodynamics

Thermodynamics determine the operation of a fuel cell on a given fuel and at a given temperature and pressure. The potential and direction of the reaction can be predicted but not its rate, which is the domain of chemical kinetics.

1.3.1. Reversible open circuit voltage (OCV)

The basic thermodynamic quantity that determines how much work any system can do on its surroundings is the change in free energy, normally referred to as the `Gibbs Free Energy`. For fuel cells, the change in the 'Gibbs free energy' (G) is an important concept which can be defined as the 'energy available or released to do external work' [2]. The Gibbs equation relates the basic thermodynamic quantities as follows:

$$\Delta G = \Delta H - T\Delta S \tag{1.5}$$

Where ΔG=change in free energy. ΔH=change in reaction enthalpy and ΔS is the change in reaction entropy.

It is usual to consider the 'Gibbs free energy of reaction' (G_r) rather than Gibbs free energy when working with chemical reaction at standard temperature and pressure (p = 1atm, a = 1, T = 298K, denoted by the superscript symbol ^{o}). It is also more convenient to consider these quantities in the molar form which is represented by a bar over the corresponding term $\bar{X}$. The change of the Gibbs free energy of reaction is the difference between the Gibbs free energy of reaction of the products and the Gibbs free energy of reaction of the reactants as follows:

$$\Delta \bar{G}_r = \bar{G}_r \text{ of products} - \bar{G}_r \text{ of reactants} \tag{1.6}$$

So the value of the Gibbs free energy of reaction for the fuel cell reaction can be calculated based on Eq. 1.7 as follows:

$$\Delta \bar{G}_r = (\bar{G}_r)_{H2O} - (\bar{G}_r)_{H2} - 1/2(\bar{G}_r)_{O2} \tag{1.7}$$

The convention in thermodynamics means that for a spontaneous process the free energy term will be a negative quantity. The value of the Gibbs free energy of reaction changes with temperature and state (liquid/gas) of the water product and in the case of the fuel cell reaction, the negative sign means that energy is released- in the form of electrical power. If we consider the fuel cell process as 'reversible' (no losses), all the Gibbs free energy of reaction is converted into electrical energy following Eq.1.8; we can then determine the reversible OCV of the fuel cell.

$$W_{\text{elec}} = - \Delta \bar{G}_r \tag{1.8}$$

The electrical work done by moving a charge Q (Coulomb) through an electrical potential difference E (volt) is:

$$W_{\text{elec}} = E\,Q \tag{1.9}$$

With:
$$Q = n\,F \tag{1.10}$$

Where n is the number of moles of electrons transferred and F is Faraday's constant.

$$\Delta \bar{G}_r = - n\,F\,E \tag{1.11}$$

The Gibbs free energy of reaction for the hydrogen-oxygen fuel cell reaction is -237 kJ/mol (under standard conditions, i.e. liquid water produced). For each molecule of hydrogen used one molecule of water is produced and two electrons pass through the external circuit [2]. Thus, the reversible voltage (E^{o}) for this reaction is 1.23 V using the following equation:

$$E^{o} = - \Delta \bar{G}_r / n\,F \tag{1.12}$$

1.3.2. Reversible voltage variation with temperature

E_T, which we define as the reversible cell voltage at the temperature T, can be calculated with the following equation [2]:

$$E_T = E^o + (\Delta \bar{S}^o / n\,F)(T\text{-}T_o) \tag{1.13}$$

For fuel cells running on hydrogen, the theoretical EMF will actually decrease as the temperature increases, so for example a PEM fuel cell running on hydrogen at 25 °C will exhibit an EMF of around 1.23V whereas a solid oxide fuel cell running at 1000 °C will exhibit an EMF closer to 1.0 V. Despite this, the performance of the fuel cell at higher temperature can easily exceed the performance at lower temperature because the reactions kinetic are faster.

1.3.3. Reversible voltage variation with pressure and reactant concentration

The Gibbs free energy of formation varies with temperature but also with reactant pressure and concentration. If we consider a general reaction such as:

$$bB + cC \rightarrow dD + fF \tag{1.14}$$

where B and C are reactants, D and F are products, and b, c, d, and f represent the stoichiometric coefficients for B, C, D and F respectively. The Gibbs free of energy of reaction is given by:

$$\Delta \bar{G}_r = \Delta \bar{G}_r^o + RT \ln (a_D^{\,d} \,.\, a_F^{\,f} / a_B^{\,b} \,.\, a_C^{\,c}) \tag{1.15}$$

where a_I^i is the activity of the species *I* raised to the power of its stoichiometric coefficient (i) and *R* is the ideal gas constant. Utilising the overall stoichiometric equation (eqn 1.3) applied to the hydrogen-oxygen fuel cell, we thus obtain:

$$\Delta \bar{G}_r = \Delta \bar{G}_r^o + RT \ln (a_{H2O} / a_{H2} \,.\, a_{O2}^{1/2}) \qquad (1.16)$$

Combining Equation (1.12) with Equation (1.16), we obtain the Nernst equation for the fuel cell reaction [3]:

$$E = E^o - RT/2F \ln (a_{H2O} / a_{H2} \,.\, a_{O2}^{1/2}) \qquad (1.17)$$

The Nernst equation shows how the reversible voltage varies as a function of species activity. The Nernst equation can also be expressed as a function of gas pressure by replacing activities by their equivalent partial pressures measured in bar; if we consider the partial pressure of the water as unity which is the case if the fuel cell is operated below 100°C, the equation is then:

$$E = E^o - RT/2F \ln (1 / p_{H2} \,.\, p_{O2}^{1/2}) \qquad (1.18)$$

1.3.4. Fuel cell efficiency

Fuel cells are not subjected to the Carnot efficiency limit as are heat engines, because the chemical energy is directly converted to electrical energy without any requirements for volume, pressure or temperature change [3]. If T_1 is the maximum temperature of the heat engine, and T_2 the temperature of the heated fluid released, then the maximum efficiency of a heat engine is:

$$\text{Carnot limit} = (T_1 - T_2) / T_1 \qquad (1.19)$$

1.3.4.1. Ideal fuel cell efficiency

For fuel cells, the reversible efficiency of the conversion process is the ratio of the maximum energy available to do work (ΔG) and the total energy of the overall reaction (ΔH), which is given by Equation (1.20):

$$\varepsilon = \Delta \bar{G}_r \; / \; \Delta \bar{H}_r \qquad (1.20)$$

Where, $\Delta \bar{H}_r$ is the enthalpy of reaction.

Two different values of $\Delta \bar{H}_r$ can be used depending on the product water state. If water is in the form of steam, $\Delta \bar{H}_r$ = -241.83 kJ mol^{-1} and if water is in the form of a liquid then $\Delta \bar{H}_r$ = -285.84 kJ mol^{-1}. The latter figure is called the higher heating value (HHV) and the former one, the lower heating value (LHV). The difference in the two values is due to the latent heat of vaporization of water. The use of HHV and LHV are common in fuel cell specifications and care should be exerted in their interpretation depending on the temperature of operation of the fuel cell [3].

1.3.4.2. Real fuel cell efficiency

The practical fuel cell efficiency is always less than the ideal one because of voltage and fuel utilization losses. The real fuel cell efficiency can be calculated with the following formula based on the thermodynamic efficiency, but multiplied by coefficients representing voltage losses and fuel utilisation of less than 100%

$$\varepsilon_{\text{real}} = (\Delta \bar{G}_r \; / \; \Delta \bar{H}_r \;) \, (V/E) \, ((i/nF)/ \, \upsilon_{\text{fuel}} \;) \qquad (1.21)$$

Where V is the real operating voltage, E is the reversible voltage, i is the current generated and υ_{fuel} is the rate at which fuel is supplied (mol sec^{-1}).

The first term is the ideal efficiency as seen in the previous section, the second is the voltage efficiency which incorporates irreversible losses and the third is the fuel utilization efficiency which accounts for the fact that not all the fuel provided is converted to electricity.

1.4. Fuel cell voltage losses

The real voltage of the fuel cell is usually very different to the ideal voltage due to irreversibilities which cause voltage drops as outlined in section 1.2.5. Three major losses occur: Activation losses, which are related to reaction kinetics, Ohmic losses, which are related to charge transport, and concentration losses, which relate to mass transport.

1.4.1. Fuel cell reaction kinetics

Fuel cell reaction kinetics involves the electrochemical reactions and charge transfer steps associated with both the anode and cathode reactions. Depending on the conditions and type of fuel cell the kinetic at one of the electrodes, usually the cathode, exerts the overall control. The basic theoretical understanding of the fuel cell reactions is the same as that applied to electrochemical redox processes and the mathematical treatment is identical. The only specific difference is that the working fuel cell comprises of two complementary charge transfer processes – the anodic oxidation of the fuel e.g. hydrogen and the cathodic reduction of oxygen. In order to fully understand how the fuel cell works, it is necessary to understand the individual electrode reactions, and in order to do this we generally split the cell into its two respective electrodes and study each one separately in a convectional electrochemical setup using working, counter and reference electrodes. A fuller explanation of how this was carried out in this thesis is given in the experimental section. However, in this part we re-visit the basic electrochemical theory to give grounding for the experiments presented in later chapters.

As far as fuel cell performance in concerned, the part of the *I-V* cure that exhibits what is termed activation control ie pure electrochemical control is observed in the portion of the *I-V* curve close to the OCV. It is characterised by a perceptible exponential form which is an embodiment of the exponential variation of current with potential. The basic theory is given below. From a practical point of view, the fuel cell performance is only high if the charge transfer kinetics is fast. This generally means that a highly active electrode is required with suitable catalysts incorporated in the structure. If neither of these conductions is satisfied then the I-V cure will rapidly decrease to an unacceptably low value even if all the other controlling factors such as ohmic loss and mass transport are deemed adequate.

Electrochemical reactions result in the transfer of electrons, the rate of which constitutes the measured electrical current. The study of the mechanisms by which electron transfer processes occur is fundamental to the understanding of how to improve fuel cell performance. Electrochemical reaction rates are proportional to the effective reaction surface area (related to the TPB distribution), but are very sensitive to the activation energy for the rate determining step. A part of the available cell voltage has to be used to overcome the activation barrier if current is to be produced. This voltage loss is called the activation overvoltage (η_{act}). The relationship between current flux and overpotential under purely activation control is given by the Butler-Volmer (equation 1.22) [4] where the first term represents the anode contribution (blue curve in Fig. 1.3) and the second term represents the cathode contribution (green curve in Fig. 1.3); the sum of the two terms giving the full function (yellow curve in Fig. 1.3):

$$j = j_o[\exp(\alpha nF\eta_{act}/RT) - \exp\text{-}((1\text{-}\alpha)nF\eta_{act}/RT)] \qquad (1.22)$$

where j is the current density, and j_o is the exchange current density. α is the charge transfer coefficient; it expresses how the change in the electrical potential changes the rate of an electrochemical reaction. For most electrochemical reactions, α ranges from 0.2 to 0.5.

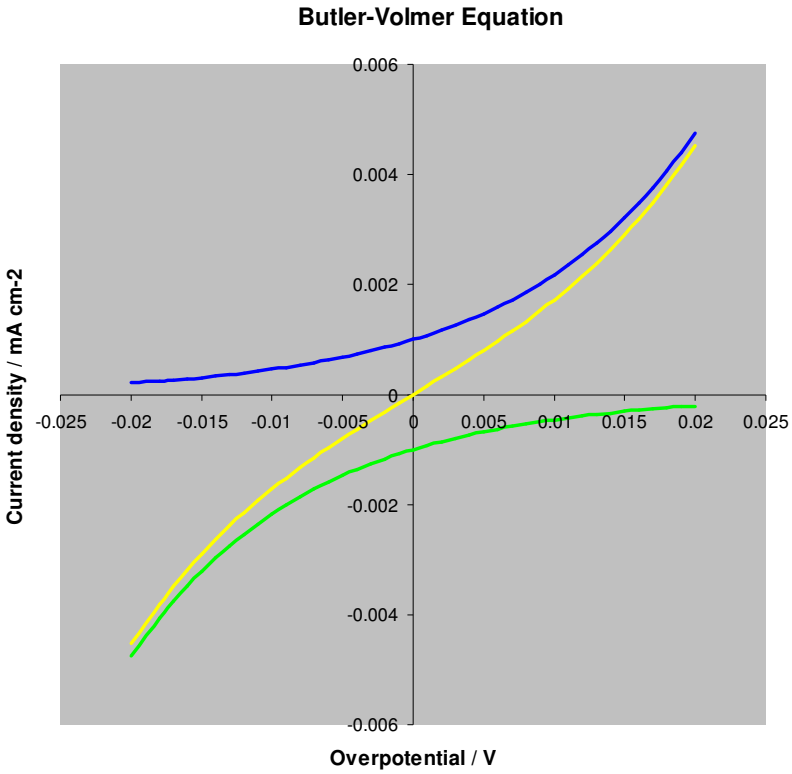


Figure 1.3: Plot of the Butler-Volmer equation.

The exchange current density (j_o) is a measure of the reaction rate at equilibrium condition between reactants and products in the absence of an activation overvoltage. A high value of j_o means a facile reaction and thus a high reaction rate at low overpotentials. It is then crucial to increase j_o in order to maximise the electrode performance. It can be accomplished by: i) increasing reactant concentration, ii) increasing reaction temperature, iii) decreasing the activation barrier (catalysts), and iv) increasing the number of reaction sites.

When η_{act} is large (> 50-100 mV), the Butler-Volmer equation can be simplified to the Tafel equation [4]:

$$\eta_{act} = 2.303(RT/\alpha nF) \log_{10} (j/j_o) \qquad (1.23)$$

If a graph of overvoltage (η) against log of current density is plotted (Tafel plot), from the slope and intercept of the linear fit to this plot, j_o and α can be calculated.

1.4.2. Fuel cell charge transport

The term “fuel cell charge transport” has been adopted by fuel cell investigators to mean the flux of electron and ion within their respective conducting phases, such as the electrolyte for the ions and the electrodes for the electrons. This is in distinction to the term “fuel cell charge transfer“, which is synonymous with electrode kinetics- as outlined above.

Charge transport, which includes both electrons and ions in an electrochemical reaction, is driven by the voltage gradient developed across the conductive phase. Generally the energy to drive the flux of current through a phase of uniform composition is a linear function i.e, voltage is proportional to current. In electrochemical systems, such as fuel cells, the voltage used to drive charge transport represents a loss which obeys Ohm’s law (Ohmic loss: η_{ohmic}):

$$V = i\,R \tag{1.24}$$

Generally the Ohmic resistance of a component material is determined from its resistivity which is often provided from data sheets or technical specifications of the material. The resistivity ρ of a sample of component material with a regular geometry is given by the relationship:

$$\rho = R\,A/l \tag{1.25}$$

Where R = resistance in Ω, ρ = resistivity in Ω cm, l is the thickness of the sample and A is the geometrical surface area of the specimen. It is often convenient to use the reciprocal quantities conductivity and conductance.

Often the specific resistance or area resistance of the sample material is used in modelling work, in which case the units are Ω cm^2. This form of representation is particularly useful for describing the resistance of large but thin electrodes where the thickness is difficult to measure with precision.

The total voltage loss in the fuel cell stack due to charge transport is the summation of all Ohmic contributions including the electrodes, the electrolyte membranes, the bi-polar plates and the end plates used for current collection.

Ionic conductance is generally orders of magnitude lower than electronic conducting materials, especially in metals. Even in mixed conductors, the electronic contributions can easily dominate over the ionic contribution. The reason for this is that the mobility of the electron is very high compared to any ionic species. In the case of ions, motilities are generally low which means that significant conductance can only be achieved if the concentration of ions is high e.g. 32% KOH for a liquid alkaline fuel cell.

The situation for the electrodes can be relaxed if they are made from metallic materials such as nickel, in which case the electrode thickness can be in the mm range. This allows the electrode to be a structural component as well as a functional component.

For a well constructed fuel cell, the ionic conductivity is by generally the main source of Ohmic loss, being in general four to eight orders of magnitude lower than the electronic conductivity. There are three ways to reduce the Ohmic resistance: i) the use of highly conductive electrodes, ii) the use of highly conductive materials in well designed bipolar plates, and iii) making the electrolyte as thin as possible.

1.4.3. Fuel cell mass transport

Mass transport, which includes the supply and removal of reactant and products, leads to a loss in fuel cell performance due to reactant depletion. Mass transport in the electrode is dominated by diffusion, whereas it is dominated by convection in flow channels. At high current densities, the diffusive character of the electrode, which is structure sensitive, leads to a limiting current density (j_L) where the reactant concentration falls to zero in the active layer. Thus, j_L is the maximum current density that can be reached by the electrode. It can be calculated from the following equation:

$$j_L = n\,F\,D^{eff}\,(C_R / \delta) \qquad (1.26)$$

where D^{eff} is the effective reactant diffusivity within the active layer, C_R is the flow channel reactant concentration, and δ is the diffusion layer thickness.

As can be seen from Equation (1.26), j_L can be maximized by ensuring a high C_R (related to bipolar plate design) and by ensuring that D^{eff} is large and δ is small (related to electrode structure).

1.5. Conclusions

A fuel cell is an electrochemical device which directly converts chemical energy into electrical energy with high efficiency. Different type of fuel cells exist which can be classified by their operating temperature and electrolyte materials; alkaline fuel cells are a type of low temperature fuel cell. Fuel cell performance is directly related to the processes occurring at the interface between electrodes and electrolyte. The higher the surface area, the higher the performance. Maximum fuel cell performance means maximised three phase boundary density, where reactant gas, electrolyte and catalyst meet. In low temperature fuel cells, high performance is only achieved when active catalysts are incorporated in the structure of the electrodes.

Fuel cell operation under reversible conditions can be described by the overall cell reaction which is a function of the temperature, pressure and species concentration. In practice high performance comes with a cost – voltage and therefore energy is lost by virtue of unavoidable internal resistance and by the finite rate at which fuel and other reactants can be supplied. These losses are termed irreversible in the sense that they are not part of the thermodynamic picture. Three major irreversible losses occur: Activation losses, which are related to reaction kinetics, Ohmic losses, which are related to charge transport, and concentration losses, which relate to mass transport.

It is fundamental to understand how a fuel cell works, and therefore how voltage losses occur, in order to formulate and improve electrode performance. In this thesis, the recording of *I-V* curves and the use of the electrochemical impedance spectroscopy technique, which will be described in Chapter 3, have formed the major basis of the investigation of electrode performance and behaviour.

1.6. References

[1] EG&G Technical Services; Fuel Cell Handbook (Seventh edition). U.S Department of Energy (2004).

[2] R. O'hayre, S-W Cha, W. Colella, F. B. Prinz; Fuel Cell Fundamentals. John Wiley & Sons: New York (2006).

[3] J. Larminie, A. Dicks; Fuel Cell Systems Explained (Second edition). John Wiley & Sons: New York (2003).

[4] M. M. Mench; Fuel Cell Engines. John Wiley & Sons: New York (2008).

Chapter 2: Review of Gas Diffusion Cathodes for Alkaline Fuel Cells

2.1. Abstract

This chapter gives a technical background to alkaline fuel cells (AFCs), introducing the advantages and drawbacks of the technology. AFCs offer the potential for low cost, mass producible fuel cells, without the dependency on platinum based catalysts and (currently) expensive membrane electrolytes. The AFC uses relatively low cost electrolytes utilising aqueous bases such as potassium hydroxide. The inherent CO_2 sensitivity of the electrolyte can be addressed by filtering out the CO_2 from the air intake using a simple scrubber and periodically replacing the liquid electrolyte.

A review of the state-of-the-art in gas diffusion cathode development is given. The overall cell performance and stability is dominated by the behaviour of the cathode, leading to a focus of research effort on cathode development. The performance and durability of the gas diffusion electrode is very much dependent on the way in which the layer structures are fabricated from carbon and polytetrafluoroethylene (PTFE). The choice and treatment of the carbon support is of prime importance for the final catalytic activity. Noble metal and non-noble metal catalysts have been investigated and show good performance; however, more work is still needed on cathode durability to ensure the long term success of the alkaline fuel cell.

2.2. Introduction

Alkaline fuel cells (AFCs) were the first practical working fuel cell following the pioneering work of Bacon [1]. AFCs can realise a high overall electrical efficiency greater than most other fuel cell types [2]. Recently, a system consisting of a 6 kW stack connected to the grid showed an efficiency between 50 and 60% (LHV) [3]. The AFC was developed and studied extensively throughout the 1960s to the 1980s [4], prior to the emergence of the proton exchange membrane fuel cell (PEMFC), which has subsequently attracted most of the attention from developers. However, primarily because the predicted cost reduction in PEMFCs remains problematic, a resurgence of

interest in AFCs has occurred in recent years [5-9]. The utilisation of non-noble metal catalysts and liquid electrolyte makes the AFC a potentially low cost technology compared to PEMFCs, which employ platinum catalysts and specially engineered electrolyte materials. Cost analyses have shown that ambient air AFC systems, for mobile and low power applications, are less expensive than ambient air PEMFC systems, and that AFCs still have the potential of major improvements with modest investment [10, 11].

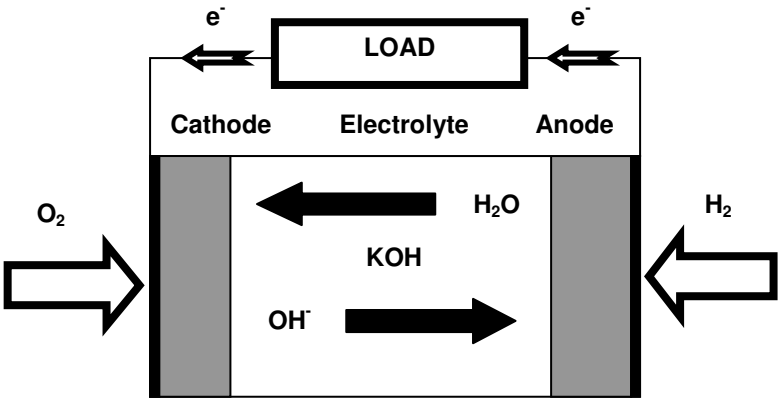
Historically, four different types of AFC cells have been developed and a description of each has been given by Gulzow [10]. These can be summarised as follows: (i) cells with free liquid electrolyte, (ii) cells with liquid electrolyte in the pore-system, (iii) matrix cells where the electrolyte is fixed in the electrode matrix, and (iv) falling film cells. The one common aspect of these cells is that they all use porous electrode architectures which are similar to the electrode used in metal air batteries [12]. More recently, the alkaline anion-exchange membrane (AAEM) has attracted increasing attention [13-15]. The feasibility of a AAEM direct methanol fuel cell has been discussed, taking into account the thermodynamic disadvantage induced by the pH difference across the membrane, and kinetic advantages; it was concluded that the technology was worth further study [16]. The development of AAEM fuel cells have several important advantages over conventional AFCs: (i) since there is no mobile cation there is no precipitated carbonate, (ii) no electrolyte weeping, (iii) reduced methanol crossover, (iv) potentially simplified water management, due to the fact that the water is produced at the anode and consumed at the cathode, (v) a larger repertoire of effective catalyst materials, and (vi) potentially reduced corrosion [17]. However, while the AAEM fuel cell holds great promise, developments still need to be made to achieve suitably conducting and stable membranes.

The anode electrode for AFCs has been less studied than the cathode, where catalysts containing platinum-group metals such as Pt/Pd have shown good performance and stability [18, 19]. Nickel has also been studied as a potential low cost catalyst for AFCs anodes [20, 21]. Raney nickel, which offers the advantage of high surface area, has been shown to be one of the most active catalysts for the hydrogen oxidation reaction in alkaline media, but has been reported to suffer from deactivation [22-24], which could be improved by the addition of copper [25] or treatment with H_2O_2 [26].

The power output and lifetime of alkaline fuel cells are directly linked to the behaviour of the cathode, where most of the polarization losses occur. This is because the oxygen reduction reaction (ORR) is a slow reaction compared with hydrogen oxidation reaction at the anode. As a consequence, cathode development requires special attention to find the best catalyst and electrode structure to combine performance and stability. After a brief technology background, this review focuses on the state-of-the-art gas diffusion cathode materials and designs used with circulating electrolyte AFCs.

2.3. AFC technical review

In an alkaline fuel cell (Fig. 2.1), hydroxyl ions are produced at the cathode and migrate to the anode side where they react with hydrogen. Some of the water formed at the anode diffuses to the cathode and reacts with oxygen to form hydroxyl ions in a continuous process. The overall reaction produces water and heat as by-products and generates four electrons per mole of oxygen, which travel via an external circuit producing the electrical current.



Cathode: $O_2 + 2H_2O + 4e^- \rightarrow 4OH^-$

Anode: $2H_2 + 4OH^- \rightarrow 4H_2O + 4e^-$

Overall: $O_2 + 2H_2 \rightarrow 2H_2O$

Figure 2.1: Diagram showing the fundamentals of an alkaline fuel cell.

The use of a non-noble metal catalyst is possible because the oxygen reduction reaction (ORR) in alkaline media is more facile than in acid media. As a consequence, higher voltages at a given current density can be obtained, leading to a higher electrical efficiency [4].

The main disadvantage of AFCs is that carbon dioxide can react with the electrolyte to form carbonate (Eq.2.1), decreasing the electrolyte conductivity, oxygen solubility and electrode activity. The formation of precipitated carbonate (Eq.2.2) can also lead to the blockage of the electrolyte pathways and electrode pores.

$$CO_2 + 2OH^- \rightarrow CO_3^{2-} + H_2O \quad (2.1)$$

$$CO_3^{2-} + 2K^+ \rightarrow K_2CO_3 \quad (2.2)$$

Potassium hydroxide solution (KOH) is almost exclusively used as the electrolyte because it has a higher ionic conductivity than sodium hydroxide solution, and potassium carbonate has a higher solubility product that sodium hydroxide, which renders the former less likely to precipitate [27].

In most terrestrial applications, the KOH electrolyte is circulated through the stack, which has some advantages over the alternative immobilized systems which have been favoured in space applications such as Apollo and the Space shuttle. The use of a circulating electrolyte allows thermal and water management to be easily controlled. Moreover, impurities (e.g. carbon from electrodes or carbonates) can be easily removed, making the circulating electrolyte systems less sensitive to CO_2 poisoning than the immobilized electrolyte systems. The OH^- concentration gradient is also greatly decreased and the build up of gas bubbles in the gap between the electrodes minimized [28]. However, electrolyte leakage and parasitic losses are challenging problems and need to be carefully considered by developers. The main advantage of the immobilised systems is the simplicity of construction and the ready removal of product water from the hydrogen side of the system. However, such systems are very

prone to degradation of the electrolyte due to impurities, and require very pure hydrogen and oxygen to function reliably. Because of this, they are ideally suited for space applications where tanked hydrogen and oxygen are used for propulsion.

As a consequence of the CO_2 sensitivity, AFCs have tended to be demonstrated in special applications where pure hydrogen and pure oxygen are provided, such as space. In such systems the KOH electrolyte has been immobilized in a matrix constructed from thin asbestos sheets. Asbestos is the preferred material in this application due to its exceptional stability and absorption properties. The use of a porous matrix, soaked with KOH, which allows the elimination of moving parts, was developed by NASA. Bacon's invention of the double-layer sintered electrode made from nickel powder was the starting point of this technology, which led to its use as the electrical power source in the Apollo missions to the Moon and later in the shuttle Orbiter. The Orbiter fuel cell system, which operated at 4 atmospheres and 95 °C, was manufactured by United Technologies Corp, (UTC) Fuel Cells. The system has given impressive performance up to 470 mA cm^{-2} at 0.88 V. However, in order to achieve this performance, the electrodes required a high noble metal loading of 10 mg cm^{-2} at the anode (80% Pt-20% Pd), and 20 mg cm^{-2} at the cathode (90% Au-10% Pt) [29].

Alkaline fuel cells were the first fuel cell technology to be put into mobile applications through its demonstration as the power source for a farm tractor in the late 1950s by Allis Chalmers. Union Carbide Corp. (UCC) developed circulating electrolyte systems leading to the demonstration of Kordesch's Austin A 40 fuel cell car for several years on public roads in the early 1970s [4, 30].

In more recent years, AFC companies such as Zetek [31, 32] focused on the design of circulating electrolyte low temperature unpressurised systems for backup power, stationary and mobile applications. The aim was to achieve a low cost mass production fuel cell. Injection-moulded plastic frames (usually polypropylene), which house the electrodes, were used to build the stack. Each frame was friction welded to the next to ensure that the stack was leak-free. Low cost electrode production was ensured by the use of standard industrial processes such as rolling (calendaring) and pressing.

The electrolyte of choice for terrestrial applications running on air and industrial grade hydrogen is 30-40 % KOH, circulated though the stack with a pump. This has the advantage of allowing easy replacement when CO_2 absorption has reached an unacceptably high level. Moreover, circulating electrolytes provides a very effective way of cooling the stack and heat recovery via a heat exchanger. The system is designed to be as simple as possible as outlined in (Fig. 2.2).

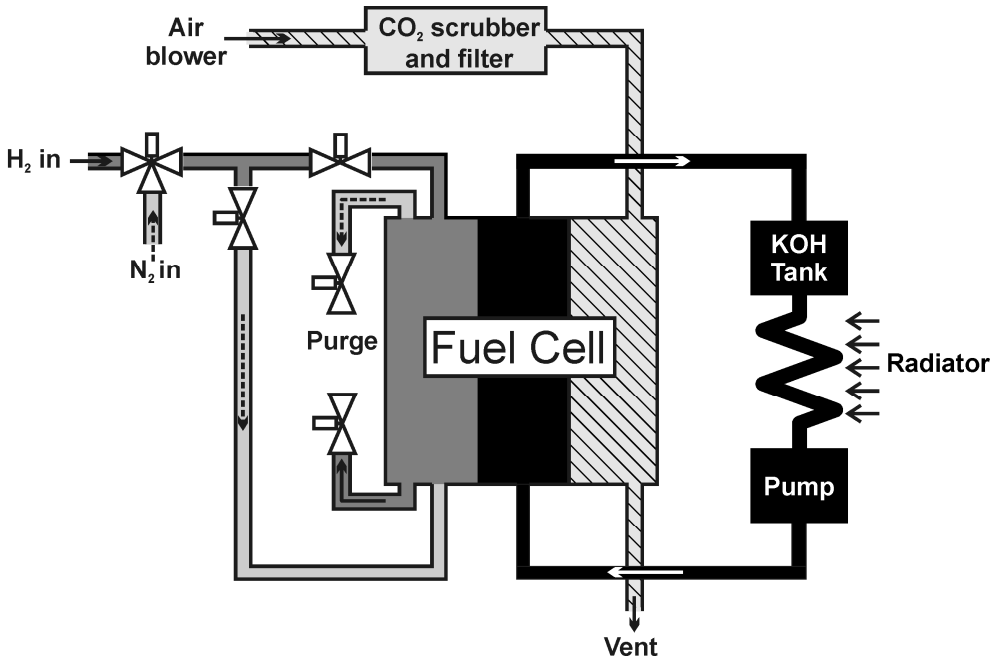


Figure 2.2: Schematic of a circulating electrolyte alkaline system.

The electrolyte circulation loop consists of a KOH tank, a KOH pump and a heat exchanger. During start up the KOH is heated to the desired operating temperature, typically 70 °C. During operation the heat exchanger is used to remove excess heat. This can be recovered for space heating applications. An air blower forces air into a CO_2 scrubber (usually containing soda lime), from where the air is directed to the air-intake. McLean estimates the cost of the scrubbing using soda lime between 0.2-2.6 Dollar cents/kWh [10]. The outlet air is directly exhausted to the atmosphere whereas the hydrogen is re-circulated or dead ended for maximum efficiency. The hydrogen circulation is achieved by means of a jet pump which facilitates the evacuation of the excess water that is collected in a water trap. The start-up/shut-down procedure is quick and easily performed by means of a nitrogen purge [32-34].

Both monopolar [31, 32] and bipolar stack designs [6, 34] have been demonstrated. The monopolar stack design (Fig. 2.3) presents several advantages: (i) low cost due to the avoidance of expensive bipolar plates, (ii) stack thickness decreases as there is only one gas chamber between two electrode, (iii) no mechanical pressure is required because cells are usually glued or welded, (iv) modularity of the power delivered by changing the external current connectors and (v) the disconnection of a bad cell facilitates maintenance of the stack [28]. However, the monopolar design is limited to a current density of up to 100 mA cm^{-2} due to the losses associated with current collection on the side of each electrode. By contrast, the bipolar design demonstrates a uniform current density over all of the electrode surface and higher terminal voltage with less power limitation, and is therefore the preferred geometry for high power applications [34].

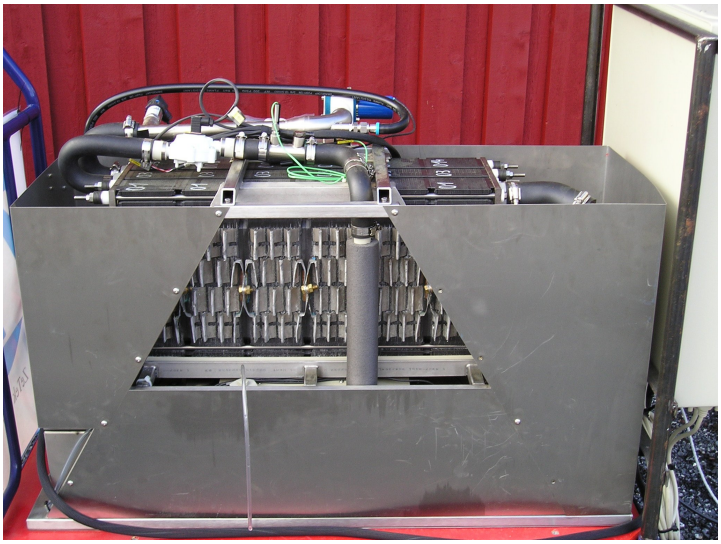


Figure 2.3: Picture of a monopolar Zetek stack (University of Agder).

Typical AFC performance obtained at different temperature and pressure are given in Fig. 2.4.

A 20,000 h life time of accumulated module operation has been achieved by Siemens using a Ni-anode and Ag-cathode [33] and 15,000 h with a shorter stack than usually used in the Space-Shuttle by UTC [2]; however, this performance data was obtained with pure oxygen and hydrogen. When air is supplied to the system, even with

scrubbing a large part of the CO_2, lifetime is much less. A stack made by Zevco has been reported to have delivered power for 5,000 h using low platinum loading and a circulating electrolyte system [32]. Insufficient studies have been done to date and the durability of AFC systems remains a key issue, especially when using non-noble metal catalysts and air.

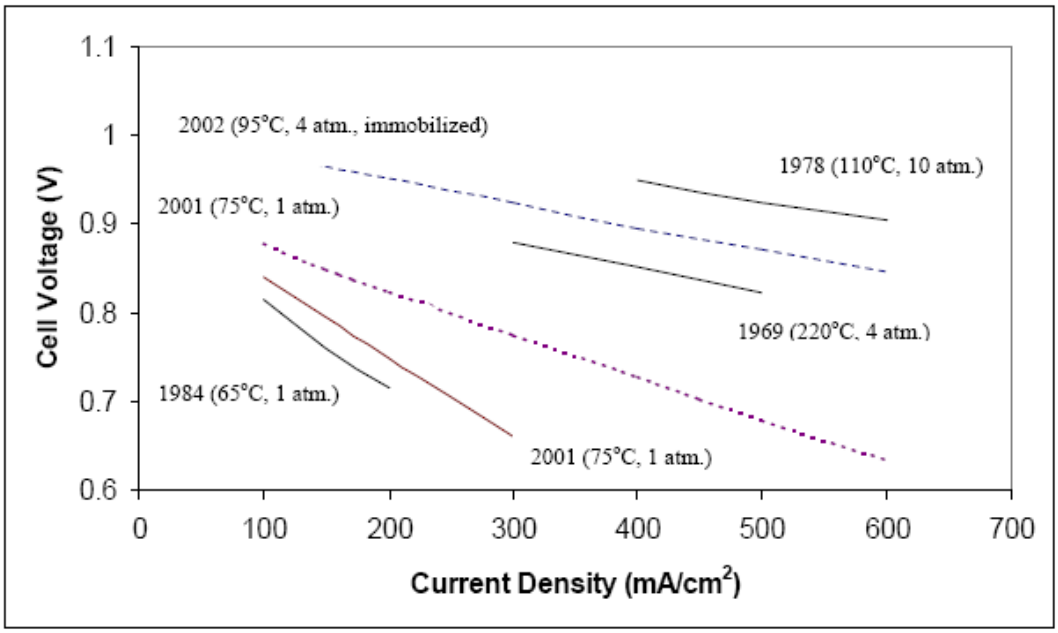


Figure 2.4: Evolution in AFC system performance: H_2/air performance is shown as solid lines and H_2/O_2 performance is shown as dashed lines [29].

2.4. AFC gas diffusion cathode

2.4.1. Electrode design

In general, AFC electrodes consist of several PTFE-bonded carbon-black layers, which fulfil different functions. The double-layer electrode structure shown schematically in Fig. 2.5, consists of a backing material (BM), a gas diffusion layer (GDL) and an active layer (AL). This design is preferentially used over single layer electrodes [35]. More complex electrode designs with more than three layers have been reported; for example, two different GDLs on top of each other and an AL; however, such geometries are rare [28].

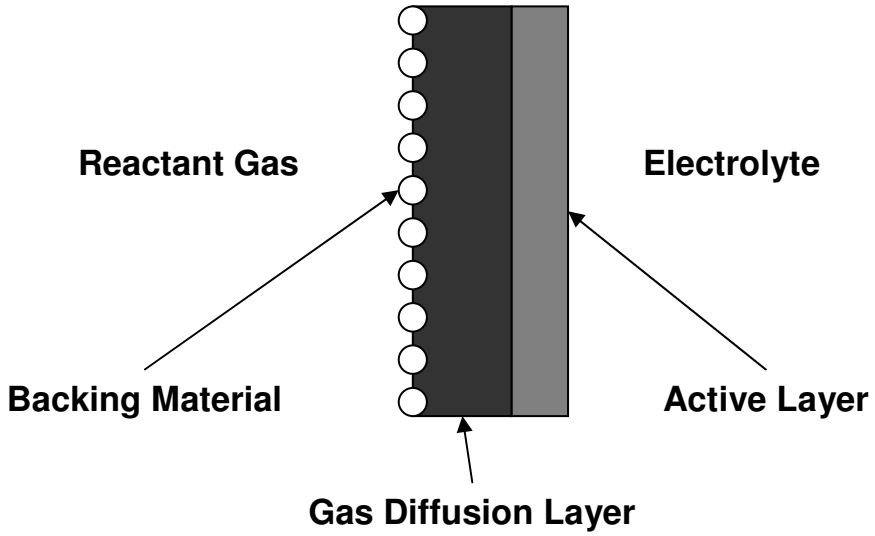


Figure 2.5: Design of a double layer electrode for a bipolar stack design.

The BM should have a high permeability to gases, high structural strength, good corrosion resistance and high electronic conductivity. In a monopolar design, the BM serves as the current collector, so metal screens, meshes or foams, usually made of nickel, are generally used. In bipolar designs, the BM is in direct contact with the bipolar plate. This means the BM can also be made of carbon cloth or porous carbon paper in a similar way to the design of PEM fuel cells [34].

The GDL supplies the reactant gas to the AL and prevents the liquid electrolyte from passing through the electrode. This effect is often termed 'weeping'. Monopolar designs almost exclusively use a GDL made from porous PTFE. The porosity is achieved by mixing the PTFE suspension with sugar or ammonium carbonate. When sintered at elevated temperature, the ammonium carbonate filler decomposes, producing gas bubbles which create porosity in the PTFE film [36]. Bipolar designs require a GDL that is electronically conducting. This precludes using pure PTFE and instead favours mixtures of PTFE with conducting carbon support [37]. The ratio of carbon / PTFE (25-60% PTFE) is a trade-off between the level of hydrophobic behaviour of the PTFE and the conductivity of the carbon support. Ideally the GDL should be completely water repellent and of metallic conductivity.

The active layer (AL) contains the catalyst which is usually supported on carbon black and bonded together with PTFE. The carbon black is chosen to have a high surface area to maximise the power density. The level of PTFE in the AL is less than in the GDL, typically the AL will contain between 2 and 25% PTFE, depending on the level of hydrophobicity required. The basic function of the PTFE in the active layer is to bind the carbon black together, but still provide multiple three-phase contact points where gas, electrolyte and carbon supported catalyst meet [38]. Different structures depending on the nature of the carbon support, carbon/PTFE ratio and electrode fabrication process can be obtained where electronic conductivity, ionic transport and gas transport have to be provided [39].

2.4.2. Materials used in electrode fabrication

AFC electrodes can be made of different materials with different structures, but modern electrodes tend to use high surface area carbon supported catalysts and PTFE to obtain the necessary TPB. Electrode performance in AFCs depends on catalyst surface area rather than catalyst weight. As with all other fuel cells, the catalyst loading is a critical parameter in determining performance. The nature of the catalyst support is also of prime importance to achieve high catalytic activity.

PTFE is a hydrophobic polymer material which has become the binding agent of choice since its commercial introduction in the 1950s by Dupont; although other materials are sometimes used (paraffin, polyethylene, polypropylene, wax *etc*.). It is available either as dry powder additives, or as a ready made aqueous suspension (containing proprietary dispersants). Both of these forms have been used to make electrodes [39]. PTFE can be present in the form of spherical particles, fibrils or thin films on porous substrates [40]. The PTFE penetrates deep into the sub-surface of the carbon when the dispersion is mixed with the carbon black powder. However, generally it is necessary to melt the PTFE in order to provide a thin film over the entire surface of the carbon black. This process is usually called sintering and takes place at temperatures around 320 °C [41, 42].

The electrical, chemical and structural properties of carbon make it an ideal material for use in AFC electrodes [43]. Carbon blacks, which are the most commonly used

carbon support in AFC electrode fabrication, consist of carbon in the form of near spherical particles obtained by the thermal decomposition of hydrocarbons. High surface area is achieved in a separate step, by treatment with steam at a temperature in the range of 800-1000 ºC. The inner core of the carbon particle is less ordered than the outside, and as a consequence the action of the steam causes large numbers of pores to form which interconnect to create the characteristic high surface area. The particle, however, does not completely disintegrate, but remains agglomerated to its neighbours. Specific surface areas of over 1000 m^2 g^{-1} can be obtained [44]. Porosity and surface area are the main characteristics of the carbon black structure. Studies have been carried out in order to gain better control of the carbon structure during the fabrication process [45]. Oxygen and hydrogen groups are introduced onto the carbon surface during the manufacturing process. The carbon-oxygen group is by far the most important and influences the physico-chemical properties of carbon blacks. Chemisorption of oxygen, and a build-up of carbon-oxygen surface compounds, occurs at temperatures below 400 ºC, whereas decomposition of these compounds occurs above 400 ºC. Formation of these groups by oxidative treatment in gaseous and liquid phases has been comprehensively studied [44, 46].

Despite the preference to use carbon black in gas diffusion electrode (GDE) fabrication, alternative catalyst supports have been tried. Hacker reported similar performance between silver and platinum catalysts supported on carbon nanofibres showing the capability of the fibres to provide the required porosity and pore structure to obtain good performance [47]. Huang showed higher performance using a binary catalyst support composed of carbon nanotubes (CNT) and active carbon black compared with a single-support catalyst. The best performance was obtained when the mass ratio was 50:50 [48]. Yang also showed good electrochemical performance with the same kind of binary support using MnO_2 as catalyst. A higher accessible surface area, an improved conductivity, and faster ORR kinetics explain the improvement [49]. Carbon nanotube / perovskite composite materials have also been tested by Weidenkaff with promising results [50].

2.4.3. Operational Mechanism

The electrochemical behaviour of the GDE can be controlled by varying the structure of its component layers and in particular by varying the ratio of hydrophobic and hydrophilic pores within the carbon support. Two structures have been developed, each playing a different role within the electrode. The primary 'macro' structure is formed at distances greater than 1µm, and is created by the partial enclosure of the carbon particles by the PTFE. It forms the skeleton structure which ensures electronic conductivity throughout the electrode and also provides mechanical support. Different macrostructures can be obtained by varying the carbon particle size and shape, the carbon / PTFE ratio, and the electrode fabrication process. The secondary 'micro' structure, created by the pore system inside of the carbon particles, depends on the surface area and pore structure of the carbon used. This structure is directly linked to the carbon manufacturing and activation process which greatly influences the micro-porosity of the carbon particles [39]. Indeed, the carbon particles have been shown to consist of macropores which are hydrophobic, and micropores (<0.01 µm) which are hydrophilic. The hydrophilic and hydrophobic property of the carbon depends on the nature of the surface groups which can be selected by various thermal and chemical treatments. The hydrophobic macropores have been shown to play an essential role in gas mass-transport by acting as gas supplying channels. The ORR mechanism occurs in the hydrophilic micropores which are filled with electrolyte and on the boundary of micro and macropores [51, 52].

The TPB is formed in the outer regions of the carbon particle shell where it is covered by a film of liquid electrolyte at the interface between the carbon micro and macro structures. The carbon particles arrangement is described as a 'tight bed of packed spheres' where the large vacancies between the particles are filled with electrolyte ensuring the ionic transport and where the carbon pore system and hydrophobic channels created by the PTFE ensure the gas transport as shown in Fig. 2.6 [39].

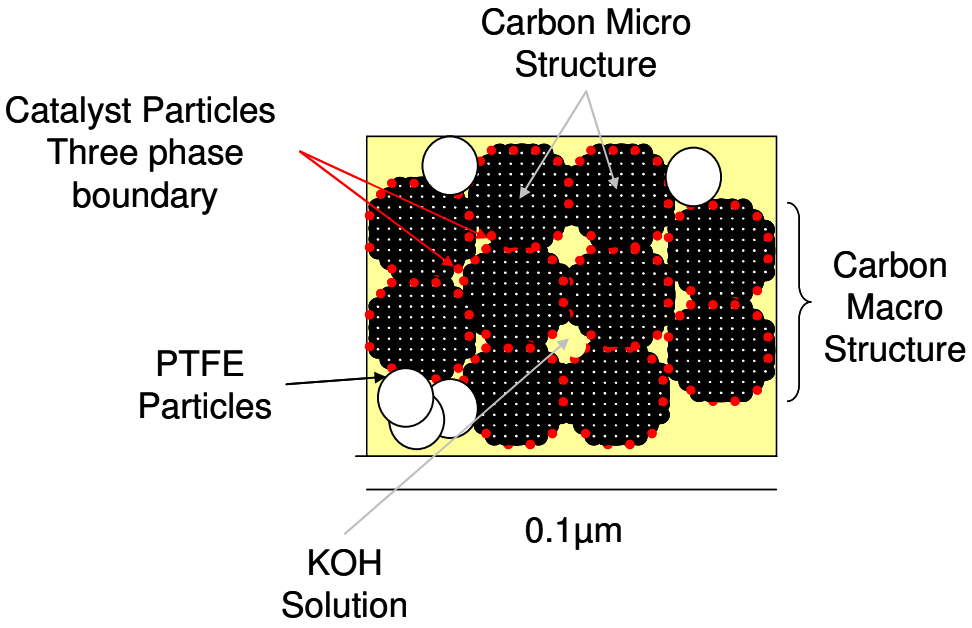


Figure 2.6: Schematic illustration of the carbon macro and micro structure within the active layer [39].

The thicknesses of the different layers have to be controlled to optimise electrode performance. The GDL thickness has to be as thin as possible to maximise oxygen accessibility, while the AL has to be optimized to maximize the reaction area constituted by the TPB. Kiros obtained maximum limiting current densities with two different catalysts, the AL thickness lying between 0.5 and 0.6 mm [53].

2.4.4. Electrode Modelling

Many publications have discussed the behaviour of porous electrodes in alkaline fuel cells. Whereas some authors have focused on specific issues such as current distribution [54], or the degree of catalyst utilization [55, 56], the majority have tried to understand the overall mechanism of operation in the GDE related to the structure; considering factors such as gas diffusion and electrolyte penetration. Several models have been used such as the simple pore model [57], the thin film model [58] or the dual scale of porosity model [59]. In the former, a range of porosities is considered, where macropores are gas filled and micropores are electrolyte filled [60, 61]. Giner [62] listed the limitations of this 'flooded porous electrode' model introducing the concept of 'flooded agglomerates'. The operational mechanism of this structure,

shown in Fig. 2.7, consists of catalyst particles which form porous agglomerates 'flooded' with electrolyte under working condition. The agglomerates are kept together by the PTFE which creates hydrophobic gas channels. Reactant gases diffuse through the channels and dissolve in the electrolyte contained in agglomerates to react on available catalyst sites. It has been reported elsewhere that the concept of 'flooded agglomerates' gives a satisfactory explanation for the behaviour of PTFE-bonded gas diffusion electrodes, and is in good accordance with experimental findings [40, 63-65].

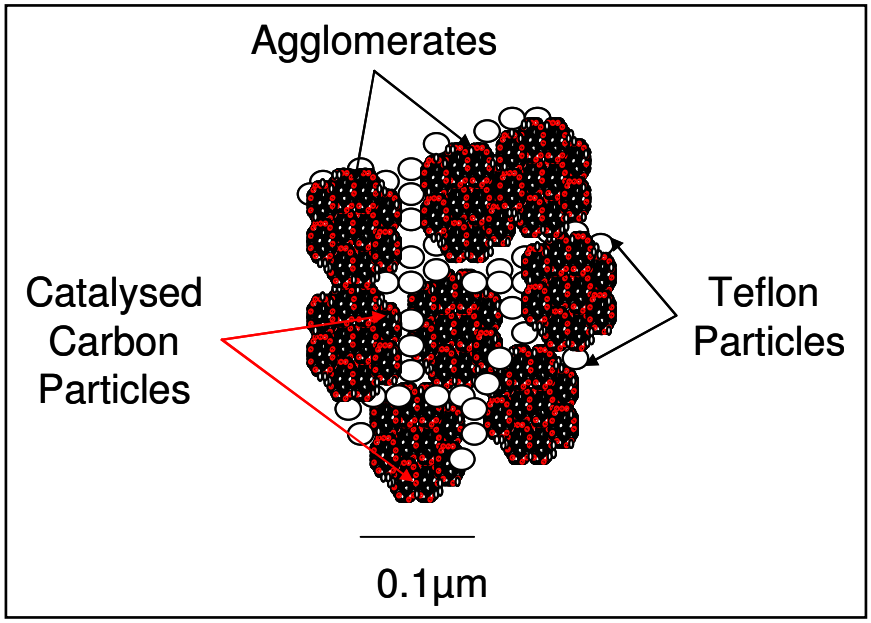


Figure 2.7: Schematic illustration of the 'flooded agglomerate' model [62].

Further single cell (anode/electrolyte/cathode) models have shown that cathode reaction kinetics are particularly important in determining the overall cell performance, predicting that the diffusion of dissolved oxygen contributes most to the polarization losses at low potentials (high current region), while the electronic resistance contributes most at high cell potentials (low current region). As a consequence, cell performance can be increased by means of improved cathode fabrication methods, in which both gas-liquid and liquid-solid interfacial surface areas are increased and the diffusion path of dissolved oxygen to catalytic sites is reduced [30, 56, 66-68].

2.4.5. Electrode Fabrication

Since different electrode structures lead to different cathode performance, the electrode fabrication requires special attention where the gas permeability of the GDL and the wettability of the AL are the two main performance-limiting factors [69]. Structural parameters of the different layers can to be optimized by varying the carbon support used, the carbon/PTFE ratio and the fabrication conditions to obtain the best cathode performance [12, 39, 70-72]. The electrochemical performance of the electrodes is also controlled by the initial porous structure and chemical surface properties of the active carbon, which in turn depend on the process fabrication route. An activation step appears to improve the electrochemical activity and stability of the carbon black by means of thermal, physical and chemical treatments [73, 74]. Increased surface area, formation of a defined inter-pore structure and an increased surface activity by the formation of catalytically active groups on the surface occurs during such treatment. The activity of carbon black is proportional to its surface area, the higher the better [75]. High temperature treatment leads to a higher surface area and as a consequence to a higher electrochemical activity. Carbon pre-treatment needs to be specific to the type of carbon black. For example, the surface area has been found to increase significantly for Vulcan XC-72 in the presence of CO_2, whereas a N_2 atmosphere is required for Ketjenblack when heat-treated at 900^{o}C [76].

Pressing, rolling, screen-printing and spraying methods are used in the production of AFC electrodes [72, 77]. The rolling method is the most commonly applied. The process shown in Fig. 2.8 is generic and variations include addition of filler materials such as sugar or ammonium bicarbonate, along with various washing or drying steps. If PTFE powder is used and ground with the carbon, the method is referred to as the ‘dry-method’. If PTFE suspension and water are mixed with the carbon black it is referred to as the ‘wet-method’ [71].

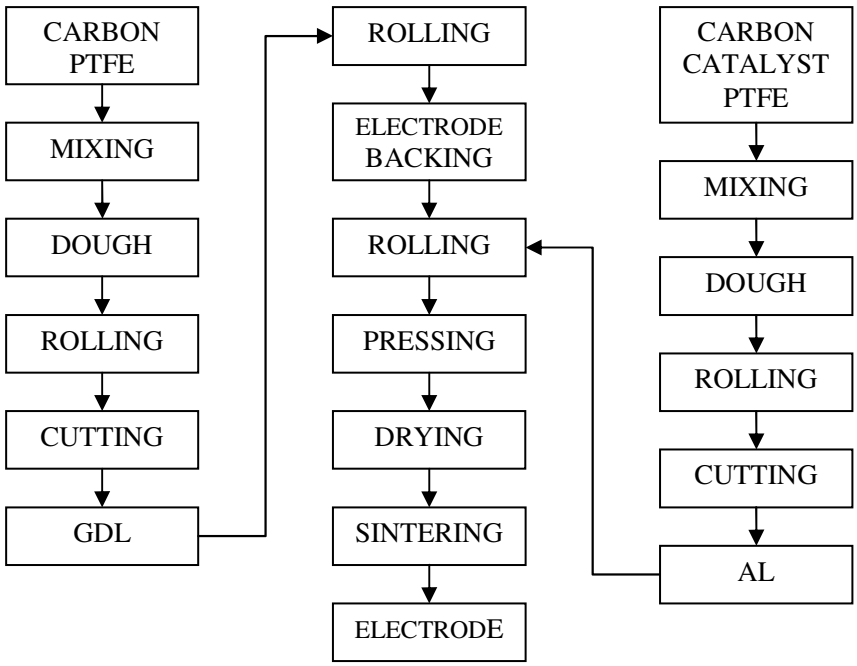


Figure 2.8: Electrode fabrication: The rolling method.

The method of mixing the carbon black with the PTFE will have a direct effect on the electrode activity and stability. Musilova showed that using an aqueous PTFE deposition process onto the carbon surface leads to a hydrophobic blend. However, if ethanol is used instead, the electrode is more hydrophilic [78]. Motoo and Watanabe showed that very fine networks of gas channels are needed in the AL to obtain high performance. Since diffusion of dissolved reactant gas is a limiting factor for high current generation, good dispersion of the carbon and PTFE particles is required to increase the number of gas dissolving sites and reduce the diffusion path length of dissolved gas to the catalyst sites, resulting in a performance increase. To achieve this, new techniques of fabrication have been applied involving, for example, colloid mill and ultrasonic agitation [79-81].

2.4.6. The oxygen reduction reaction (ORR) in alkaline media

Optimising the cathode performance is essential because it governs the overall performance of the fuel cell. According to Bockris at high current density, 80% of the polarization may be due to the oxygen reduction [2]. The ORR is a complex process

involving four coupled proton and electron transfer steps. Several of the elementary steps involve reaction intermediates leading to a wide choice of reaction pathways. The exact sequence of the reactions is still not known, and identification of all reaction steps and intermediates, and their kinetic parameters is required, which is clearly challenging. Appleby has reviewed and discussed the issues relating to the ORR in acid and alkaline solution [82]. In acid electrolyte, the ORR reaction is electrocatalytic, as pH values become alkaline, redox processes involving superoxide and peroxide ions start to play a role and dominate in strongly alkali media. The reaction in alkaline electrolytes may stop with the formation of the relatively stable HO_2^- solvated ion, which is easily disproportionated or oxidized to dioxygen. Although there is no consensus on the exact reaction sequence, two overall pathways take place in alkaline media [83]:

(i) Direct 4-electron pathway:

$$O_2 + 2H_2O + 4e^- \rightarrow \quad 4OH^- \tag{2.3}$$

(ii) Peroxide pathway or '2+2-electron' pathway:

$$O_2 + H_2O + 2e^- \quad \rightarrow \quad HO_2^- + OH^- \tag{2.4}$$

$$\text{With } HO_2^- + H_2O + 2e^- \quad \rightarrow \quad 3OH^- \tag{2.5}$$

The peroxide produced may also undergo catalytic decomposition with the formation of dioxygen and OH^-, given by:

$$2HO_2^- \rightarrow \quad 2OH^- + O_2 \tag{2.6}$$

The kinetics of the ORR reaction is more facile in alkaline medium than in some acid medium such as H_2SO_4 (Markonic 1997). This is also illustrated by the comparison made by Blurton [84] for the operating potentials of a fuel cell running on H_2/O_2 at a controlled current density of 100 mA cm^{-2} at 70 ºC with platinum electrodes. These workers reported a potential of 0.67 V for 13.9 M H_3PO_4 and a potential of 0.89 V for 6.9 M KOH versus a hydrogen reference electrode. The higher voltage (performance) of the alkaline system was explained by the preferred formation of peroxide species in the alkaline medium which desorbs more readily than in the acid counterpart.

Blizanac [85] used a thermodynamic analysis to explain the origin of the pH effect, showing that the overpotential required to facilitate the 4-electron transfer process at high pH is relatively small compare to the potential required at low pH in the case of Ag (111). At high pH, no specific chemical interaction between the catalyst and O_2 or O_2^- is required, whereas strong chemical interaction is necessary at low pH. Blizanac also explained how the low activity of catalysts in acid media is exacerbated by the presence of spectator species adsorbed onto the electrode surface, which act to physically block the active sites and also lower the adsorption energy for intermediates, so retarding the reaction rate.

2.4.7. Cathode catalyst materials

Due to the inherently faster kinetics for the ORR in alkaline media, a wide range of catalysts have been studied including noble metals, non-noble metals, perovskites, spinels, *etc* [37,48,71,140,144]. However, it is important to appreciate that the carbon support plays a role in the kinetics as well as the catalyst supported on its surface, so that in evaluating the performance, it is necessary to assess the loading of the catalyst and the type of carbon used where its hydrophobic properties as well as its surface groupings greatly affect the final hydrophobic structure and the TPB length of the electrode. The performance of the catalyst/support system is considered since carbon participates in the reaction by a 2-electron process. The catalytic activity of the system is directly linked to the physical and chemical characteristics of the carbon support. The catalyst deposition method is critical since a high catalytic activity relies on a very fine and well dispersed catalyst particle. In the case of platinum, the particle size is generally in the nanometre range. The carbon impregnation of metal salt solution with further reduction of the metal is commonly used, and well known for it simplicity and ability to produce metal nanoparticles with nearly mono-dispersed size distribution and easy scale-up [151-154].

2.4.7.1. Noble metal catalyst

Platinum is the most commonly used and active catalyst for the electro-reduction of oxygen and all of the platinum-group metals reduce oxygen in alkaline media according to the direct four electron process [86-94]. At a very low Pt/C ratio, the overall number of electrons exchanged is approximately two due to the carbon contribution, but increases as the Pt/C ratio increases, reaching four electrons at 60% wt.Pt [95]. Pt-based alloys have been studied and generally exhibit higher activity [96] and stability [97] than Pt-alone. The enhanced electrocatalytic activity of Pt-alloy systems has been explained by a number of phenomena, including: (i) reduction in Pt-Pt bond distance, favouring the adsorption of oxygen; (ii) the electron density in the Pt 5d orbital and (iii) the presence of surface oxide layers [95, 98-101]. Due to the high cost of Pt, techniques have been developed to reduce loading [56, 95, 101-103]. For example, monolayer deposition of Pt on non-noble metal nanoparticles showed improved catalytic properties with a very small amounts of Pt [103, 104]. The carbon impregnation with hexachloroplatinic acid solution ($H_2PtCl_6.6H_2O$) followed by metal reduction using heat treatment or wet chemical methods, have been widely used to produce a catalyst particle size lying between 12 to 34 nm [48, 78, 95, 105, 106]. A more complex colloidal precursor deposition technique showed a PtRu particle diameter close to 2 nm [107, 108].

Silver has been studied as a potential replacement of Pt due to its high activity for the ORR and its lower cost. Silver in alkaline solutions is oxidized in two steps; first a layer of Ag_2O is formed which is partly oxidized in the second to AgO [109]. ORR occurs with the participation of 2 and 4 electron processes, depending on the surface state and in particular on its oxidation state and electrode potential [47, 110-118]. The size of the Ag particles affects the different catalytic activity for these two processes. Four electrons are exchanged during ORR on nano-dispersed silver particles on carbon, with an optimum loading lying between 20 wt% [111] and 30 wt% [113]. The effect of electrolyte concentration is positive for silver catalyst but not for Pt catalyst, which is slightly hindered due to greater adsorbed species coverage. Silver becomes competitive to Pt due to favoured kinetics in high concentration alkaline media [47, 110], but shows a strong propensity to dissolution at open circuit voltages following Eq. (2.7) [28]:

$$4\ Ag + O_2 + H_2O \rightarrow 4\ Ag^+ + 4OH^- \quad (2.7)$$

At an overpotential of 100-300 mV, this dissolution was found not to be significant [113]. The impregnation of $AgNO_3$ is commonly used, associated with different techniques of Ag reduction [47, 119]. Chatenet using impregnation of $AgNO_3$ and electrochemical reduction in sulphuric acid to obtain silver particle sizes in the range 5-10 nm (Fig. 2.9) [110].

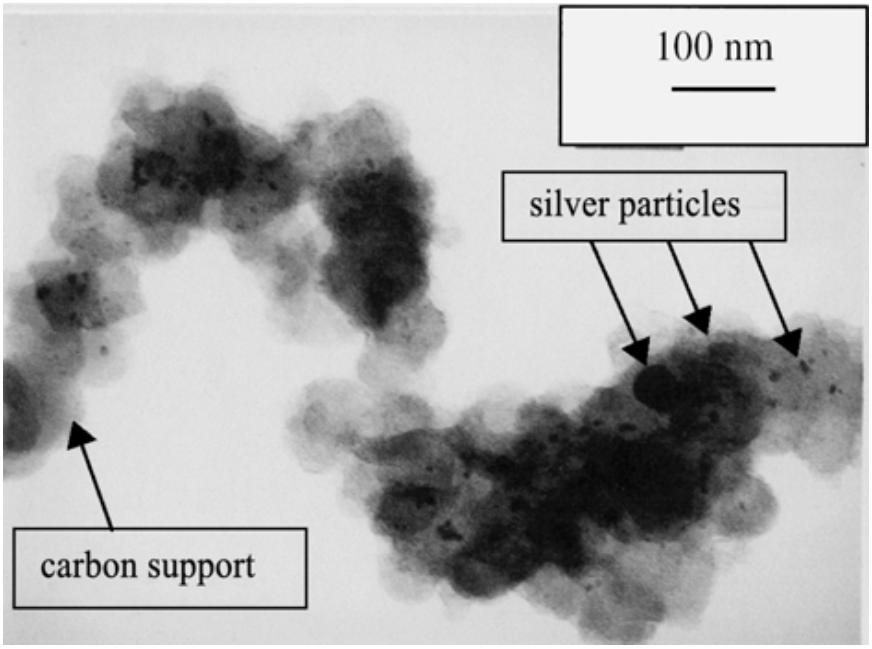


Figure 2.9: TEM photograph for reduced carbon-supported silver nanoparticles [110].

2.4.7.2. Non-noble metal catalyst

Whereas carbon supports show poor electrochemical activity in acidic media [120], carbon blacks and graphite have been shown to catalyse the ORR in alkaline media with the formation of HO_2^- in a two electron process (Eq 2.4), where high surface area carbon blacks such as Vulcan XC-72R (25 nm, 250 m^2g^{-1}) showed an increased activity [74, 75, 120-122].

Recently, manganese oxides have attracted more attention as potential catalysts for both fuel cells [123, 124] and metal-air batteries [125] because of their attractive cost

and good catalytic activity toward O_2 reduction. The investigation of different manganese oxides dispersed on high surface area carbon black showed low activity for MnO/C and high activity for MnO_2/C and Mn_3O_4/C. The higher activity of MnO_2 was explained by the occurrence of a mediation process involving the reduction of Mn(IV) to Mn(III), followed by the electron transfer from Mn(III) to oxygen. The reaction was sensitive to the manganese oxide /carbon ratio in which, at lower ratios, the reaction proceeds by the 2-electron pathway, evolving to an indirect 4-electron pathway with disproportionation of HO_2^- into O_2 and OH^- at higher catalyst/carbon ratios [125-128]. The catalytic activity for the disproportionation reaction has led to a new approach of dual system catalysis in which one catalyst is used for the reduction of O_2 through the two-electron process producing HO_2^-, which is subsequently decomposed by MnO_2, leading to a four-electron process [129-131]. The MnO_2 catalytic activity was found to vary following its crystalline structure in the sequence: β-MnO_2 < λ-MnO_2 < γ-MnO_2 < α-MnO_2 ≈ δ-MnO_2, in which higher activity seems to go with higher discharge ability, proceeding through chemical oxidation of the surface Mn^{3+} ions generated by the discharge of MnO_2 rather than through a direct 2-electron reduction [132]. γ-MnOOH exhibits higher activity than γ-MnO_2; this has been explained by the fact that amorphous manganese oxide has more structural distortion and is more likely to have active sites compared to crystalline manganese oxides [125, 133].

Pyrolysed macrocyles on carbon supports have been studied in alkaline media showing high activity towards the ORR. Cobalt phthalocyanine has been shown to reduce oxygen with similar kinetics to that of Pt [134]. Electrodes made of cobalt/iron tetraphenylporphyrin (CoTPP, FeTPP) demonstrated good performance, outperforming electrodes made of silver catalysts. Structural changes and increased surface area is required to enhance the catalytic activity, which is obtained by chemical and heat treatment of the carbon and the porphyrins [37, 71, 135]. This high catalytic activity was attributed to the combined effect of the macrocycle black and Co; however, poor stability has been shown where the loss of Co appeared to be important, leading to performance deterioration [136]. $CoCO_3$+TetraMethoxyPhenylPorphyrin (TMPP) +carbon showed better performance than CoTMPP+carbon confirming the fact that the structure of the metal macrocycle is not responsible for catalytic activity, but its origin is due to the simultaneous

presence of the metal precursor, active carbon and a source of nitrogen, supposed already to be part of the catalytic process [137, 138].

Perovskite-type oxides, which have an ABO_3-type crystal structure, have shown a high cathode activity in alkaline media proceeding by a 2-electron pathway where HO_2^- is further reduced [139]. Good performance has been reported with different catalyst composition such as $La_{0.5}Sr_{0.5}CoO_3$, $La_{0.99}Sr_{0.01}NiO_3$ [140], $La_{1-X}A_xCoO_3$ (A = Ca, Sr) [141], $Ca_{0.9}La_{0.1}MnO_3$ [142] and $Pr_{0.6}Ca_{0.4}MnO_3$, $La_{0.6}Ca_{0.4}CoO_3$ [143]. The catalyst support choice seemed to be crucial to obtain stable performance. Graphite supports appeared less stable [144] than high surface area carbon black [139].

A spinel is a ternary oxide with an AB_2O_4 structure in which the choice of the B cation is critical since it plays an important part in the activity of the catalyst [145, 146]. Studies of $MnCo_2O_4$ catalysts have mainly indicated an ORR mechanism that involves a 2-electron process with HO_2^- formation [147, 148]. The catalytic activity depends greatly on the preparation route; the decomposition of Co and Mn nitrates and subsequent heat treatment is most commonly used [149-151].

2.4.8. Performance

A summary of the data in the literature describing cathode performance for different catalysts is given in Table 1 and 2, which have been separated according to whether the measurements were made in oxygen or air. All the potentials are overpotentials reported against an Hg / HgO reference electrode, the KOH concentration lying between 5 and 8 M. The electrolyte temperature varied between 25 and 70^{o}C and is reported for each instance.

Table 2.1: Cathode performance using different catalysts with O_2.

Catalyst	KOH Temperature (^{o}C)	KOH Concentration (M)	Potential (V)	Current Density (mA cm^{-2})	Source
Pt/Pd/C 4wt.%Pt/6wt.%Pd	25	6	-0.1 -0.2 -0.3	900 1600 2100	[152]
Ag 47 mg cm^{-2}	70	7	-0.1 -0.2	250 540	[117]
$La_{0.5}Sr_{0.5}CoO_3$/C 7%wt	25	6	-0.1 -0.2 -0.3	250 700 1600	[140]
CoTPP/C 1.76 mg cm^{-2}	40	5	-0.06 -0.14 -0.18	150 600 950	[37]
$La_{0.6}Ca_{0.4}CoO_3$/C 9-13 mg cm^{-2}	25	6	-0.1 -0.2 -0.3	150 500 1000	[144]

Table 2.2: Cathode performance using different catalysts with air.

Catalyst	KOH Temperature (^oC)	KOH Concentration (M)	Potential (V)	Current density (mA cm^{-2})	Source
Pt/CNT/C 100 μg cm^{-2}	25	6	-0.2 -0.5	125 520	[48]
$Pr_{0.8}Ca_{0.2}MnO_3$/C 50 wt.%	60	8	-0.1 -0.15	115 260	[143]
CoTMPP/C Not known	25	5	-0.1 -0.2 -0.25	140 350 500	[71]
MnO_2/ CNT/C 3.63 mg cm^{-2}	25	8	-0.2 -0.5	91 440	[153]
$LaMnO_3$/C 6.9 mg cm^{-2}	60	8	-0.08 -0.1	300 400	[154]
$MnCo_2O_4$/C 14 mg cm^{-2}	60	6	-0.1 -0.2	150 300	[151]

2.4.9. Electrode Durability

Several degradation rates have been reported; Tomantschger reported performance degradation under working conditions of 10-30 mV/1000 h over a period of 3500 h at 0.1 A cm^{-2} [140]. Gouerec showed a degradation rate of 5-10 mV/1000 h over a period of 2800 h at 0.1 A cm^{-2} [19]; Gulzow reported, over 3500 h at 0.15 A cm^{-2}, a degradation rate of 17 mV/1000 h with silver based electrodes [138]. Several causes or effects have been proposed to explain the degradation of AFC cathode performance with time; they are described in the following sections. The understanding of these effects and their studies is very important in the development of increased AFC lifetimes. However, few studies have been reported in the literature to date.

2.4.9.1. CO_2 effect

Carbon dioxide is generally believed to be detrimental to the performance of the alkaline electrolyte due to the formation of carbonate species which will eventually cause a decrease in ionic conductivity. Thus, air is generally scrubbed to reduce the CO_2 content to between 5 and 30 ppm, depending on the technology used, before it enters the fuel cell [19]. However, residual CO_2 reacts to form carbonate ions following Eq. (2.1), which increases the ionic resistance of the KOH because the conductivity of CO_3^{2-} is lower than that of OH^-. If carbonate formation occurs, it forms in the pores of the electrode active layer. Subsequent mass transport will take place causing the carbonate species to be transferred to the bulk liquid electrolyte. If the wash out process, which depends on the porosity of the AL and the electrolyte viscosity, is fast enough, no CO_2 effect is observed; otherwise potassium carbonate is precipitated in the pores (Eq. 2.2) blocking them, or causing destruction of the structure due to the expansion of the precipitate [155].

Authors are not unanimous on the effect of CO_2 on cathode degradation. Whereas Rolla [155] attributes CO_2 to be the main factor determining cathode ageing, Gulzow [156] has demonstrated 3500 hours of operation with a cathode in the presence of CO_2 concentrations 150 times that in air, asserting that CO_2 in air had no influence on the cathode, but rather degradation in the fuel cell performance was attributed solely to its impact on electrolyte conductivity, which could be mitigated by exchanging the electrolyte every few hundreds hours (McLean estimates the KOH cost at 0.25 dollar

cents/kWh if the electrolyte is changed every 500 h for a stack lifetime of 5000 h). Based on published evidence, the CO_2 effect seems to be electrode structure dependant, wherein the pore structure of the electrode is crucial. Sato observed a different CO_2 effect on the cathode stability depending on the carbon support used. It was found that CO_2 had a strong effect on cathode stability when electrodes were prepared from activated carbon. No CO_2 dissolution or progressive wetting was observed with Asahi-90 black which was explained by the small particle size of this carbon and its compact electrode structure [157].

2.4.9.2. Corrosion effect

The degradation reported by Tomantschger [158] of the electrochemical performance of the electrode with increasing operating time was assigned to the corrosion of carbon, and PTFE degradation caused by the KOH electrolyte. The carbon is slowly oxidized due to attack by the HO_2^- radical formed as an intermediate during oxygen reduction. Korovin [159] identified the discreet processes of electrocatalyst deterioration as composed of corrosion, chemical dissolution, cathode hydrogenization and metal intercalation. An increase in current density, temperature and ligand (OH^-) concentration was found to accelerate corrosion. A multi-catalyst system has been proposed to increase lifetime using the most stable support in moderate electrolyte concentration. PTFE was shown to lose some hydrophobicity after KOH exposure, which was attributed to surface chemical changes. It was shown that the contact angle reached a minimum; the higher the KOH temperature and concentration, the shorter the time taken to reach this minimum [160].

2.4.9.3. Weeping and flooding effects

The reduction of the cathode performance over time is often caused by flooding of the electrode structure by the electrolyte, which reduces oxygen accessibility to reacting sites by blocking gas pores. Gouerec [36] described this phenomenon as the main parameter driving cathode degradation, showing an increasing cell capacitance over time due to greater electrode surface being in contact with the electrolyte. Burchart [161] considered the role of electrocapillarity in which the contact angle between the electrode surface and the electrolyte is potential dependant. The contact angle was

found to decrease with a decrease in potential from the OCV (open circuit voltage) which increased wetting of the electrode. An increase in pH and temperature, especially at 90^{o}C with the condensation of the vapour in gas pores, both lead to flooding of the electrode. Wagner [117] tested silver catalysed GDEs for 5000h showing a voltage loss of 100 mV, which was partially explained by a decrease of the catalyst surface roughness, but mainly by PTFE degradation. The decrease in hydrophobicity with time allows more pore flooding, which hinders gas transport. The hypothesis that the degradation of cathode performance is mainly caused by excessive electrode wettability was confirmed by Maja [12] who showed that the use of acetylene black ensures a highly hydrophobic and homogeneous electrode structure with long term durability, whereas oil-furnace carbon such as Vulcan XC-72R displayed excessive wettability. Hull [162] and Baugh [163] studied the creep of alkaline electrolyte through cathodes. The production of OH^- ions arising from the ORR in the active zone increases its concentration. The movement of water from the bulk electrolyte, or from condensation via the vapour phase to compensate this gradient, causes an increase in the size of the active zone with the result that the reaction zone moves through the electrode. Khalidi [164] characterized the weeping process on the cathode and showed that humidification of the oxygen inlet reduces this effect.

2.5. Conclusions

AFCs offer a fuel cell solution with the potential for low cost. The alkaline electrolyte means that platinum based catalysts are not required, and AFC production methods are scaleable. AFC systems, which have been successfully used in space applications, need to meet the challenging requirement of low cost, high performance and durability to be successful in terrestrial applications. The development of circulating electrolyte systems has shown to have advantages compared to the immobilized electrolyte systems for terrestrial applications that could open the way to the commercialization of this technology. Electrolyte leakage and parasitic power losses are still challenges with the circulating electrolyte system and require the development of improved stack designs.

After a long hiatus in research and development, the alkaline fuel cell is creating renewed interest among research groups and some fuel cell companies, but research and development remains limited. There is no doubt that the success of this technology will come mainly by the improvement of electrodes, especially the cathode which is responsible for most of the cell losses.

Macro and micro structures in the different layers have to be obtained during the electrode fabrication to ally performance and durability where the carbon support is of prime importance in obtaining optimized performance. The development of new catalyst systems is more likely in alkaline media because of the wide range of options for the materials support and catalyst, as compared to acidic media which offers more limited materials choice. Alternatives to platinum have been investigated, showing good performance, comparable sometimes to platinum itself, but more work is needed to meet the durability targets required for commercial application.

The aim of this thesis is the development of a gas diffusion cathode using innovative substrate materials (nickel foam and porous silver membranes) which ally mechanical support, current collection and catalyst support so as to reduce the cost of the electrode keeping acceptable performance.

2.6. References

[1] M.L. Perry. J. Electrochem. Soc. 149 (2002) S59.

[2] J.O.M. Bockris, A.J. Appleby. Energy 11 (1986) 95.

[3] G. Mulder, P. Coenen, A. Martens, J. Spaepen. Int. J. Hydrogen Energy 33 (2008) 3220-3224.

[4] M. Cifrain, K.V. Kordesch, in: W. Vielstich, A. Lamm, H. Gasteiger (Eds.), Handbook of Fuel Cells, John Wiley, 2003, p. 267,Vol1.

[5] M. Duerr, S. Gair, A. Cruden, J. McDonald. J. Power Sources 171 (2007) 1023-1032.

[6] E. Gulzow, M. Schulze, U. Gerke. J. Power Sources 156 (2006) 1-7.

[7] T. Hejze, J.O. Besenhard, K. Kordesch, M. Cifrain, R.R. Aronsson. J. Power Sources 176 (2008) 490-493.

[8] B.Y.S. Lin, D.W. Kirk, S.J. Thorpe. J. Power Sources 161 (2006) 474-483.

[9] A. Verma, S. Basu. J. Power Sources 168 (2007) 200-210.

[10] E. Gulzow. J. Power Sources 61 (1996) 99-104.

[11] G.F. McLean, T. Niet, S. Prince-Richard, N. Djilali. Int. J. Hydrogen Energy 27 (2002) 507-526.

[12] M. Maja, C. Orecchia, M. Strano, P. Tosco, M. Vanni. Electrochim. Acta 46 (2000) 423-432.

[13] A.E.S. Sleightholme, J.R. Varcoe, A.R. Kucernak. Electrochem. Commun. 10 (2008) 151-155.

[14] D. Stoica, L. Ogier, L. Akrour, F. Alloin, J.F. Fauvarque. Electrochim. Acta 53 (2007) 1596-1603.

[15] J.R. Varcoe, R.C.T. Slade, E.L.H. Yee, S.D. Poynton, D.J. Driscoll. J. Power Sources 173 (2007) 194-199.

[16] Y. Wang, L. Li, L. Hu, L. Zhuang, J. Lu, B. Xu. Electrochem. Commun. 5 (2003) 662-666.

[17] J.R. Varcoe, R.C.T. Slade, in: Wiley-VCH (Ed.). Fuel Cells, 2005, pp. 187-200.

[18] Y. Kiros, C. Myrén, S. Schwartz, A. Sampathrajan, M. Ramanathan. Inter. J. Hydrogen Energy 24 (1999) 549-564.

[19] Y. Kiros, S. Schwartz. J. Power Sources 87 (2000) 101-105.

[20] M.A. Al-Saleh. J. Appl. Electrochem. 24 (1994) 575.

[21] M. Schulze, E. Gülzow, G. Steinhilber. Appl. Surface Sci. 179 (2001) 251-256.

[22] S. Gultekin, M.A. Al-Saleh, A.S. Al-Zakri, K.A.A. Abbas. Inter. J. Hydrogen Energy 21 (1996) 485-489.

[23] T. Kenjo. Bulletin of the Chemical Society of Japan 54 (1981) 2553.

[24] K. Schultze, H. Bartelt. Inter. J. Hydrogen Energy 17 (1992) 711-718.

[25] M.A. Al-Saleh, S. Gultekin, A.S. Al-Zakri, A.A.A. Khan. Inter. J. Hydrogen Energy 21 (1996) 657-661.

[26] M.A. Al-Saleh, R. Sleem Ur, S.M.M.J. Kareemuddin, A.S. Al-Zakri. J. Power Sources 72 (1998) 159-164.

[27] J. Larminie, A. Dicks, in: J. Wiley (Ed.). Fuel Cell Systems Explained, 2002, pp. 109-122.

[28] M. Cifrain, K.V. Kordesch. J. Power Sources 127 (2004) 234-242.

[29] Fuel Cell Handbook, 7th ed., U.S.Dept.Energy, Morgantown, West Virginia, 2004.

[30] K. Kordesch, J. Gsellmann, M. Cifrain, S. Voss, V. Hacker, R.R. Aronson, C. Fabjan, T. Hejze, J. Daniel-Ivad. J. Power Sources 80 (1999) 190-197.

[31] T. Burchardt, P. Gouerec, E. Sanchez-Cortezon, Z. Karichev, J.H. Miners. Fuel 81 (2002) 2151-2155.

[32] E. De Geeter, M. Mangan, S. Spaepen, W. Stinissen, G. Vennekens. J. Power Sources 80 (1999) 207-212.

[33] K. Strasser. J. Power Sources 29 (1990) 149-166.

[34] K. Tomantschger, F. McClusky, L. Oporto, A. Reid, K. Kordesch. J. Power Sources 18 (1986) 317-335.

[35] E. Han, I. Eroglu, L. Turker. Inter. J. Hydrogen Energy 25 (2000) 157-165.

[36] P. Gouerec, L. Poletto, J. Denizot, E. Sanchez-Cortezon, J.H. Miners. J. Power Sources 129 (2004) 193-204.

[37] Y. Kiros, S. Schwartz. J. Power Sources 36 (1991) 547-555.

[38] N.N.P. Brandon, D.D.J. Brett. Philosophical transactions. Math., Phys., and Eng. Sci. 364 (2006) 147-159.
[39] K. Tomantschger, K.V. Kordesch. J. Power Sources 25 (1989) 195-214.

[40] W.M. Vogel, K.A. Klinedinst. Electrochim. Acta 22 (1977) 1385-1388.

[41] K.A. Klinedinst. J. Mater. Sci. 11 (1976) 794.

[42] K.A. Klinedinst. J. Mater. Sci. 11 (1976) 209.

[43] A.L. Dicks. J. Power Sources 156 (2006) 128-141.

[44] J. Donnet, R. Bansal, M. Wang. Carbon Black, Marcel Dekker, 1993.

[45] T. Kyotani. Carbon 38 (2000) 269-286.

[46] K. Kinoshita, J.A.S. Bett. Carbon 11 (1973) 403-411.

[47] V. Hacker, E. Wallnofer, W. Baumgartner, T. Schaffer, J.O. Besenhard, H. Schrottner, M. Schmied. Electrochem. Commun. 7 (2005) 377-382.

[48] H. Huang, W. Zhang, M. Li, Y. Gan, J. Chen, Y. Kuang. J. Colloid and Interface Sci. 284 (2005) 593-599.

[49] C.-C. Yang, S.-T. Hsu, W.-C. Chien, M. Chang Shih, S.-J. Chiu, K.-T. Lee, C. Li Wang. Inter. J. Hydrogen Energy 31 (2006) 2076-2087.

[50] A. Weidenkaff, S.G. Ebbinghaus, P. Mauron, A. Reller, Y. Zhang, A. Zuttel. Mater. Sci. Eng.: C 19 (2002) 119-123.

[51] G.V. Shteinberg, A.V. Dribinsky, I.A. Kukushkina, L.N. Mokorousov, V.S. Bagotzky. J. Electroanal. Chem. 180 (1984) 619-637.

[52] G.V. Shteinberg, A.V. Dribinsky, I.A. Kukushkina, M. Musilova, J. Mrha. J. Power Sources 8 (1982) 17-33.

[53] Y. Kiros, T. Quatrano, P. Bjornbom. Electrochem. Commun. 6 (2004) 526-530.
[54] K.J. Euler. J. Appl. Electrochem. 2 (1972) 105.

[55] K. Mund, F.v. Sturm. Electrochim. Acta 20 (1975) 463-467.

[56] N. Giordano, E. Passalacqua, V. Alderucci, P. Staiti, L. Pino, H. Mirzaian, E.J. Taylor, G. Wilemski. Electrochim. Acta 36 (1991) 1049-1055.

[57] L.G. Austin. Indus. & Eng. Chem. fundamentals 4 (1965) 321.

[58] S. Srinivasan, H.D. Hurwitz. Electrochim. Acta 12 (1967) 495-512.

[59] V.S. Markin. Russian chemical bulletin 12 (1963) 1551.

[60] E.A. Grens. Electrochim. Acta 15 (1970) 1047-1057.

[61] E.A. Grens, C.W. Tobias. Electrochim. Acta 10 (1965) 761-772.

[62] J. Giner. J. Electrochem. Soc. 116 (1969) 1124.

[63] R.P. Iczkowski. J. Electrochem.Soc.127 (1980) 1433.

[64] W. Vogel, J. Lundquist, A. Bradford. Electrochim. Acta 17 (1972) 1735-1744.

[65] S.-C. Yang, P. Bjornbom. Electrochim. Acta 37 (1992) 1831-1843.

[66] J.H. Jo. J. Appl. Electrochem. 30 (2000) 1023.

[67] M.C. Kimble. J. Electrochem. Soc. 138 (1991) 3370.

[68] M.C. Kimble. J. Electrochem. Soc. 139 (1992) 478.

[69] T. Kenjo, K. Kawatsu. Electrochim. Acta 30 (1985) 229-233.

[70] M.T. Ergul, L. Turker, I. Eroglu. Inter. J. Hydrogen Energy 22 (1997) 1039-1045.

[71] J. Kivisaari, J. Lamminen, M.J. Lampinen, M. Viitanen. J. Power Sources 32 (1990) 233-241.

[72] K. Kordesch, S. Jahangir, M. Schautz. Electrochim. Acta 29 (1984) 1589-1596.

[73] D.M. Drazic, R.R. Adzic. Electrochim. Acta 14 (1969) 405-411.

[74] R. Manoharan, A.K. Shukla. J. Power Sources 10 (1983) 333-341.

[75] A.J. Appleby, M. Savy. J. Electroanal. Chem. 92 (1978) 15-30.

[76] M. Pirjamali, Y. Kiros. J. Power Sources 109 (2002) 446-451.

[77] K. Kordesch, V. Hacker. J. Gsellmann, M. Cifrain, G. Faleschini, P. Enzinger, R. Fankhauser, M. Ortner, M. Muhr, R.R. Aronson, J. Power Sources 86 (2000) 162-165.

[78] M. Musilova, A. Kaisheva, J. Mrha, I. Iliev, S. Gamburzev. J. Power Sources 3 (1978) 245-255.

[79] S. Motoo, M. Watanabe, N. Furuya. J. Electroanal. Chem. 160 (1984) 351-357.

[80] M. Watanabe, K. Makita, H. Usami, S. Motoo. J. Electroanal. Chem. 197 (1986) 195-208.

[81] M. Watanabe, M. Tomikawa, S. Motoo. J. Electroanal. Chem. 182 (1985) 193-196.

[82] A.J. Appleby. J. Electroanal. Chem. 357 (1993) 117-179.

[83] E. Yeager. Electrochim. Acta 29 (1984) 1527-1537.

[84] K.F. Blurton, E. McMullin. Energy Conversion 9 (1969) 141-144.

[85] B.B. Blizanac, P.N. Ross, N.M. Markovic. Electrochim. Acta 52 (2007) 2264-2271.

[86] N.A. Anastasijevic, Z.M. Dimitrijevic, R.R. Adzic. J. Electroanal. Chem. 199 (1986) 351-364.

[87] G. Bianchi, F. Mazza, T. Mussini. Electrochim. Acta 7 (1962) 457-473.

[88] J.M. Martinovic, D.B. Sepa, M.V. Vojnovic, A. Damjanovic. Electrochim. Acta 33 (1988) 1267-1272.

[89] J.M. Martinovic, D.B. Sepa, M.V. Vojnovic, A. Damjanovic. Electrochim. Acta 34 (1989) 671-676.

[90] R. Pattabiraman. Applied Catalysis A: General 153 (1997) 9-20.

[91] D.B. Sepa, M.V. Vojnovic, M. Stojanovic, A. Damjanovic. J. Electroanal. Chem. 218 (1987) 265-272.

[92] D.B. Sepa, M.V. Vojnovic, L.M. Vracar, A. Damjanovic. Electrochim. Acta 32 (1987) 129-134.

[93] W.M. Vogel. Electrochim. Acta 13 (1968) 1821-1826.

[94] Y.-F. Yang, Y.-H. Zhou, C.-S. Cha. Electrochim. Acta 40 (1995) 2579-2586.

[95] F.H.B. Lima, E.A. Ticianelli. Electrochim. Acta 49 (2004) 4091-4099.

[96] K.V. Ramesh, A.K. Shukla. J. Power Sources 19 (1987) 279-285.

[97] M. Chatenet. J. Electrochem. Soc.150 (2003) D47.

[98] G. Couturier, D.W. Kirk, P.J. Hyde, S. Srinivasan. Electrochim. Acta 32 (1987) 995-1005.

[99] M.-k. Min, J. Cho, K. Cho, H. Kim. Electrochim. Acta 45 (2000) 4211-4217.

[100] T. Toda, H. Igarashi, M. Watanabe. J. Electroanal. Chem. 460 (1999) 258-262.

[101] M.B. Vukmirovic, J. Zhang, K. Sasaki, A.U. Nilekar, F. Uribe, M. Mavrikakis, R.R. Adzic. Electrochim. Acta 52 (2007) 2257-2263.

[102] N. Giordano, E. Passalacqua, V. Recupero, M. Vivaldi, E.J. Taylor, G. Wilemski. Electrochim. Acta 35 (1990) 1411-1421.

[103] K. Sasaki, Y. Mo, J.X. Wang, M. Balasubramanian, F. Uribe, J. McBreen, R.R. Adzic. Electrochim. Acta 48 (2003) 3841-3849.

[104] J.J. Zhang, M.B.M.B. Vukmirovic, Y.Y. Xu, M.M. Mavrikakis, R.R.R.R. Adzic. Angewandte Chemie (International ed.) 44 (2005) 2132-2135.

[105] V.S. Bagotzky, E.I. Khrushcheva, M.R. Tarasevich, N.A. Shumilova. J. Power Sources 8 (1982) 301-309.

[106] Y. Kiros. J. Electrochem. Soc. 143 (2005) 2152.

[107] L. Dubau. J. Appl. Electrochem. 33 (2003) 419.

[108] L. Dubau, F. Hahn, C. Coutanceau, J.M. Leger, C. Lamy. J. Electroanal. Chem. 554-555 (2003) 407-415.

[109] R. Kotz, E. Yeager. J. Electroanal. Chem. 111 (1980) 105-110.

[110] M. Chatenet, L. Genies-Bultel, M. Aurousseau. J. Appl. Electrochem. 32 (2002) 1131-1140.

[111] L. Demarconnay, C. Coutanceau, J.M. Leger. Electrochim. Acta 49 (2004) 4513-4521.

[112] D.J. Guo, H.L. Li. Carbon 43 (2005) 1259-1264.

[113] H.-K. Lee, J.-P. Shim, M.-J. Shim, S.-W. Kim, J.-S. Lee. Mater. Chem. and Phys. 45 (1996) 238-242.

[114] N.D. Merkulova, G.V. Zhutaeva, N.A. Shumilova, V.S. Bagotzky. Electrochim. Acta 18 (1973) 169-174.

[115] N.A. Shumilova, G.V. Zhutaeva, M.P. Tarasevich. Electrochim. Acta 11 (1966) 967-974.

[116] K. Smrcek. J. Power Sources 7 (1981) 105-112.

[117] N. Wagner, M. Schulze, E. Gulzow. J. Power Sources 127 (2004) 264-272.

[118] Y. Yang, Y. Zhou. J. Electroanal. Chem. 397 (1995) 271-278.

[119] K. Smrcek, J. Beran, J. Jandera. J. Power Sources 2 (1978) 273-286.

[120] J. Mrha, I. Iliev, A. Kaisheva, S. Gamburzev, M. Musilova. J. Power Sources 1 (1976) 47-56.

[121] M. Appel, A.J. Appleby. Electrochim. Acta 23 (1978) 1243-1246.

[122] I. Iliev, J. Mrha, A. Kaisheva, S. Gamburzev. J. Power Sources 1 (1976) 35-46.

[123] A. Verma, A.K. Jha, S. Basu. J. Power Sources 141 (2005) 30-34.

[124] I. Roche. J. physical chem. 111 (2007) 1434.

[125] J. Yang, J.J. Xu, Electrochem. Commun. 5 (2003) 306-311.

[126] M.L. Calegaro, F.H.B. Lima, E.A. Ticianelli. J. Power Sources 158 (2006) 735-739.

[127] F.H.B. Lima, M.L. Calegaro, E.A. Ticianelli. J. Electroanal. Chem. 590 (2006) 152-160.

[128] F.H.B. Lima, M.L. Calegaro, E.A. Ticianelli. Electrochim. Acta 52 (2007) 3732-3738.

[129] L. Mao. Electrochim. Acta 48 (2003) 1015.

[130] K. Arihara. J. Electrochem. Soc. 151 (2004) A2047.

[131] D. Zhang, D. Chi, T. Okajima, T. Ohsaka. Electrochim. Acta 52 (2007) 5400-5406.

[132] Y.L. Cao, H.X. Yang, X.P. Ai, L.F. Xiao. J. Electroanal. Chem. 557 (2003) 127-134.

[133] K. Matsuki. Electrochim. Acta 31 (1986) 13.

[134] A. Elzing, A. van der Putten, W. Visscher, E. Barendrecht. J. Electroanal. Chem. 200 (1986) 313-322.

[135] S. Sarangapani, P. Lessner, M. Manoukian, J. Giner. J. Power Sources 29 (1990) 437-442.

[136] Y. Kiros, O. Lindstrom, T. Kaimakis. J. Power Sources 45 (1993) 219-227.

[137] C. Mocchi, S. Trasatti. J. Molecular Catalysis A: Chemical 204-205 (2003) 713-720.

[138] H. Tributsch, U.I. Koslowski, I. Dorbandt. Electrochim. Acta 53 (2008) 2198-2209.

[139] V. Hermann, D. Dutriat, S. Muller, C. Comninellis. Electrochim. Acta 46 (2000) 365-372.

[140] R. Manoharan, A.K. Shukla. Electrochim. Acta 30 (1985) 205-209.

[141] A. Weidenkaff, S.G. Ebbinghaus, T. Lippert, M.J. Montenegro, C. Soltmann, R. Wessicken. Crystal Engineering 5 (2002) 449-457.

[142] Y. Kiros, C. Myren, S. Schwartz, A. Sampathrajan, M. Ramanathan. Inter. J. Hydrogen Energy 24 (1999) 549-564.

[143] T. Hyodo, M. Hayashi, S. Mitsutake, N. Miura. J. Appl. Electrochem. 27 (1997).

[144] M. Bursell, M. Pirjamali, Y. Kiros. Electrochim. Acta 47 (2002) 1651-1660.

[145] J. Ortiz, J.L. Gautier. J. Electroanal. Chem. 391 (1995) 111-118.

[146] E. Rios, H. Reyes, J. Ortiz, J.L. Gautier. Electrochim. Acta 50 (2005) 2705-2711.

[147] A. Restovic, E. Rios, S. Barbato, J. Ortiz, J.L. Gautier. J. Electroanal. Chem. 522 (2002) 141-151.

[148] R.N. Singh, J.P. Pandey, N.K. Singh, B. Lal, P. Chartier, J.F. Koenig. Electrochim. Acta 45 (2000) 1911-1919.

[149] T. Nissinen, Y. Kiros, M. Gasik, M. Lampinen. Materials Research Bulletin 39 (2004) 1195-1208.

[150] T. Nissinen, M. Leskela, M. Gasik, J. Lamminen. Electrochim. Acta 427 (2005) 155-161.

[151] T. Nissinen, T. Valo, M. Gasik, J. Rantanen, M. Lampinen. J. Power Sources 106 (2002) 109-115.

[152] K.V. Ramesh, P.R. Sarode, S. Vasudevan, A.K. Shukla. J. Electroanal. Chem. 223 (1987) 91-106.

[153] C.-C. Yang. Inter. J. Hydrogen Energy 31 (2006) 2076-2087.

[154] M. Hayashi, H. Uemura, K. Shimanoe. J. Electrochem. Soc. 151 (2004) A158.

[155] A. Rolla, A. Sadkowski, J. Wild, P. Zoltowski. J. Power Sources 5 (1980) 189-196.

[156] E. Gulzow, M. Schulze. J. Power Sources 127 (2004) 243-251.

[157] M. Sato, M. Ohta, M. Sakaguchi. Electrochim. Acta 35 (1990) 945-950.

[158] K. Tomantschger, R. Findlay, M. Hanson, K. Kordesch, S. Srinivasan. J. Power Sources 39 (1992) 21-41.

[159] N.V. Korovin. Electrochim. Acta 39 (1994) 1503-1508.

[160] Y. Rotenberg, S. Srinivasan, E.I. Vargha-Butler, A.W. Neumann. J. Electroanal. Chem. 213 (1986) 43-51.

[161] T. Burchardt. J. Power Sources 135 (2004) 192-197.

[162] M. Hull, H. James. J. Electrochem. Soc. 124 (1977) 332.

[163] L. Baugh, J. Cook, J. Lee. J. Appl. Electrochem. 8 (1978) 253.

[164] A. Khalidi, B. Lafage, P. Taxil, G. Gave, M.J. Clifton, P. Cezac. Inter. J. Hydrogen Energy 21 (1996) 25-31.

Chapter 3: Experimental setup and characterisation techniques

3.1. Abstract

In this chapter a description of the experimental test setup and characterisation techniques is given. Test cells used to study cathodes made of nickel foam and porous silver membrane are described. The test rig to study nickel foam cathodes in circulating electrolyte mode, is also detailed. Electrochemical impedance spectroscopy (EIS) is outlined giving the basic principles of the technique and showing the advantages of the method in the development of fuel cell electrodes. Basic principles of SEM, BET and XRD are given and the equipment used during this work is introduced.

3.2. General electrochemistry

The electrolyte used in most experiments was a concentrated potassium hydroxide solution (30 wt. % or ~6.9 M) prepared from deionised 18 MΩ cm deionised water (Millipore) and KOH pellets (VWR).

Electrochemical and impedance measurements were performed using a PGSTAT30 potentiostat fitted with a frequency response analyser (FRA, Autolab, Windsor Scientific Ltd., UK). Impedance measurements were performed in potentiostatic mode using a sinusoidal signal of amplitude 0.02 V_{rms} over the frequency range of 10 kHz to 0.01 Hz. Impedance measurements were fitted to equivalent circuit models using the Autolab FRA for windows (version 4.9.004).

All the results presented in this thesis are three electrode measurements using a hydrogen reference electrode (E^o = 0.0V) from Gaskatel (Hydroflex HREF B01) which is suitable for high pH values.

3.3. Test rig set up for nickel substrate cathodes

Half-cell measurements were performed at room temperature using a 2-part housing made from machined epoxy resin using a design originating from Cenergie Corporation. This design emulated the basic functions of a full sized fuel cell in so far that it facilitated circulating electrolyte and flowing air at pressures close to atmospheric. A schematic of the cell housing showing the principal parts is shown in Fig. 3.1 (a). A platinum wire, rolled into a spiral, was used as a counter electrode. Four tie rods and nuts are used to close the cell. A rubber gasket was employed between the cell and the electrode to avoid electrolyte leakage. The seal was obtained by compression of the tie rods on the rubber gasket.

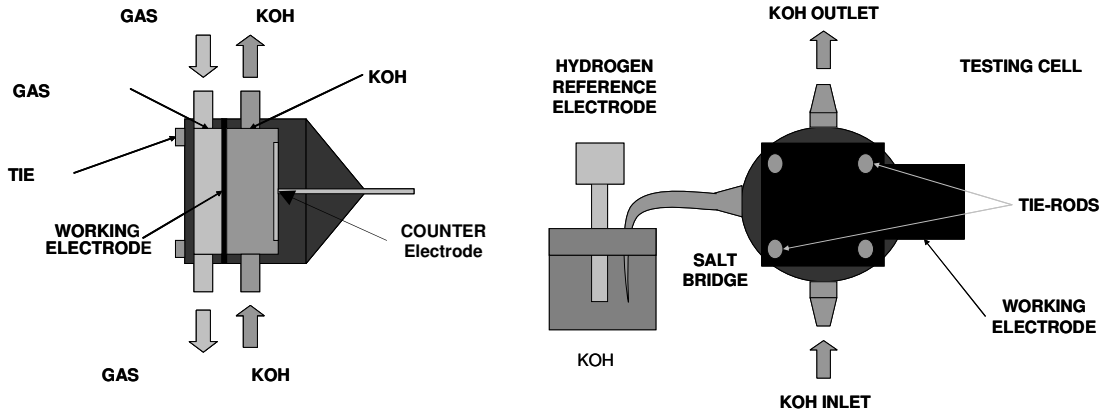


Figure 3.1: Schematic illustration of the test assembly for half-cell measurements: (a) cross section and (b) front view.

The electrode was positioned, as shown on Fig. 3.1 (b), between the electrolyte and gas chamber with the active layer of the electrode facing the electrolyte and the gas diffusion layer facing the gas side. The geometric surface area of the electrode was ~4 cm^2. The current was collected directly via the tag on the working electrode, limiting resistive losses. The hydrogen reference electrode was connected to the cell using an alumina (Al_2O_3) salt bridge. A small aperture, filled with aluminium oxide fibres, was located within one millimetre of the working electrode inside the KOH chamber and connected to the salt bridge. The reference electrode, placed in a special sealed glass

container, was dipped in an electrolyte of the same concentration as that used in the cell.

A special test rig was constructed (Figure 3.2 and 3.3) consisting of a pump and a tank to allow the electrolyte to be circulated through the system. These were mounted on a plastic support with a tray to collect any electrolyte spillage during the change of electrode between two experiments. The tank was made of polypropylene and sealed in order to avoid the reaction of CO_2 from air with the electrolyte. PTFE pipes were used to join the cell, pump and tank. A KOH circulation valve was placed at the inlet of the testing cell in order to control (or stop) the electrolyte flow. The electrolyte was circulated from the bottom to the top of the cell to make sure the electrolyte chamber was completely filled, avoiding trapped air. The gas was also circulated from top to bottom to ensure that any electrolyte passing through the electrode could be drained out of the cell.

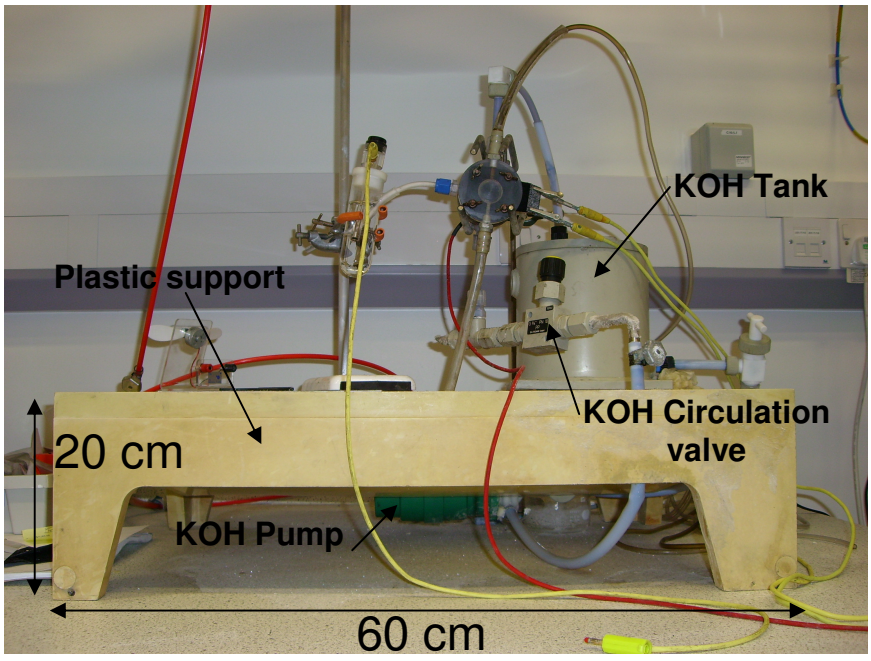


Figure 3.2: Picture of the circulating electrolyte test rig.

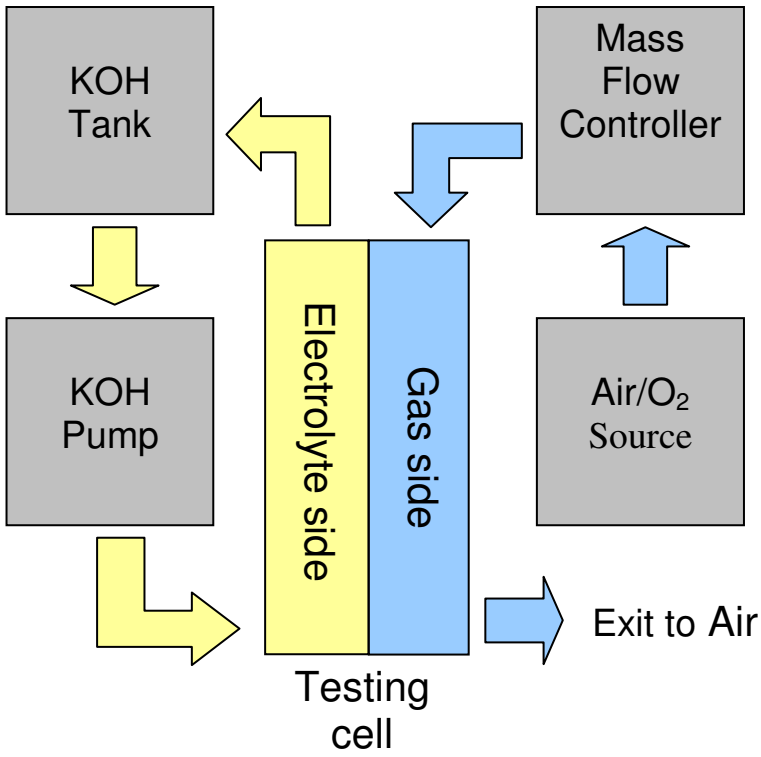


Figure 3.3: Flow diagram of the circulating electrolyte test rig.

The cell was mounted in a rig to allow the electrolyte to be circulated through the system at a flow rate of 100 ml min^{-1}. No effect on performance was found by increasing KOH flow rate as shown in Fig 3.4. As can be seen, best performance was found without circulation of the electrolyte. Air flow was controlled by a mass flow controller (Bronkhorst Hi-Tec) set to 500 ml min^{-1} for all experiments, which was sufficient to avoid any pronounced mass transport effect (Fig 3.5). The electrolyte was circulated from the bottom to the top of the cell to make sure the electrolyte chamber was completely filled, avoiding trapped air. The gas was also circulated from top to bottom to ensure that any electrolyte passing through the electrode could be drained out of the cell.

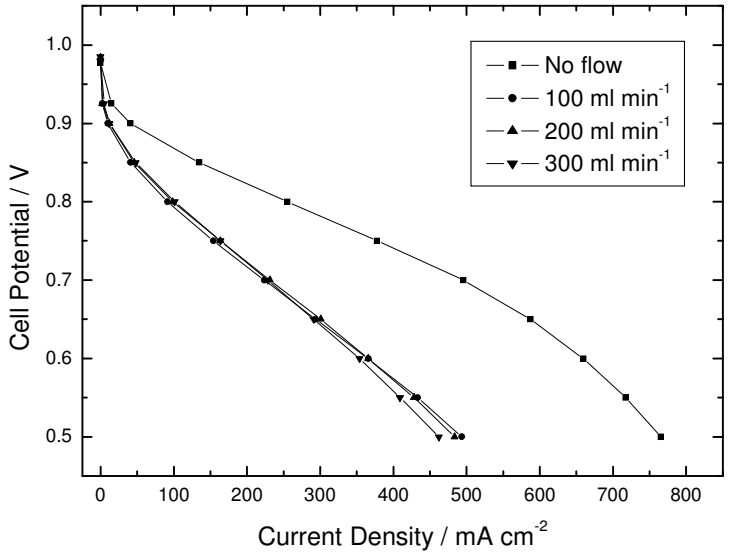


Figure 3.4: Effect of KOH flow rate on Cath4 performance.

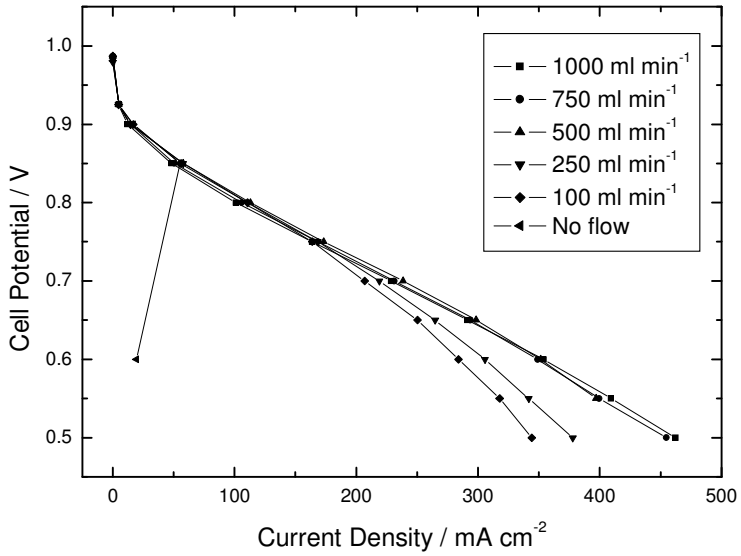


Figure 3.5: Effect of air flow rate on Cath4 performance.

3.4. Testing cell for porous silver membrane cathodes

Electrochemical experiments on porous silver membranes cathodes were carried out in a standard three-compartment cell with a Luggin capillary arrangement as shown in Fig. 3.6. The counter electrode was made of nickel foam which was 10 times the geometrical surface area of the working electrode to avoid excessive polarization. Silver membrane cathodes (1 cm^2) were floated on the surface of a fresh KOH solution with the top side exposed to an oxygen or air atmosphere through forced convection. Measurements were collected directly via the vertical tip of the working electrode by the means of a crocodile clip which was inserted in a pipette. When used, O_2 was provided via the pipette.

The fuel cell testing was carried out in a home-made cell consisting of hydrogen and electrolyte chambers, as shown in Fig. 3.7. The seal between the two chambers was achieved using a rubber gasket. A commercial hydrogen electrode from Alfa Aesar was used as the anode. Potential measurements were made directly on the silver membrane cathode and on the tag of a nickel mesh placed in contact of the back of the anode. A plastic mesh (1 mm) was put between the cathode and the anode filled with KOH solution. The cell was open to atmosphere on the cathode side being in a self-breathing mode.

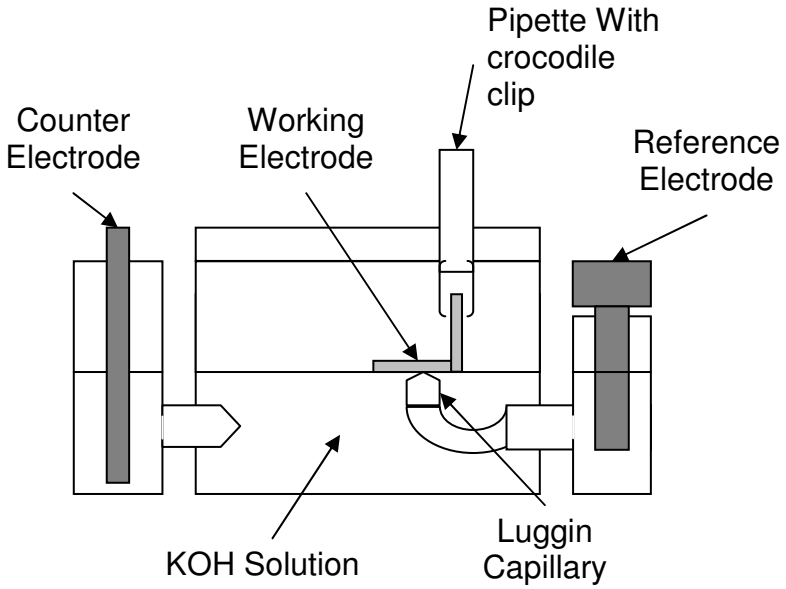


Figure 3.6: Three-compartment electrochemical cell.

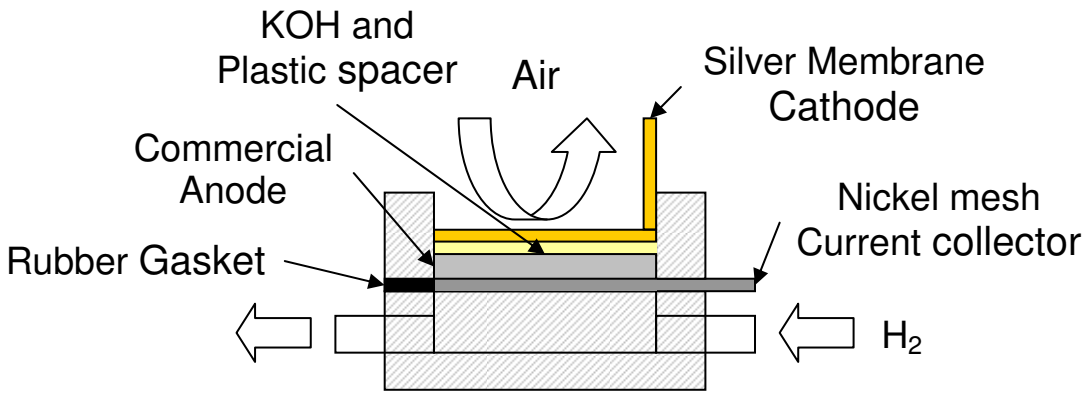


Figure 3.7: Fuel cell testing set up.

3.5. Electrochemical impedance spectroscopy (EIS) technique

EIS was employed as the main investigation technique, alongside DC polarization measurements, to assess cathode performance. Impedance measurements allow the characterisation of the bulk electrode (e.g. conductivity), the electrode/electrolyte interface (e.g. charge transfer resistance and capacitance of the double layer), and mass transport behaviour, making this a powerful tool for electrode development. This technique can contribute to the interpretation of fundamental electrochemical and electronic processes leading to insights about the factors limiting electrode performance.

The fundamental approach of all impedance methods is to apply a small amplitude sinusoidal stimulus (voltage or current) to the system under investigation and measure the associated response. The amplitude of the stimulus must be kept small enough that the response of the system operates in a pseudo-linear regime [1]. There are different ways of applying the stimulus but the most common is to work in the frequency domain, using a single frequency signal. The advantage of this method is the availability of commercial instruments. It also gives a good signal-to-noise ratio in the frequency range of interest. However, the technique is limited by measurement speed.

It is not suitable for a fast changing system since the measurement takes time to sweep across a range of frequencies.

In the single frequency method, a sinusoidal signal is applied where the response is a complex quantity which is similar in frequency but shifted in phase and different in amplitude. The impedance of the system can be calculated using Ohm's law as,

$$Z(\omega)=\Delta E(\omega)/\ \Delta I(\omega) \qquad 3.1$$

By varying the frequency of the applied signal, the impedance of the system can be determined as a function of frequency. The results are plotted on a Nyquist plot where real and imaginary parts are given as function of frequency as shown in Fig. 3.8.

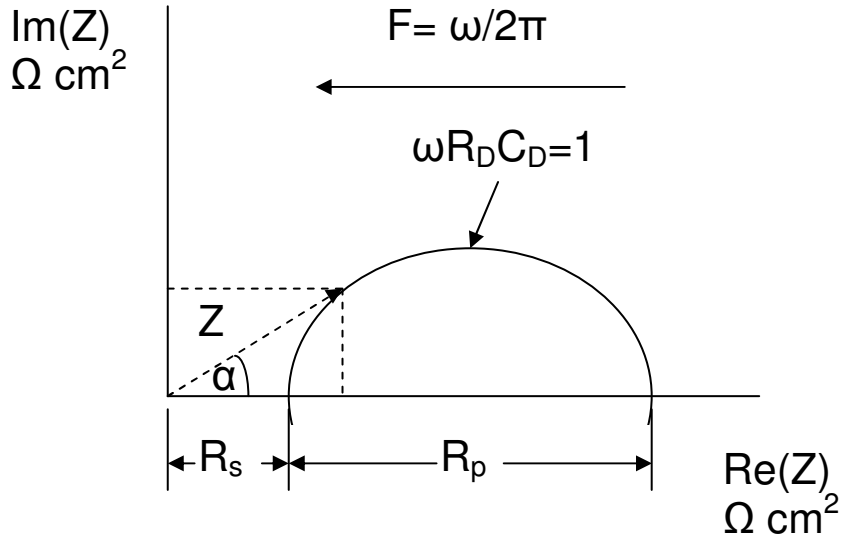


Figure 3.8: Schematic illustration of the Nyquist plot.

While plotting data in the Nyquist format the real axis must be equal in length and unit to the imaginary axis, so as not to distort the shape of the curve which is important for qualitative interpretation of the data. An alternative way of presenting the data is to plot, on a same graph, the absolute value of impedance and the phase shifts (α) as a function of frequency; this representation is called a Bode plot.

In order to explain, understand and extract physically meaningful properties of the system, experimental data are modelled or fitted to an equivalent circuit composed of ideal resistors (R), capacitors (C) and inductors (L). A resistor can represent the bulk resistance of a material such as the resistance of the electrolyte to ion transport, the resistance of a conductor to electron transport, or the resistance to the charge-transfer step at the surface of the electrode. Capacitors and inductors are associated with space-charge polarization regions such as electrochemical double-layer and adsorption processes at the electrode surface. The impedance of a circuit with multiple elements can be calculated using the same rules as with multiple resistors. The total impedance of two elements in series is the sum of the impedances of the individual elements. In the same way, the impedance of two elements in parallel is given by the sum of the inverse impedances of the individual elements.

The use of ideal elements to describe the characteristics of a real electrochemical system is limited by the fact that the properties of materials can be distributed and that the electrode–electrolyte interface is often non-homogeneous. Under this condition, a constant phase element (CPE) is introduced to mimic the distributed nature of the element. The impedance of a constant phase element is given by Eq. 3.2:

$$Z_{CPE} = \frac{1}{Yo(j\omega)^n} \qquad 3.2$$

Where Y_0 is the admittance relating to the double-layer capacitance and n is a constant between -1 and 1 giving information about the nature of the CPE. When n=1, Y_0 corresponds to the ideal capacitance C and the CPE behaves as an ideal capacitor.

A resistance in series with a resistance, itself in parallel with a capacitance (or CPE), is one of the simplest and most common models. It is called the Randles circuit and includes a solution resistance, a double-layer capacitor and a polarization resistance (Fig. 3.9) [1]. It is often the starting point for more complex models.

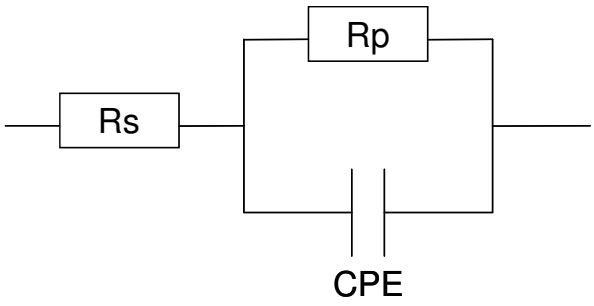


Figure 3.9: Equivalent circuit: the Randles circuit.

3.6. Other characterization techniques

In this work, surfaces of the different substrates were observed with a scanning electron microscope (JEOL JSM-5610LV). The scanning electron microscope (SEM) uses a beam of electrons to scan the surface of a sample to build a three-dimensional image of the specimen. The interaction of the electrons with the atoms that make up the sample also produces a variety of signals including secondary electrons (electrons from the sample itself), backscattered electrons (beam electrons that bounce off nuclei of atoms in the sample), X-rays, light, heat, and even transmitted electrons (beam electrons that pass through the sample) that contain information about chemical compositions, crystalline structure and crystal orientation. A SEM (Fig. 3.10) consists of an electron gun which generates the beam of electrons which typically has an energy ranging from a few hundred eV to 40 keV. The beam is focused by one or two condenser lenses to a spot about 0.4 nm to 5 nm in diameter. It then passes through pairs of scanning coils, which deflect the beam in the *x* and *y* axes so that it can scan line by line a rectangular area of the sample surface. Several detectors are mounted in the chamber to view the different electron signals from the sample.

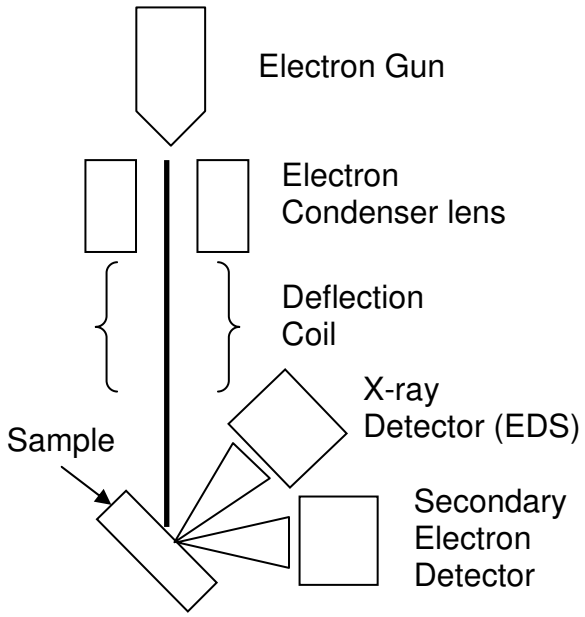


Figure 3.10: Schematic drawing of the SEM.

The most widely used technique for estimating surface area is the so-called BET method (Brunauer, Emmett and Teller). BET measurements were performed using a TriStar 3000 gas adsorption analyzer. The BET technique gives information about surface area and porosity of a material using physical adsorption and capillary condensation principles. A sample is cooled to cryogenic temperature, and then is exposed to analysis gas at a series of precisely controlled pressures. With each incremental pressure increase, the number of gas molecules adsorbed on the surface increases. Any micropores in the surface are filled first, then the free surface becomes completely covered, and finally the larger pores are filled by capillary condensation. Commonly, a desorption process begins in which pressure systematically is reduced resulting in liberation of the adsorbed molecules. As with the adsorption process, the changing quantity of gas on the solid surface at each decreasing equilibrium pressure is quantified. These two sets of data describe the adsorption and desorption isotherms. Analysis of the shape of the isotherms yields information about the surface and internal pore characteristics of the material.

X-ray diffraction (XRD) results were obtained using an automated powder diffractometer, Philips PW1700 series, using Cu K α radiation at 40 kV / 40 mA with a secondary graphite crystal monochrometer. The basic principle of XRD is

simple: a beam of X-rays hits a sample and diffracts into many specific directions. From the angles and intensities of these diffracted beams different information can be determined such as the arrangement of atoms within a crystal as well as their chemical bonds.

In this chapter, experimental setups have been described and characterisation techniques briefly introduced. More information on electrode fabrication is given in the experimental sections of each chapter.

3.7. References

[1] E. Barsoukov, J. R. Mcdonald. Impedance spectroscopy theory, experiment, and applications. John Wiley & Sons: New Jersey (2005).

[2] Southampton Electrochemistry group. Instrumental methods in electrochemistry. Ellis Horwood: England (1990).

[3] C. Hamann, A. Hamnett, W. Vielstich. Electrochemistry. Wiley-VCH: Weinheim (1998).

Chapter 4: Development of a cathode using nickel Foam as a substrate material

4.1. Abstract

The use of nickel foam as an electrode substrate in alkaline fuel cells (AFCs) has been investigated for bipolar cells incorporating an electrically conducting gas diffusion layer. This contribution focuses on the cathode, and draws comparisons between nickel foam and nickel mesh substrates. One of the principal electrocatalysts for the cathodic reduction of oxygen is silver, so an improvement in electrochemical performance was obtained by electroplating the nickel foam with silver. The electrodeposition process was optimised to maximise electrochemical performance with a minimum of silver deposited. Nickel foam, which is less expensive than the usual nickel mesh, appears to be a good substrate for AFC electrode fabrication, especially when incorporating a conducting gas diffusion layer. Silver deposited by electroplating onto the nickel foam was found to result in significantly enhanced electrochemical performance, with a reduction in both the Ohmic resistance of the electrode, as well as the oxygen reduction reaction charge transfer resistance.

4.2. Introduction

Recently, there has been a resurgence of interest in alkaline fuel cells (AFCs) [1-7], partly because they have the potential for lower cost in mass production [8, 9] than other types of low temperature fuel cells. AFC systems, which have been successfully used in space applications for decades [10], need to meet the challenging requirements of low cost, high performance and durability to be successful in terrestrial applications; improvement in electrode performance is a necessary step towards this goal. AFC cathodes consist of several PTFE-bonded carbon layers applied onto a metal mesh which is used as the current collector [11]. The catalyst is supported on a carbon substrate; usually a high surface area carbon black [12]. The oxygen reduction reaction in alkaline media is more facile than in acid media, making the use of less expensive catalyst materials in place of platinum possible; this opens an opportunity for new electrode designs [13]. AFC stacks have generally favoured mono-polar

construction, which uses a non-conducting PTFE based gas diffusion layer bonded onto the backside of a nickel mesh. Very few systems have been built with bipolar construction as is the norm for polymer electrolyte fuel cells (PEFCs). In the present study, we have developed a conducting gas diffusion layer (GDL) which is suitable for bipolar operation. The GDL is based on a PTFE bonded carbon black layer which is applied to the nickel substrate. The relative merits of metal mesh versus metal foam are made in the course of this study.

Nickel, in the form of mesh, is predominantly used as an electrode substrate in AFCs because it is highly conductive and corrosion resistant to KOH. However, nickel mesh is a relatively expensive component. One of the aims of this work was to investigate lower cost nickel substrates such as nickel foams.

Nickel foam has a lower weight-to-surface ratio and is consequently less expensive than nickel mesh (Table 4.1). The weight and cost of the electrodes in an AFC stack are two crucial parameters which have to be reduced. Based on these two parameters, it is clear that nickel foam has an advantage over the commonly used nickel mesh.

Parameters	**Nickel mesh**	**Nickel foam**
Weight-surface ratio (g cm^{-2})	0.0415	0.0366
*Price ($\$ m^{-2}$)	60	20

* Quotations were obtained in 2008 for 4000 m^2 of material from suppliers

Table 4.1: Weight and price comparison of nickel mesh and nickel foam.

Metal foams, which can be manufactured from numerous metals and metal alloys by a wide variety of vapour, liquid and solid-state processes, have been extensively characterized in recent years [14-18]. Nickel foam can be mass produced in a continuous process in which a coating of nickel is applied by electroplating or chemical vapour deposition onto a reticulated polymer substrate, usually made from polyurethane foam. The plastic former is then burnt out using a high temperature sintering step, resulting in an open-cell skeletal structure of hollow metal limbs [19, 20]. This open-cell nickel foam is very attractive due to its high porosity, high mechanical strength, high specific surface area, low density, corrosion resistance and good electrical conductivity.

During the past decade, nickel foams have been used in battery applications as a substrate for pasted nickel electrodes [21-26]. More recently, the deposition of coatings onto nickel foams has been shown to increase their oxidation resistance [27, 28] or their catalytic activity in diverse chemical processes [29-31]. Deposition techniques including: electrodeposition [30, 32, 33], electroless deposition [34, 35], and impregnation methods followed by thermal treatment [29, 36] have all been demonstrated with nickel foam.

Yang *et al*. have studied silver and palladium-silver coated nickel foam cathodes prepared by electrodeposition, and these appear to be suitable for practical metal-hydrogen peroxide fuel cells [37, 38]. Hydrogen evolution cathodes have been investigated as a means of hydrogen production from water electrolysis [32, 33] or from chemical hydrides such as sodium borohydride [34].

The use of nickel foam (compared to nickel mesh) in supercapacitor electrodes has shown that the open structure of the three-dimensional current collector considerably reduces the internal resistance of the electrode by improving the electronic contact between the activated carbon and the collector [39]. Nickel foam has properties which are also well suited for fuel cell electrode development; these properties are particularly useful in AFCs in which the foam can provide both catalyst support, mechanical support and a means of current collection. However, to our knowledge, the use of nickel foam as catalyst support and electrode substrate for AFCs has not been investigated.

4.3. Experimental

4.3.1. Electrode Preparation

The electrode substrates used in this work were nickel foam (purity: 99.9%, pore per inch: 110, density: 380 g m^{-2}, average pore size: 590 μm, thickness: 1.7 mm) from INCO (Dalian) Co. Ltd, an SEM picture of which is shown in Fig. 4.1. The nickel mesh was from Fuelcellmaterials.com (40 x 40 mesh x 0.13 mm wire diameter).

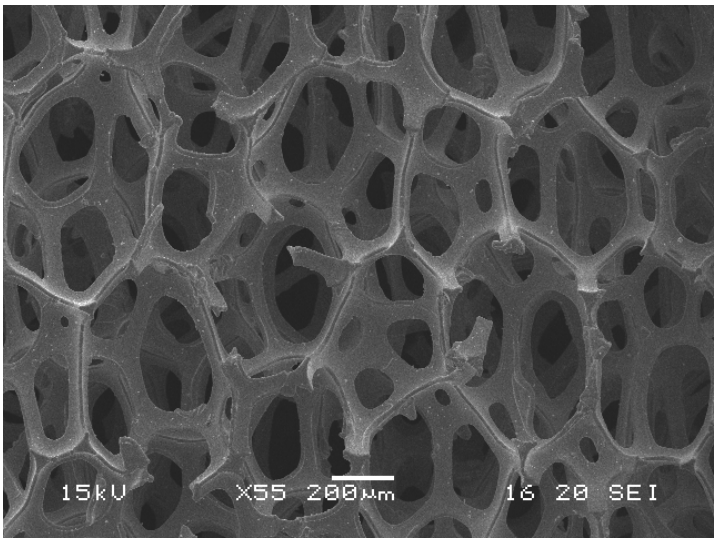


Figure 4.1: Scanning electron microscope image showing the open structure of the nickel foam.

Silver is one of the most active catalysts for the oxygen reduction reaction (ORR) in alkaline media [40] and has the highest electrical conductivity of any element. Silver plating was accomplished on samples of size 50×90 mm using a series of plating baths. Plating chemicals were provided by Balco Ltd (UK). Between each bath the substrate was washed with de-ionized water and then dried. To ensure an even deposition, the substrate was electrochemically cleaned in an alkaline solution. Then, a very thin strike layer (low concentration of silver potassium cyanide) of pure silver was deposited onto the clean substrate to ensure good adherence of the thicker layer of silver which was subsequently deposited in a heavy silver bath (high concentration of silver potassium cyanide). Two anodes at equal distance (3 cm) from the substrate were used to obtain an even deposition. In the strike bath, stainless steel anodes were used whereas pure silver anodes provided the silver in the heavy bath. The silver electroplating conditions (voltage and immersion time) applied in this work were advised by the chemical provider and are summarized in Table 4.2.

BATH	Voltage (V)	Time (s)
Electro-cleaning	5	30
Strike	3	10
Heavy	2	60

Table 4.2: Silver electroplating conditions.

The final silver thickness can be readily determined from the current and time used in the heavy bath and can be easily controlled owing to the high Faradaic efficiency associated with silver cyanide solutions. The amount of silver deposited onto the nickel foam as a function of electrolysis time in the heavy bath using the conditions quoted above is shown in Fig. 4.2. The actual amount of silver deposited was obtained by weighing the sample before and after electroplating. A linear relation was obtained which could be fitted to the data shown in Fig.4.2.

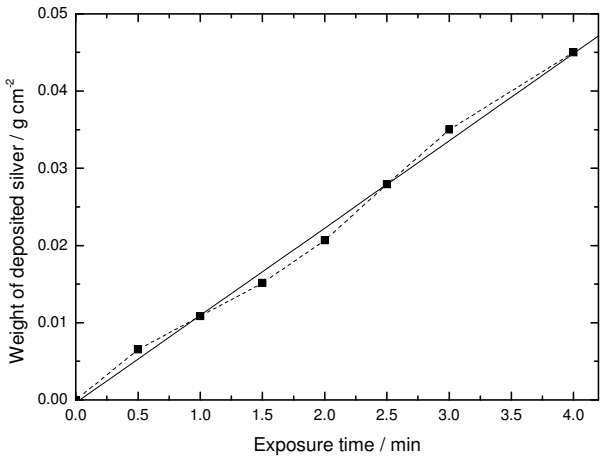


Figure 4.2: Amount of deposited silver as a function of electroplating time in the heavy bath (plating conditions 2 V, 5.8 A).

A gas diffusion layer (GDL) was prepared with carbon black (Printex XE2 BET surface 950 m^2 g^{-1}, average primary particle size 35 nm) from Degussa which was selected for its high surface area. PTFE suspension (TE3893-N solution 59.94% solid) from Alfa chemicals and propan-2-ol from VWR, which facilitate the GDL rolling onto the substrate, were mixed and stirred with the carbon black until a homogeneous paste was obtained. The PTFE solution:carbon black ratio was 2.5:1.

To prepare each electrode, both the silver plated foam and the nickel foam (80×50 mm) were pressed to obtain a thickness of ~0.3 mm. The GDL mixture was rolled to 0.5 mm thickness with a calendering machine on grease-proof paper. The foam was put on top of the GDL and rolled to a thickness of 0.5 mm. The GDL was then cut to size. Finally, the electrode was pressed at 20 bars for 2 minutes to remove excess liquid. The electrode was then sintered in air at 255°C for 30 min

4.3.2. Electrode characterization

The catalytic activity of the various nickel substrates was measured by immersion in fresh KOH solution which was saturated with air or argon by bubbling for 30 min. During measurements, gas was turned off. The geometric surface area for each electrode (≈ 1 cm^2) was measured, and results were normalised to this. A three electrode set up with a Luggin capillary was used; the counter electrode was a piece of nickel foam which was 10 times the geometrical surface area of the working electrode, to avoid excessive polarization as described in Chapter 3.

4.4. Results and discussion

4.4.1. Nickel mesh vs. nickel foam

Polarization curves, for both nickel mesh and nickel foam in aerated KOH solution, were obtained and can be seen in Fig. 4.3. The Ni foam is observed to clearly outperform the Ni mesh.

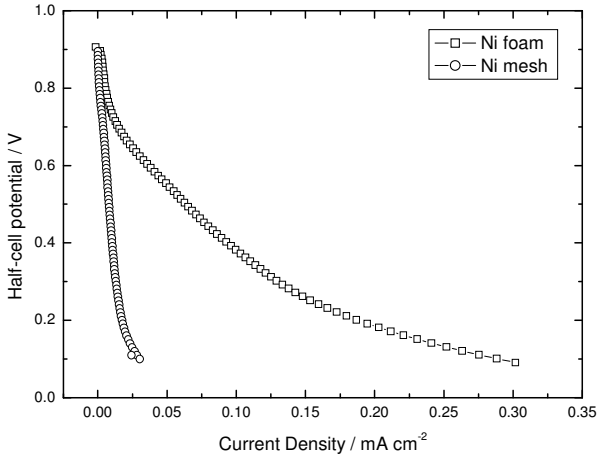


Figure 4.3: Polarization curves of nickel foam and nickel mesh in aerated 32 wt% KOH solution.

Impedance measurements (Fig. 4.4) show one capacitive arc for both substrates, with the arc of the Ni foam being much smaller than that of the Ni mesh. These results were fitted using the simple equivalent circuit shown in Fig. 4.5, where Rs, Rp and CPE are the Ohmic resistance, the charge transfer resistance and the constant phase element representing the double layer capacitance.

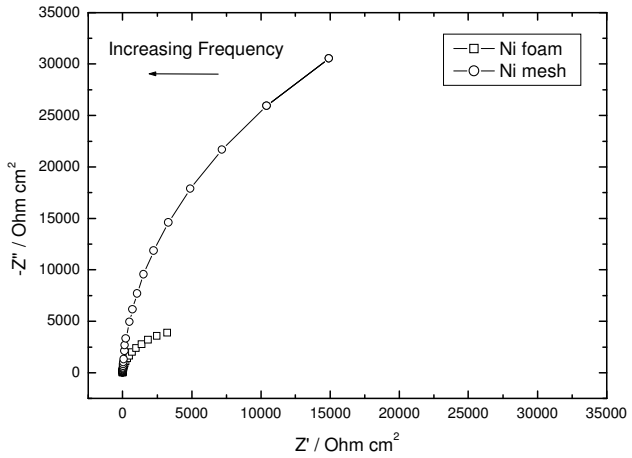


Figure 4.4: Impedance diagram of nickel foam and nickel mesh in aerated 32 wt% KOH solution at 0.6 V (cell voltage) frequency range 10 kHz to 0.01 Hz.

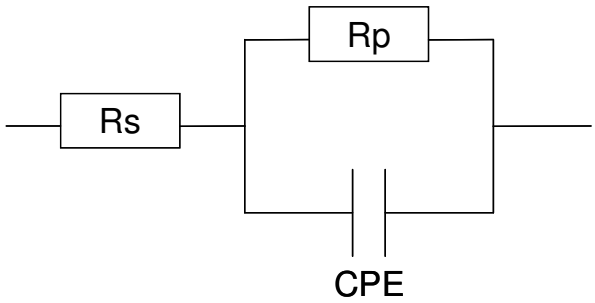


Figure 4.5: Equivalent circuit of the nickel mesh and foam electrode for the impedance spectra.

Results from the fitting of the curves in Fig. 4.4 are given in Table 4.3; it can be seen that the nickel foam Ohmic resistance Rs, is higher than the nickel mesh value, which was expected since nickel mesh contains more nickel mass than nickel foam. The

lower value of Rp and larger value of the CPE for the Ni foam would suggest that there is a greater surface area in contact with the electrolyte than there is for the Ni mesh which seems to be predominant over Rs for good performance.

Substrate	**Rs** (Ω **cm^2**)	**Rp** (Ω **cm^2**)	**CPE** **(Farad)**
Nickel foam	1.32	$4.45 \times 10^{+3}$	1.56×10^{-4}
Nickel mesh	0.609	$2.82 \times 10^{+4}$	4.63×10^{-5}

Table 4.3: Values of equivalent circuit parameters for nickel foam and nickel mesh.

4.4.2. Characterization of nickel foam

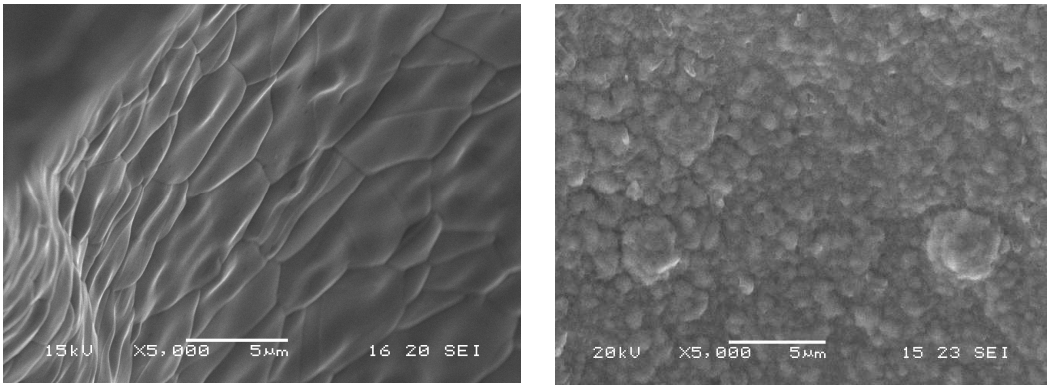
Table 4.4 summarizes results of different measurements made on nickel foam. The density was determined by weighing a known geometric volume of foam. The same technique was used to find the mean porosity, knowing the density of nickel. The electrical resistivity was deduced from the slope of current-voltage plots obtained with a four-point measurement method at 20°C. Results are in good agreement with reports from other workers on similar nickel foams [16].

Parameter	**Nickel Foam**
Density (kg m^{-3})	220
Mean Porosity	0.975
Electrical Resistivity (Ω m)	1.09×10^{-5}

Table 4.4: Key characteristics of the nickel foam at 20°C.

4.4.3. Characterization of silver plated nickel foam

SEM images of the nickel foam surface before and after silver deposition are shown in Fig. 4.6. As can be seen, the nickel foam surface shows a granular texture (Fig. 4.6a). The silver coating is a uniform film of fine grains in the µm range (Fig. 4.6b).



(a) (b)

Figure 4.6: SEM pictures of (a) the Ni foam surface and (b) the Ni foam surface after silver plating (Silver loading: 11 mg cm^{-2}).

Fig. 4.7 presents the X-ray diffractograms in the 2θ range 30-80° comparing the bare nickel substrate to the silver plated case. As can be seen, diffraction peaks corresponding to silver replace those of nickel. However, some nickel is still observed in the composition of the silver plated foam. This nickel peak was probably picked up from under the thin silver coating (estimated at 3 µm for a silver loading of 11 mg cm^{-2}) which appeared uniform from the SEM pictures.

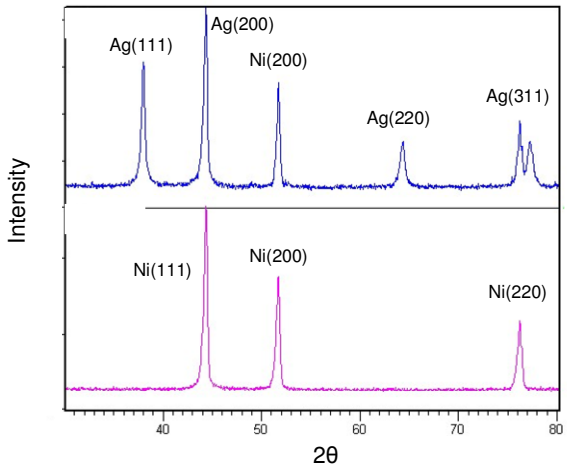


Figure 4.7: XRD of nickel foam (bottom) and silver plated nickel foam (top).

Underpotential deposition (UPD) is a technique which appears to give well-defined surface structures at sub- and full-monolayer coverage [41]. Lead, which deposits on silver but not on nickel (Fig. 4.8), was used to determinate the surface area of the silver plated nickel foam. The UPD of lead on silver has been well studied and described by Kirowa-Eisner *et al*. [1, 42-44]. A similar method was used in this work where the cyclic voltammogram (CV) resulting from the UPD on silver plated nickel foam is shown in Fig. 4.9. The area under the anodic peak was used to determine the surface area of the silver, which was found to be 0.0324 m^2 g^{-1}. This is in good agreement with results obtained from the BET technique which was 0.0292 m^2 g^{-1}.

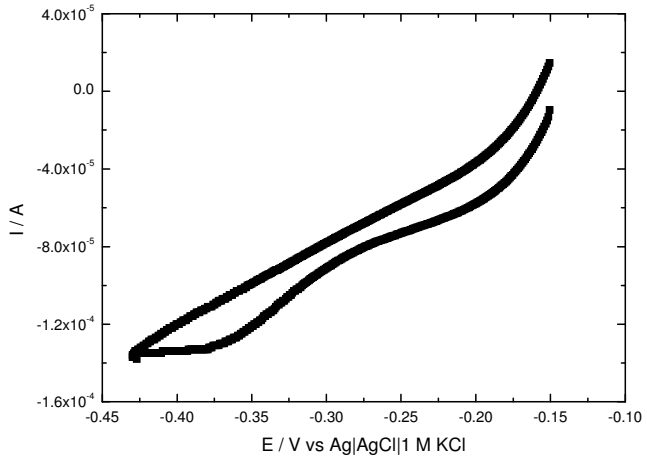


Figure 4.8: Cyclic voltammogram for UPD formation of Pb on nickel foam, υ = 1 mV s^{-1}; 12 mM Pb $(NO_3)_2$ and 100 mM HCl solution.

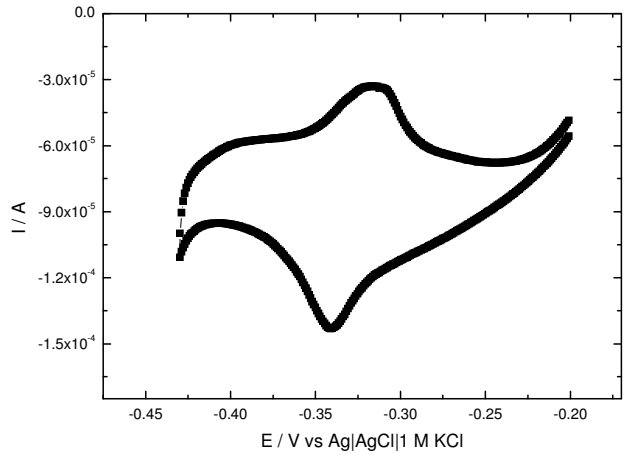


Figure 4.9: Cyclic voltammogram for UPD formation of Pb/Ag on silver plated nickel foam (silver loading: 11 mg cm^{-2}), υ = 1 mV s^{-1}; 12 mM $Pb(NO_3)_2$ and 100 mM HCl solution.

The electrical resistivity of silver plated nickel foam with different silver loadings was calculated from the slope of current-voltage lines obtained with a four-point measurement method at 20°C, as shown in Fig. 4.10. Uncoated nickel foam is included as a reference. The slope of the line, and thus the electrical resistivity of the substrate, decreased with increasing silver loading. Up to silver loadings of 15 mg cm^{-2}, the conductivity improvement is significant and the electrical resistivity was 4.13×10^{-6} Ω m, 2.5 times less than the uncoated nickel foam.

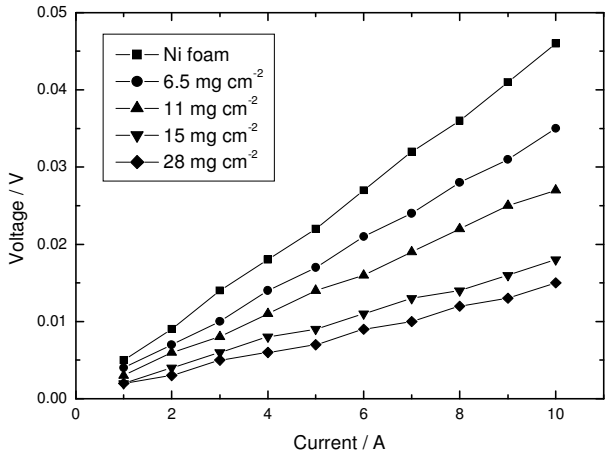


Figure 4.10: Current-voltage lines showing the electrical resistivity of the uncoated nickel foam, and the silver plated nickel foam with different silver loadings.

In order to examine the electrochemical performance of nickel foam and silver plated nickel foam toward the oxygen reduction reaction (ORR), polarization curves were obtained using an aerated KOH solution. As can be seen in Fig. 4.11, at high overpotential, the silver coating greatly improves the performance of the substrate for ORR. The relatively low active surface area of the foam limits the current generated by the ORR to a few mA cm^{-2}. It is clear that the silver coating further improves the foam's performance compared to the uncoated Ni case. The optimum silver loading for the electrochemical performance was found to be 11 mg cm^{-2} since increasing the loading of silver beyond this did not result in any significant improvement in performance. The experiment has been reproduced several times showing the same trend as in Fig. 4.11; the bare nickel foam without activity and two distinct groups (6.5/8.5 mg cm^{-2} and 11/15/21 mg cm^{-2}) with almost the same performance. The adding cost of the silver, considering the cost of the silver in January 2010, would be 40 \$ m^{-2} which corresponds of the difference in price between nickel mesh and nickel foam.

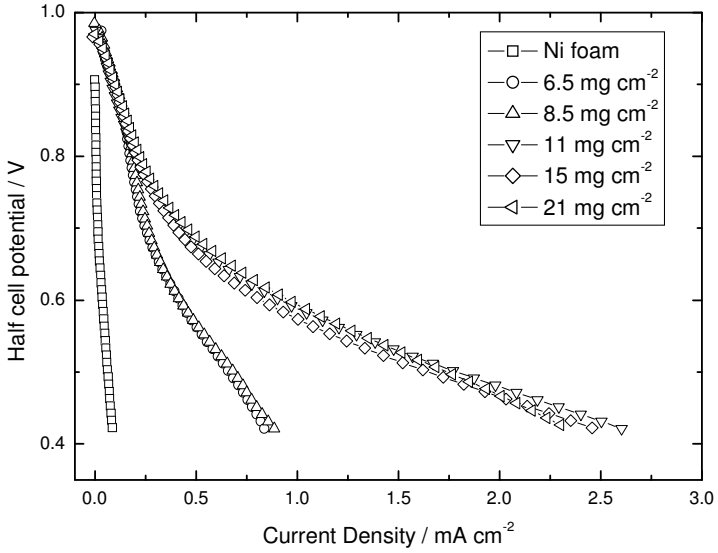


Figure 4.11: Effect of silver loading on the electrochemical performance of nickel foam in aerated 32 wt. % KOH solution.

The electrochemical performance of the silver plated nickel foam with loading of 11 mg cm^{-2} is better than for the 6.5/8.5 mg cm^{-2}. This is thought to be due to non-uniform plating at the lower silver loading which is evident from the SEM image that shows a defective surface covering (Fig. 4.12). This lack of silver is believed to increase the resistivity of the substrate decreasing performance.

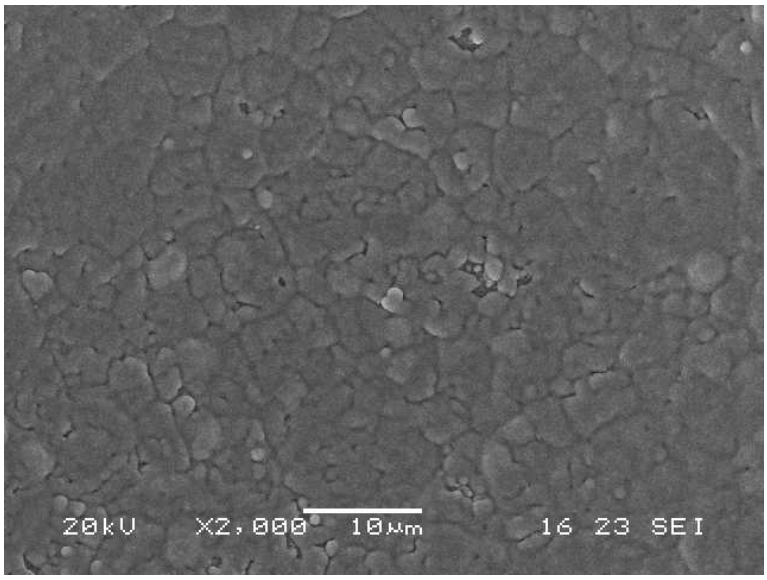


Figure 4.12: SEM pictures of the Ni foam surface after silver plating (Silver loading: 6.5 mg cm^{-2}).

Impedance measurements were made in aerated KOH solution on uncoated nickel foam and silver plated nickel foam with loading of 11 mg cm^{-2} (Fig. 4.13). Results obtained were fitted to the equivalent circuit shown in Fig. 4.5. We can see from the results summarized in Table 4.5 that the capacitance of nickel foam is much smaller than that of silver plated foam. This is attributed to a surface roughness effect which is apparent from the SEM pictures shown in Fig. 4.6, where the silver surface appeared much rougher than the bare nickel foam surface. The silver coating, when uniformly deposited (as is the case with the silver plated nickel foam at a loading of 11 mg cm^{-2}), also appeared to reduce greatly both the Ohmic and charge transfer resistance.

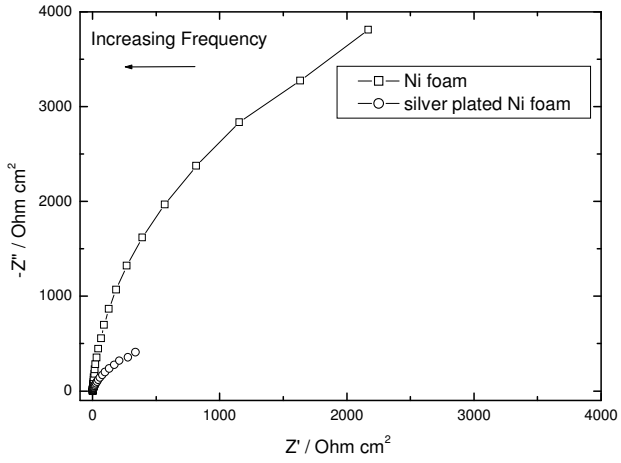


Figure 4.13: Comparison between the EIS response for nickel foam and silver plated nickel foam (11 mg cm^{-2}) at 0.6 V (cell voltage) in 32 wt. % KOH solution from 10 kHz to 0.01 Hz.

Substrate	**Rs** (Ω **cm²**)	**Rp** (Ω **cm²**)	**CPE** **(Farad)**
Nickel foam	1.32	$4.45 \times 10^{+3}$	1.56×10^{-4}
Ni Foam silver loading: 11 mg cm^{-2}	0.124	$9.45 \times 10^{+2}$	1.62×10^{-3}

Table 4.5: Values of equivalent circuit parameters for nickel foam and silver plated nickel foam (11 mg cm^{-2}).

4.4.4. Characterization of fuel cell gas diffusion cathodes

Nickel foam and silver plated nickel foam were used to prepare fuel cell cathodes containing the gas diffusion layer following the procedure described in the experimental section. Measurements were taken after 30 min of conditioning at 0.7 V (cell voltage) under air flow**.** The half cell polarization curves obtained for the cathodes in Fig. 4.14 clearly show an improved performance for the Ag coated Ni foam over that of the cathode prepared using the uncoated Ni foam. The addition of the gas diffusion layer has also significantly increased the current density in both cases compared with the bare metal electrodes. This is due to the much improved three-phase boundary contact associated with the very high surface area of carbon black in the GDL. At overpotentials below ~200 mV there is little difference, and the improved catalytic activity for the ORR due to the silver on the nickel foam cannot be seen due to the relatively low surface area of the foam (0.03 m^2 g^{-1}) compared to the carbon black (950 m^2 g^{-1}); i.e. the contribution made by the foam to fuel cell cathode performance is not significant in this region. At overpotentials > 200 mV, the improved performance comes from the reduced Ohmic drop due to the silver coating which improved the conductivity of the substrate.

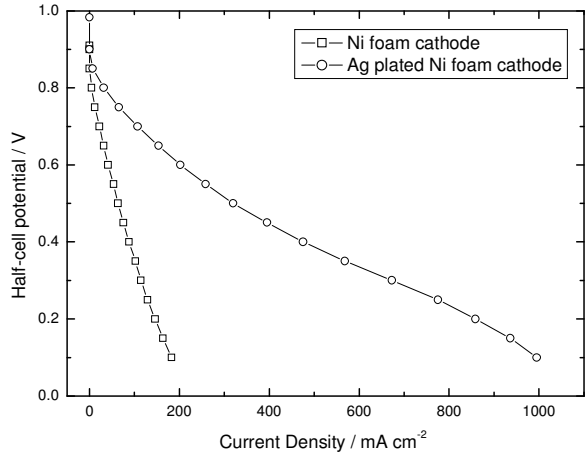


Figure 4.14: Polarization curves of cathodes made of nickel foam and silver plated nickel foam (loading: 11 mg cm^{-2}) under air at 25°C in 32 wt. % KOH solution.

Impedance measurements were performed on a cathode made using silver plated nickel foam (Fig. 4.15), and a cathode made of nickel foam (Fig. 4.16) in order to investigate why the addition of a layer of silver on the nickel foam improved performance. Measurements were made at different potentials for both electrodes. As can be seen in Fig. 4.15, the cathode made of silver plated nickel foam shows one capacitive semi-circle and one inductive loop at low frequencies. Similar results have been found by Thiele *et al*. on a gas diffusion electrode made of perovskite catalyst and carbon nanotubes [45]. At high electrode potential (above 0.5 V), the higher the polarization the smaller the semi-circle; this is related to the impact of electrode polarisation on the charge transfer resistance. At low electrode potential (below 0.4 V), the semi-circle increases, which is associated with mass transport limitations. This is especially expected when using air. Both charge transfer and diffusion processes are taking place simultaneously when the electrode is under working conditions, but at high electrode potential the capacitance is mainly due to charge transfer resistance. The impact of the diffusion processes becomes more important at high polarization, especially when using air. The inductive loop at low frequencies has been ascribed in the literature to the carbon support upon which intermediate species are adsorbed [46, 47].

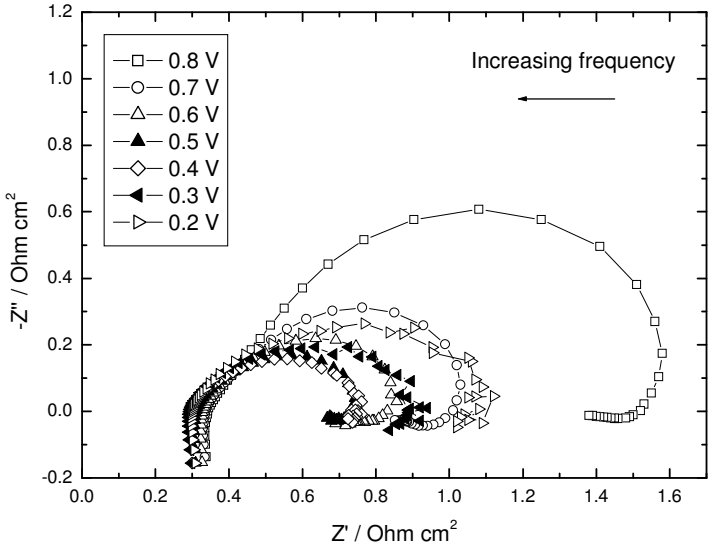


Figure 4.15: Impedance measurements over a range of electrode voltages of a cathode made of silver plated nickel foam (loading: 11 mg cm^{-2}) under air at 25°C in 32 wt. % KOH solution from 10 kHz to 0.01 Hz.

It can be seen in Fig. 4.16 that the shape of the impedance spectra for the cathode made of nickel foam is different from the silver plated impedance spectra. Two arcs and one inductive loop at low frequencies are visible at cell polarisations between 0.2 and 0.6 V. Two capacitive semi-circles and one growth of the lower frequency loop are visible at cell polarisations of 0.7 and 0.8 V. It is shown in Table 4.4 that the capacitance of the nickel foam in KOH solution is ten times lower than that of the silver plated nickel foam. Bultel *et al.* have shown by simulation how the decrease of the double layer capacitance leads to a shift in the frequency domain of the charge transfer arc towards higher frequencies. As a consequence, one semi-circle splits into two semi-circles, where the high frequency semi-circle is related to charge transfer and the low frequency semi-circle is related to diffusion [48]. As can be seen in Fig. 4.15, the trend is that the higher the polarization, the smaller the high-frequency semi-circle, this confirms that the high frequency semi-circle corresponds to the charge transfer resistance. The second (lower frequency) semi-circle remained almost unchanged; the source of this feature is not certain, but given its frequency range and the fact that the cell is being supplied with a large excess of reactant (in Fig. 4.14, the polarization curve for the cathode made of nickel does not show any mass transport limitation) it is proposed that the second semi-circle is due to diffusion processes. These features have been observed by other workers on similar electrodes in the same electrolyte [49]. As for the silver plated nickel foam cathodes, the inductive loop at low frequencies for cell polarisations between 0.2 and 0.6 V can be ascribed to the carbon support. The growth of the lower frequency loop for the cell polarisations of 0.7 and 0.8 V has been ascribed in the literature to reflect the water transport characteristics inside the pores of the electrodes [47, 50]. Further work is still required in order to fully characterise the EIS response from these cathodes, especially the water / electrolyte transport processes under working conditions.

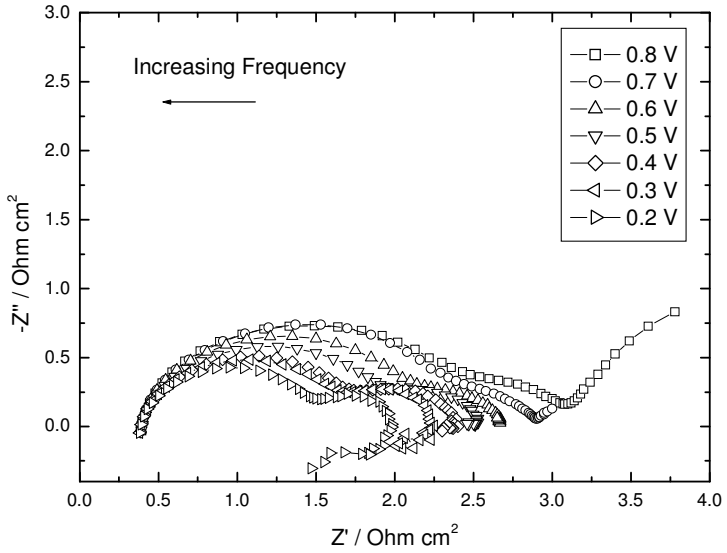


Figure 4.16: Impedance measurements over a range of electrode voltages of a cathode made of nickel foam under air at 25°C in 32 wt. % KOH solution from 10 kHz to 0.01 Hz.

The comparison of the impedance measurements made at 0.6 V (cell voltage) on the nickel foam cathode and silver plated nickel foam cathode is shown in Fig. 4.17. The high frequency semi-circle for the nickel foam cathode and the semi-circle of the silver plated nickel foam cathode ascribed to charge transfer. Because both impedance spectra are different, it is not possible to fit the entire frequency spectrum with the same equivalent circuit; however, the circuit shown in Fig. 4.5 was used to fit the high frequency semi-circle to determine Rs. The Ohmic resistance of the silver plated nickel foam cathode is smaller (7.9×10^{-2} Ω) than that of nickel foam cathode (9.3×10^{-2} Ω). The Ag coating is observed to significantly reduce the resistance to charge transfer and also the Ohmic resistance. The reason for this is still the subject of investigation, but it is speculated that it may be due to improved contact resistance between carbon particles and the coated nickel foam substrate, and/or a more uniform current distribution within the higher conductivity silver coated substrate.

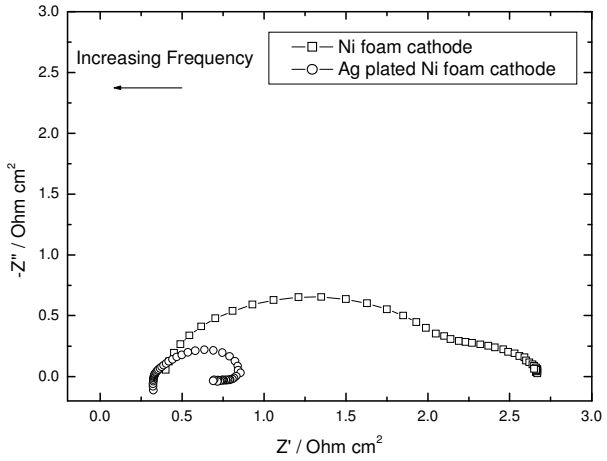


Figure 4.17: Comparison between the EIS response from the nickel foam and silver plated nickel foam based cathodes at 0.6 V (cell voltage) from 10 kHz to 0.01 Hz.

4.5. Conclusions

Nickel foam has been investigated as a potential electrode substrate for AFC electrodes because of its lower cost compared to the commonly used nickel mesh.

Both nickel foam and silver plated nickel foam have been characterized and results have been compared. In direct immersion in KOH solution, silver plated nickel foam showed a decrease in Ohmic and charge transfer resistance, and also an increase of the double layer capacitance compared to the uncoated nickel foam. The silver coating enhanced the catalytic activity of the uncoated nickel foam towards the oxygen reduction reaction.

Cathodes made of silver plated nickel foam showed enhanced performance compared to cathodes made of uncoated nickel foam due to the reduction of the Ohmic and charge transfer resistance. Silver plating leads to an increase in the surface roughness of the nickel foam. The form of impedance spectra of both cathodes are different; this is believed to be due to the silver layer which increases the double layer capacitance showing only one capacitive semi-circle instead of two for the uncoated nickel substrate.

4.6. References

[1] F. Bidault, D.J.L. Brett, P.H. Middleton, N.P. Brandon. J Power Sources 187 (2009) 39-48.

[2] B.B. Blizanac, P.N. Ross, N.M. Markovic. Electrochimica Acta 52 (2007) 2264-2271.

[3] M. Duerr, S. Gair, A. Cruden, J. McDonald. J Power Sources 171 (2007) 1023-1032.

[4] E. Gulzow, M. Schulze, U. Gerke. J Power Sources 156 (2006) 1-7.

[5] T. Hejze, J.O. Besenhard, K. Kordesch, M. Cifrain, R.R. Aronsson. J Power Sources 176 (2008) 1490-493.

[6] B.Y.S. Lin, D.W. Kirk, S.J. Thorpe. J Power Sources 161 (2006) 474-483.

[7] A. Verma, S. Basu. J Power Sources 168 (2007) 200-210.

[8] E. Gulzow. J Power Sources 61 (1996) 99-104.

[9] G.F. McLean, T. Niet, S. Prince-Richard, N. Djilali. Int J Hydrogen Energy 27 (2002) 507-526.

[10] M. Cifrain, K. Kordesch. Hydrogen/oxygen (Air) fuel cells with alkaline electrolytes. In: Vielstich W, Lamm A, Gasteiger HA, editors. Handbook of Fuel Cells. Chichester: John Wiley, 2003.p.267-280.

[11] M. Cifrain, K. Kordesch. J Power Sources 127 (2004) 234-242.

[12] K. Tomantschger, F. McClusky, L. Oporto, A. Reid, K. Kordesch. J Power Sources 18 (1986) 317-335.

[13] K.F. Blurton, E. McMullin. Energy Conversion 9 (1969) 141-144.

[14] S. Langlois. J Appl Electrochem 19 (1989) 51.

[15] S. Langlois. J Appl Electrochem 20 (1990) 740.

[16] S. Langlois. J Appl Electrochem 19 (1989) 43-50.

[17] M.S. Phanikumar, R.L. Mahajan. Int J Heat and Mass Transfer 45 (2002) 3781-3793.

[18] E.O. Vilar, F. Coeuret. Electrochimica Acta 40 (1995) 585-590.

[19] O.B. Olurin, D.S. Wilkinson, G.C. Weatherly, V. Paserin, J. Shu. Composites Sci and Tech 63 (2003) 2317-2329.

[20] V. Paserin. Advanced Eng Mater 6 (2004) 454.

[21] W. Metzger, R. Westfall, A. Hermann. Int J Hydrogen Energy 23 (1998) 1179-1183.

[22] Q.S. Song, G.K. Aravindaraj, H. Sultana, S.L.I. Chan. Electrochimica Acta 53 (2007) 1890-1896.

[23] W. Taucher-Mautner, K. Kordesch. J Power Sources 132 (2004) 275-281.

[24] D. Wang, C. Wang, C. Dai, D. Sun. Rare Metals 25 (2006) 47-50.

[25] D. Yan, W. Cui. J Alloys Compd 293 (1999) 780-783.

[26] A. Yuan, S. Cheng, J. Zhang, C. Cao. J Power Sources 77 (1999) 178-182.

[27] O. Smorygo, V. Mikutski, A. Leonov, A. Marukovich, Y. Vialiuha. Scripta Materialia In Press, Uncorrected Proof, 23.

[28] B. Yang, G. Yu, X. Liu. Electrochimica Acta 52 (2006) 1075-1081.

[29] Y.F. Guo, D. Ye, K. Chen, J. He. Catal Today 126 (2007) 328-337.

[30] Y. Tao, B. Zhu, Z. Chen. J Crystal Growth 293 (2006) 382-386.

[31] B. Yang, G. Yu, D. Shuai. Chemosphere 67 (2007) 1361-1367.

[32] H. He, H. Liu, F. Liu, K. Zhou. Surface and Coatings Tech 201 (2006) 958-964.

[33] T. Yuan, R. Li, K. Zhou. Transactions of Nonferrous Metals Society of China 17 (2007) 762-765.

[34] H.B. Dai, Y. Liang, P. Wang, H.M. Cheng. J Power Sources 177 (2008) 17-23.

[35] L. Yang, Z. Liu, J. Shi, H. Hu, W. Shangguan. Catalysis Today 126 (2007) 359-368.

[36] F. Chen, et al. Appl Surface Sci 253 (2007) 5155-5160.

[37] W. Yang, S. Yang, W. Sun, G. Sun, Q. Xin. J Power Sources 160 (2006) 420-424.

[38] W. Yang, S. Yang, W. Sun, G. Sun, Q. Xin. Electrochimica Acta 52 (2006) 9-14.

[39] N. Tassin, G. Bronoel, J.F. Fauvarque, I. Bispo-Fonseca. J Power Sources 65 (1997) 61-64.

[40] M. Chatenet, L. Genies-Bultel, M. Aurousseau. J Appl electrochem 32 (2002) 1131-1140.

[41] E. Herrero, L.J. Buller, H.D. Abruña. Chemical reviews 101 (2001) 1897-930.

[42] Y. Bonfil. Analytica Chimica Acta 464 (2002) 99.

[43] E. Kirowa-Eisner. Analytica Chimica Acta 385 (1999) 325.

[44] E. Kirowa-Eisner. J Electroanalytical Chem Inter Electrochem 552 (2003) 171.

[45] D. Thiele, A. Züttel. J Power Sources 183 (2008) 590-594.

[46] J.T. Müller, P.M. Urban, W.F. Hölderich. J Power Sources 84 (1999) 157-160.

[47] J.M. Song, S.Y. Cha, W.M. Lee. J Power Sources 94 (2001) 78-84.

[48] Y. Bultel, L. Genies, O. Antoine, P. Ozil, R. Durand. J Electroanal Chem 527 (2002) 143-155.

[49] F. Alcaide, E. Brillas, P.L. Cabot. J Electroanal Chem 547 (2003) 61-73.

[50] H. Huang, et al. J Colloid Interface Sci 284 (2005) 593-599.

Chapter 5: Effect of an additional active layer on cathode performance using nickel foam as a substrate material

5.1. Abstract

Improved performance was obtained by adding an extra active layer (AL) composed of manganese (IV) oxide (MnO_2) deposited onto carbon black. This new cathode design performed significantly better (130 mA cm^{-2} at 0.8 V and 25 ^oC) than the previous design (35 mA cm^{-2} under the same condition), especially at higher potential. It has been shown that the GDL is a key component of the gas diffusion electrode for both performance and durability, especially with liquid electrolytes. Electrochemical impedance spectroscopy was used to study the various losses in the cathode as a function of electrolyte concentration, oxygen concentration and cell voltage. The typical impedance spectra consisted of one high frequency depressed semi-circle which is believed to be related to porosity and KOH wettability, and one low frequency semi-circle related to electrode kinetics.

5.2. Introduction

This work builds on the previous chapter and shows how introduction of an extra active layer into the cathode electrode assembly can significantly improve electrochemical performance. The objective was to improve the activation area of the I-V curves shown in Chapter 4 by adding a catalysed active layer. MnO_2 was selected as the catalyst because of its excellent activity towards the disproportionation reaction of HO_2^- into O_2 and OH^-, and its low cost.

5.3. Experimental

5.3.1. Electrode Preparation

The electrode substrates used in this work were nickel foam (purity: 99.9%, pore per inch: 110, density: 380 g m^{-2}, average pore size: 590 μm, thickness: 1.7 mm) from INCO (Dalian) Co. Ltd.

Silver plating was carried out on 50×90 mm samples using a series of plating baths following the procedure already described in the previous chapter. The amount of deposited silver was 12 mg cm^{-2} and plating chemicals were provided by Balco Ltd (UK).

Gas diffusion layers (GDLs) were prepared with carbon black (Printex XE2 BET surface 950 m^2 g^{-1}, average primary particle size 35 nm) from Degussa, PTFE (TE3893-N solution 59.94% solid) from Alfa chemicals and propan-2-ol from VWR, by mixing and stirring until a homogeneous paste was obtained. The PTFE solution:carbon black ratio was 2.5:1.

An active layer (AL) was prepared with the same carbon black as that used for the GDL, using a PTFE dispersion as the bonding agent. Manganese (IV) oxide was deposited (loading ~ 15 mg cm^{-2}) by the impregnation method using manganese (II) nitrate solution (50% wt. %) in dilute nitric acid, followed by a thermal reduction during the sintering of the complete electrode. The mechanism of thermal decomposition of manganese nitrate in air has been comprehensively studied by Hussein et al [1]. According to this work, the precursor is converted to MnO_2 at 220^oC, after which it is quantitatively converted to Mn_2O_3 at 560^oC. Considering the temperature of the sintering (255^oC), MnO_2 is expected to be the major oxide formed.

To prepare each electrode, the silver plated foam (80×50 mm) was pressed to obtain a thickness of ~0.3 mm. The GDL mixture was rolled to 0.5 mm thickness with a calendering machine on grease-proof paper. The foam was put on top of the GDL and rolled to a thickness of 0.5 mm. The GDL was then cut to size. The active layer, which was rolled to a thickness of 0.2 mm, was then rolled onto the other side of the electrode as shown in Fig.5.1. Finally, the electrode was pressed at 20 bars for 2 minutes to remove excess liquid. The electrode was then sintered in air at 255$^{\circ}C$ for 30 min.

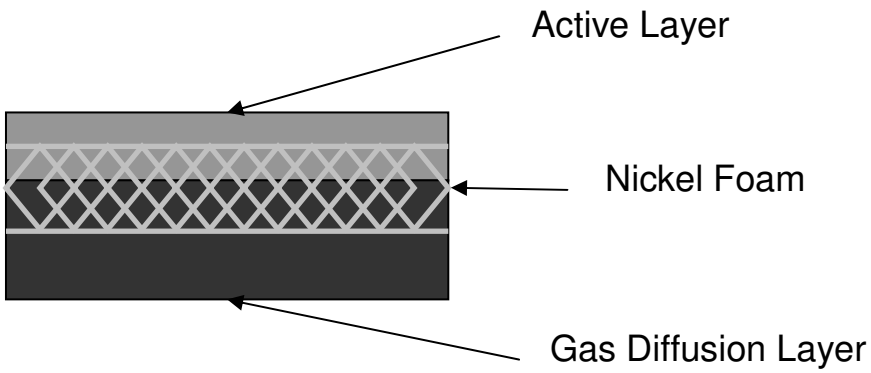


Figure 5.1: Scheme of the new cathode design using nickel foam as the substrate.

5.4. Results and discussion

5.4.1. Cathode performance and optimization

Table 5.1 summarises the formulation and performance of each of the cathodes developed in chapter 5 and 6.

Cathode Type	Substrate	GDL	AL	Typical Final Thickness (mm)	Current Density at 0.8 V (mA cm^{-2})
Cath0	nickel mesh	Porous PTFE	5 wt. % Pt on activated carbon black	0.5	35
Cath1	nickel foam	Mixture of PTFE dispersion and carbon black ratio 2.5:1	None	0.8	5
Cath2	Silver plated nickel foam	Mixture of PTFE dispersion and carbon black ratio 2.5:1	None	0.8	40
Cath3	Silver plated nickel foam	Mixture of PTFE dispersion and carbon black ratio 3:1	MnO_2 on carbon black	0.9	85
Cath4	Silver plated nickel foam	Mixture of PTFE dispersion and carbon black ratio 3:1	MnO_2 on carbon black	0.6	132

Fig. 5.2 shows the performance of the cathodes referred to as Cath0 and Cath2 at 25, 70 and 90°C under air in 30 wt. % KOH solution. Cath0 was made using nickel mesh as the backing material. The GDL was non-conductive and comprised porous PTFE, and the AL was 5 wt. % Pt on activated carbon black. Cath2 was developed with the aim of decreasing the cost of Cath0 by using nickel foam instead of nickel mesh, and by replacing platinum with a non-noble metal catalyst, i.e. manganese (IV) oxide. Not surprisingly the performance of both cathodes was improved by increasing electrolyte temperature due to the decrease in activation overpotential and increase in ionic conductivity and mobility of the electrolyte at the higher temperature. Cath0 outperformed Cath2 at high potential (from OCV to 0.8 V) over the range of temperatures tested, this is an indicator of the higher electrokinetic activity of Cath0 due to the presence of platinum (inset Fig. 5.2). At medium and low potential, Cath2 shows better performance due to the improved conductivity of the backing material and the higher porosity of the GDL, which avoided mass transport limitation, even at a current density as high as 1 A cm^{-2}. Cath2 performed relatively well with current densities of 260, 350, and 425 mA cm^{-2} (0.6 V) at 25, 70 and 90 °C respectively.

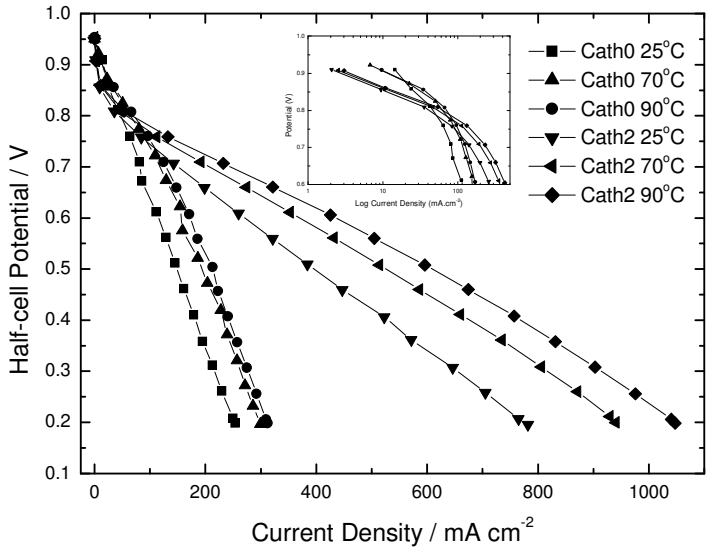


Figure 5.2: Polarization curves showing performance of Cath0 and Cath2 with air in 30 wt. % KOH solution at different temperatures. Inset: potential vs. log current density at high potential.

These results demonstrate that, even in the case of platinum (the most active catalyst known for the oxygen reduction reaction), a good electrode requires a number of characteristics to perform well, including good electrical conductivity to limit ohmic losses, and appropriate porosity in the GDL to avoid mass transport effects.

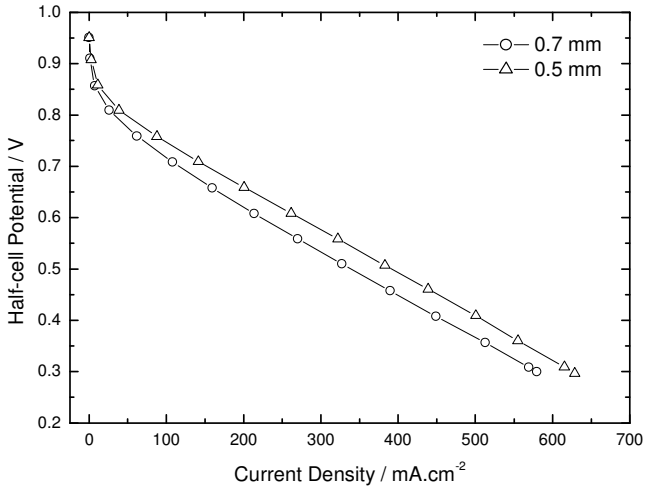


Figure 5.3: Polarization curves showing improved performance of Cath2 by optimization of the GDL thickness under air in 30 wt. % KOH solution.

Optimization of the electrode design must be performed to get the most from the catalyst loading, GDL thickness being a particularly important parameter. As can be seen in Fig. 5.3, increasing the thickness of the GDL from 0.5 to 0.7 mm decreased the electrode performance by decreasing the oxygen accessibility. It was found that a GDL thickness of 0.5 mm gives the best performance without incurring problems associated with electrolyte weeping.

The improvement of performance with different cathode generations is shown in Fig. 5.4. Cath1 and Cath2 were both made of nickel foam with the same GDL following the process described in the experimental section without the AL; only an extra layer of silver (12 mg cm^{-2}) onto the Cath2 foam differs. More details on Cath1 and Cath2 fabrication can be found elsewhere in the previous chapter. The increased electrical conductivity (by a factor 2), which improved the current collection, between Cath1 and Cath2 shows the importance of a conducting backing material for good performance.

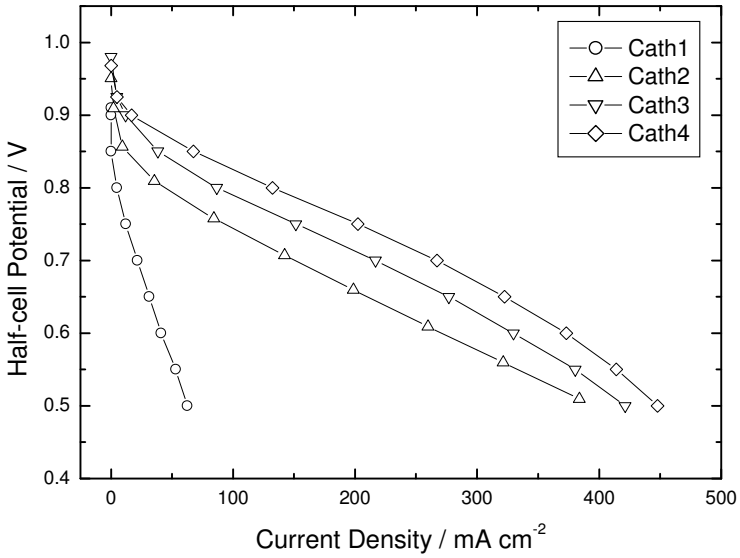


Figure 5.4: Polarization curves showing the improved performance of the different cathode generation under air at 25°C in 30 wt. % KOH solution.

Cath3 and Cath4 were made with the new cathode design which incorporates the extra active layer, leading to significantly improved performance. As can be seen, the new AL also influenced the shape of the polarisation curves, where Cath3 and Cath4 demonstrate a higher activity at high and medium potential but introduce a mass transfer limitation at low potential (starting at 0.6 V), whereas Cath2 does not exhibit this behaviour. From a fuel cell efficiency perspective, it is better to run the cell at higher potential so the new design with the extra active layer was deemed better that that of the Cath2 design. Cath4 contained the same GDL and AL as Cath3, but the thickness of the different layers was been optimized to give maximum power by performing a further rolling process on the finished electrode to get the desired thickness. As can be seen from the improved performance, the optimization exercise of the thickness plays an important role in maximising cathode performance.

Long term testing was then carried out on Cath3 by maintaining steady operation at 0.7 V (half cell potential) interspersed with polarisation curve runs. In each case the polarization measurements were taken five minutes after unloading the cell from the steady state value. The results are presented in Fig.5.5. After 50 hours Cath3 had fallen to almost 50% of the initial performance. Upon examination of the electrode after this time, drops of liquid electrolyte were seen on the rear of the GDL

corresponding to "weeping" through the GDL – a phenomena which has been observed many times with other electrode systems [36]. Weeping causes internal flooding of the pores in the GDL, severely limiting the diffusion of gas to the active layer. This type of degradation can be countered by increasing the hydrophobicity of the GDL and controlling the distribution of pore sizes. In this particular case, we opted to increase the hydrophobicity by increasing the PTFE dispersion/carbon black ratio from 2.5/1 to 3/1 in the GDL. A significant improvement in performance was then obtained. Even after 200 hours of continuous operation the performance was similar to the initial behaviour, at least down to 0.6 V. At lower potentials some mass transport limitation was evident, and therefore this operating regime should be avoided to reduce degradation.

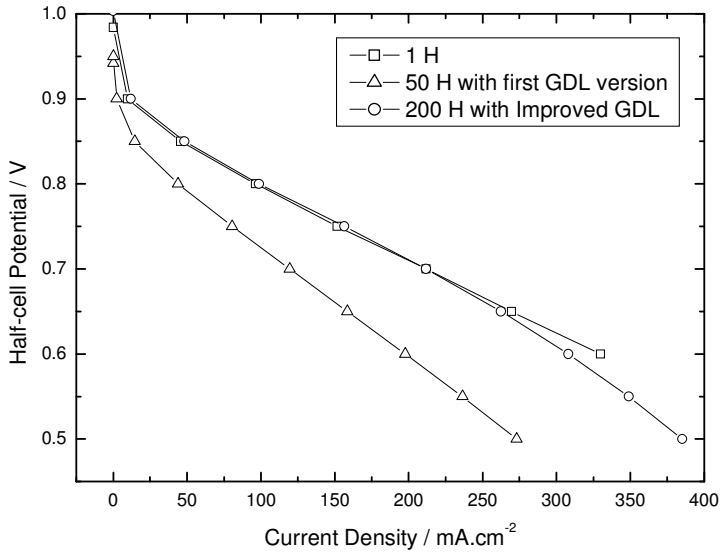


Figure 5.5: Polarization curves showing the performance of Cath3 after 1 and 50 hrs of operation as well as the operation of improved Cath3 containing a higher hydrophobic composition after 200 hours on air at 25°C in 30 wt. % KOH solution.

The ability to manufacture electrodes with high reproducibility and quality is important from a commercial perspective; Fig. 5.6 shows that the processing route developed here is appropriate for reproducible manufacture, showing the results from four cathodes produced at different times but fabricated using nominally the same procedure, especially given the fact that these fabrication procedures were operated on a batch rather than continuous basis.

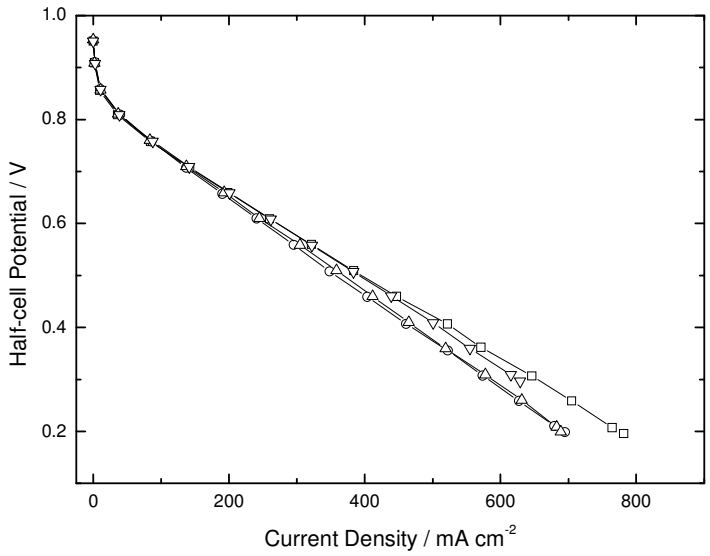


Figure 5.6: Polarization curves showing the performance of four different cathodes prepared using the same procedure under air at 20°C in 30 wt. % KOH solution.

5.4.2. Electrochemical impedance spectroscopy study

Electrochemical impedance spectroscopy measurements (EIS) were performed to resolve the various factors affecting the electrode performance of Cath4. Measurements were made in both air and pure oxygen and with varying electrolyte concentrations. The overall impedance results gave a depressed high frequency arc and a low frequency capacitive semi-circle.

Fig. 5.7 shows the impedance spectra of the cathode under air and oxygen at the same half cell voltage (0.9 V). It can be seen that the high frequency semi-circle is unchanged, whereas the low frequency feature is much smaller under pure oxygen. Fig. 5.8 shows the Bode plot spectra of the same cathode at different cell voltages. It can be seen that the high frequency semi-circle is again unchanged, whereas the size of the low frequency semi-circle decreases with increasing polarization. Both results demonstrate that the low frequency semi-circle is related to the oxygen reduction kinetics (including charge transfer and mass transport) whereas the high frequency feature seems to be related to the electrode structure (porosity).

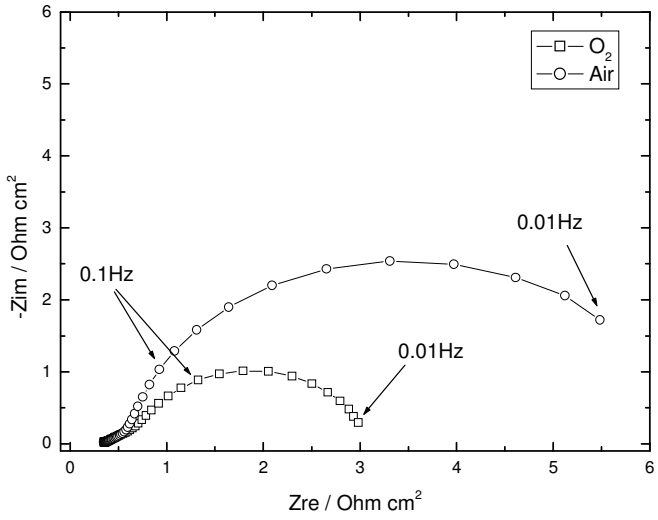


Figure 5.7: Impedance measurements of Cath4 under air and oxygen at 25°C in 30 wt. % KOH solution at 0.9 V (cell voltage) from 10 kHz to 0.01 Hz.

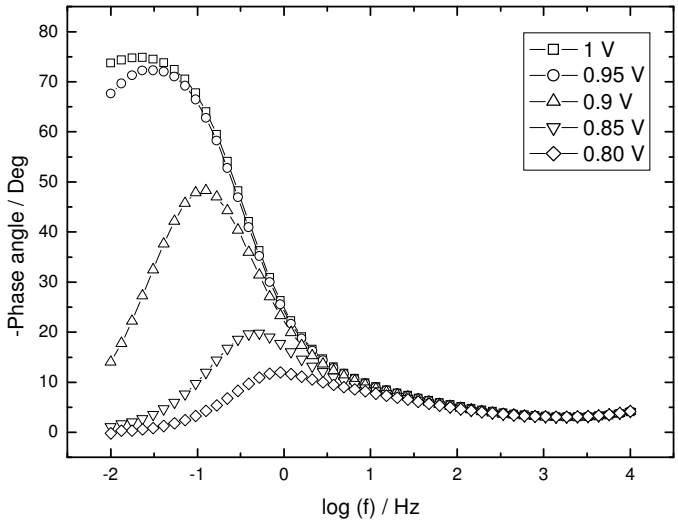


Figure 5.8: Impedance measurements of Cath4 under air at 25°C in 30 wt. % KOH solution at different cell voltages from 10 kHz to 0.01 Hz.

Impedance spectra of the same cathode in different KOH concentrations can be seen in Fig. 5.9. The low frequency arc increases in size when the KOH concentration increases. This could be due to the fact that, at higher concentration, KOH solution penetrates deeper in the AL structure which hinders the reactant gas accessibility increasing the mass transport resistance or due to the fact that oxygen solubility

decreases in KOH solution when KOH concentration increases (by a factor 4.5 between a 2 M KOH (10 wt.%) solution and 6.9 M KOH (30 wt.%) solution [2]).

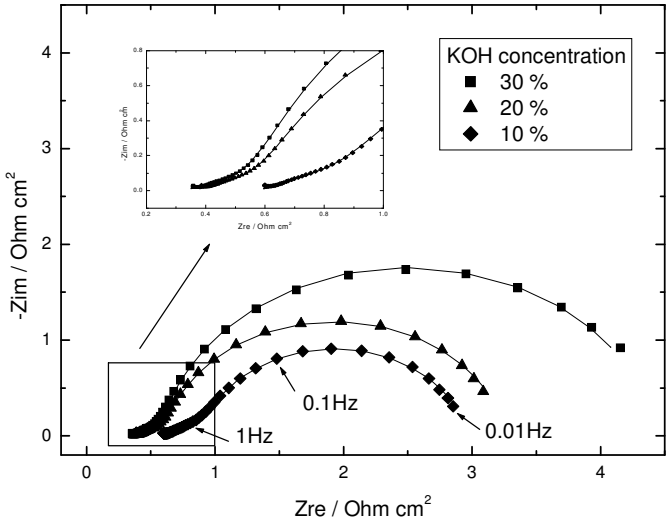


Figure 5.9: Impedance measurements of Cath4 under air at 25°C in different KOH concentration solutions at 0.9 V from 10 kHz to 0.01 Hz (symbol: experimental, line: fitting).

The equivalent circuit shown in Fig. 5.10 is then proposed to fit the Cath4 impedance spectrum where R_Ω is the sum of electrolyte resistance (bulk), contact resistances and cell resistances; R_1 is the ohmic drop resistance of the electrolyte in active pores (or flooded pores) which depends on electrode porosity and wettability, and R_2 is related to the oxygen reduction kinetics. Similar circuits have already been proposed in the case of cathode [3] and anode [4] in alkaline media. A constant phase element (CPE) is introduced, in place of a simple capacitor, because the semi-circles show some depression which relates to the current distribution within the electrode structure [5].

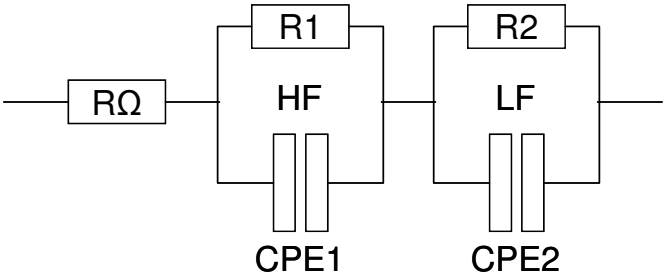


Figure 5.10: Equivalent circuit used to fit the high and low frequency semi-circles observed for Cath4.

As can be seen in Table 5.2, R_Ω decreases when the KOH solution concentration increases (which is in accordance with the predicted increase of the electrolyte conductivity with the concentration: increase of a factor ~ 1.6 between a 2 M KOH solution and 6.9 M KOH solution [6]) which was expected because R_Ω represents the ohmic resistances of the electrolyte and the cell. Surprisingly, R_1 appears to decrease with the increase of the electrolyte concentration. If R_1 was only a structural (physical) related resistance, it should stay constant which is obviously not the case. The admittance of the constant phase element (Y_1), representing the double-layer, also increases when the KOH concentration increases; this could again be due to the deeper KOH penetration in the electrode structure with higher KOH electrolyte concentration solutions. The low value of the parameter *n* of the CPE suggests that the electrode consists of semi-infinite pores [7] and is in agreement with porosity effects [8]. In a similar way, R_2 increases with the KOH concentration which could be due again to the deeper KOH penetration in the AL structure which hinders gas accessibility.

KOH Concentration (wt. %)	R_Ω (mΩ)	R_1 (mΩ)	Y_1 (F)	n_1	R_2 (mΩ)	Y_2 (F)	n_2
30	81	343	7.75	0.25	850	4.41	0.97
20	88	303	6.98	0.27	553	4.85	0.98
10	144	248	4.23	0.34	401	5.54	0.98

Table 5.2: Fitted values of equivalent circuit parameters of the Cath4 impedance spectra in different KOH concentration.

5.5. Conclusion

A new electrode design has been developed and studied for the oxygen reduction cathode in an alkaline fuel cell which exhibited a considerable improvement over previous designs. The addition of an extra active layer, comprising an MnO_2 catalyst supported on carbon black, significantly improved the cathode performance especially at high potential (130 mA cm^{-2} at 25 ^oC at 0.8 V under air as compared to 35 mA cm^{-2} for the previous design under the same conditions). A final cathode thickness optimization (0.6 mm) was carried out to maximise fuel cell performance. Electrochemical impedance spectroscopy study was performed on the latest electrode design showing one high frequency depressed semi-circle which is believed to be related to porosity and KOH wettability and one low frequency semi-circle related to kinetics. This insight allows us to link directly electrode micro and macrostructure to its kinetics which is very interesting for further cathode development.

5.6. References

[1] A.K.H. Nohman, H.M. Ismail, G.A.M Hussein. J Analytical and Applied Pyrolysis 34 (1995) 265-78.

[2] D. Tromans. Hydrometallurgy 50 (1998) 279-96.

[3] D. Thiele, A. Züttel. J Power Sources 183 (2008) 590-94.

[4] P.L. Cabot, F. Alcaide, E. Brillas. J Electroanal Chem 626 (2009) 183-91.

[5] A. Lasia. J Electroanal Chem 397(1995) 27-33.

[6] R.J. Gilliam, J.W. Graydon, D.W. Kirk, S.J. Thorpe. Inter J Hydrogen Energy 32 (2007) 359-64.

[7] R. de Levie. Electrochimica Acta 9 (1964) 231-45.

[8] H. Keiser, K.D. Beccu, M.A. Electrochimica Acta 21 (1976) 539-43.

Chapter 6: A Novel Cathode for Alkaline Fuel Cells based on a Porous Silver Membrane

6.1. Abstract

Porous silver membranes were investigated as potential substrates for alkaline fuel cell cathodes and as an approach for studying pore-size effects in alkaline fuel cells. The silver membrane provides both the electrocatalytic function, mechanical support and a means of current collection. Relatively high active surface area (~ 0.6 m^2 g^{-1}) results in good electrochemical performance (~200 mA cm^{-2} at 0.6 V and ~400 mA cm^{-2} at 0.4 V) in the presence of 6.9 M KOH. The electrode fabrication technique is described and polarisation curves and impedance measurements are used to investigate the performance. The regular structure of the electrodes allows parametric studies of the performance of electrodes as a function of pore size. Impedance spectra have been fitted with a proposed equivalent circuit which was obtained following the study of impedance measurements under different experimental conditions (electrolyte concentration, oxygen concentration and, temperature, pore size). The typical impedance spectra consisted of one high frequency depressed semi-circle related to porosity and KOH wettability and one low frequency semi-circle related to kinetics. A passive air-breathing hydrogen-air fuel cell constructed from the membranes in which they act as mechanical support, current collector and electrocatalyst achieves a peak power density of 50 mW cm^{-2} at 0.40 V cell potential when operating at 25^{o}C.

6.2. Introduction

Silver has the highest electrical conductivity of any element and is approximately 100 times less expensive than platinum. Moreover, silver is one of the most active catalysts for the oxygen reduction reaction (ORR), even competitive to Pt in high concentration alkaline media [1-3]. Oxygen cathodes loaded with Ag have also shown a longer lifetime over Pt based cathodes (3 years compare to 1 year for Pt) under practical chlor-alkali electrolysis conditions [4]. The impregnation of Ag onto carbon support via the *in situ* reduction of $AgNO_3$ has been shown to produce very fine

catalyst particles, resulting in high surface area required catalyst for optimal cathode performance [5]. Another way to obtain high surface area silver catalyst is the Raney approach, which involves leaching aluminium out of a 50% aluminium/50 % silver alloy using KOH [6].

The properties of silver present opportunities for the development of new electrode designs. In the previous chapters and in published work it has been shown how silver plated nickel foam can be used as an effective electrode substrate [7]. The silver plated foam provided improved current collection compared to bare nickel foam; however, the catalytic activity was limited due to the low surface area of the open cell structure of the foam.

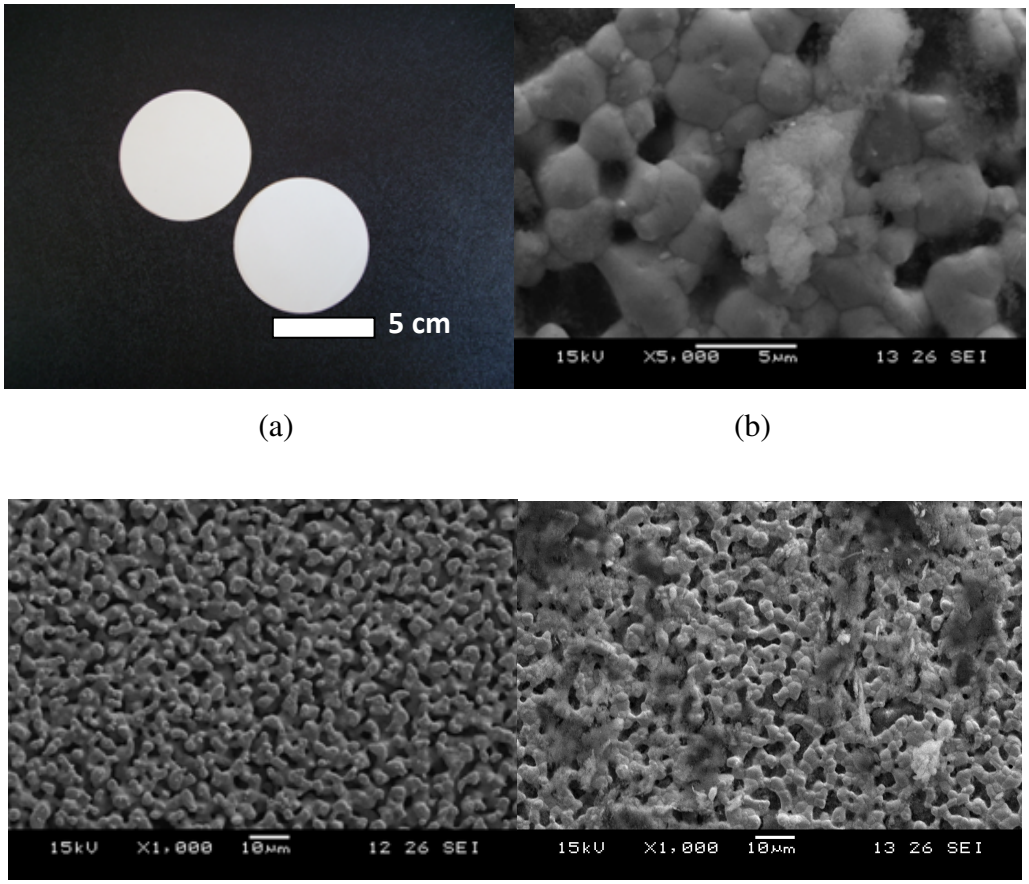
Porous silver membranes are mainly used in a variety of filtration applications where the antimicrobial and antibacterial properties of silver make silver membranes a very efficient filtration system [8-12]. Silver membranes are available with small pore size (micron range) and high porosity, resulting in high surface area structures. These properties are particularly useful in AFCs in which silver membranes can provide catalyst, mechanical support and a means of improved current collection compared to nickel mesh (silver having the highest electrical and thermal conductivity of all metals). Porous silver membranes offer the potential for a new cathode design that does not use a carbon support. This is beneficial since the commonly used carbon supports degrade in alkaline media, so affecting fuel cell lifetime.

The aim of this work is to investigate a new cathode design for AFCs that is based on a silver membrane. The high surface area of the membrane and the catalytic activity of the silver are a promising combination for high performance. Furthermore, the ability to obtain membranes with uniform pore sizes for a range of different pores sizes allows parametric studies of pore size on other important parameters. To our knowledge, its use in fuel cells has not been investigated.

6.3. Experimental

6.3.1. Electrode preparation

Silver metal membranes from Sterlitech (Purity: 99.97%, of 50 μm nominal thickness) were used as cathode substrates, Fig. 6.1. The pore size of the membranes ranges from 0.2 to 5.0 μm.



(a) (b)

(c) (d)

Figure 6.1: a) Optical Image of silver membranes; Scanning electron microscope image showing the porous structure of silver membranes without (c) and with PTFE (b) and (d).

Hydrophobization of the membranes was achieved using polytetrafluoroethylene (PTFE) solution (60 wt. % dispersion in water) from Sigma Aldrich which was applied by pipette directly onto one side of the membrane. The PTFE deposition was applied in a two step process. In the first PTFE deposition, a loading is applied that penetrates into the membrane body, this is allowed to dry at room temperature. In the second PTFE deposition, a second amount of PTFE is applied to the membrane, but this second amount does not penetrate into the membrane but stays on the membrane surface. The electrode was then sintered in air at 320 °C for 30 min. For membranes with pore size smaller than 0.8 μm, it was found that the PTFE during the first deposition did not tend to enter the structure and remained on the surface forming a non-porous layer after sintering. It was necessary to remove this compliant film covering the membrane in order to allow gas access to the silver membrane.

6.3.2. Electrode characterization

The surface of the silver membranes was analysed using a scanning electron microscope (JEOL JSM-5610LV).

The catalytic activity of the various silver membranes were measured in a half-cell configuration using a three electrode set-up and a Luggin capillary situated less than 0.5 mm from the electrode surface and a counter electrode of nickel foam which was 10 times the geometrical surface area of the working electrode, to avoid excessive polarization. Silver membrane cathodes (1 cm^2) were floated on the surface of a fresh KOH solution with the other side exposed to an oxygen or air atmosphere through forced convection [13]. Cathodes were polarised after 15 min in contact with the electrolyte under oxygen in a first scan (0.01 V s^{-1}) from OCV (1.1 V) to 0.1 V for conditioning. All polarization curves shown are the results of a second scan. A third scan was then taken (not shown here) to make sure that the optimum performance was obtained. Impedance spectra were then taken at 0.8 V, still under oxygen. Finally, measurements were taken under air.

6.3.3. Fuel cell operation

Cathodes were tested in a cylindrical 4 cm^2 hydrogen-air fuel cell utilising 25 mm diameter silver membrane disks as mechanical support, current collector and catalyst.

The fuel cell was constructed using a commercial hydrogen reformate anode from Alfa Aesar (Johnson Matthey Company, 0.4 mg cm^{-2} Pt, Toray paper GDL) separated with a plastic mesh (1 mm thick). Current was collected around the edge of the silver membrane disk, requiring that the current from the centre of the disk flowed >1 cm to the external current collector. The KOH solution was 30 wt. %, pure hydrogen (99.999%) from BOC was provided on the anode side whereas the cathode side was left open to the laboratory air in self-breathing mode without any supplemental gas flow. As the cathode was open to the laboratory air, no back pressure control was possible. Utilising optimised PTFE loading, the fuel cell did not show any weeping of electrolyte on the cathode side. Fuel cell results are not iR corrected.

6.4. Results and discussion

6.4.1. Characterization of silver membranes

Table 6.1 summarizes results of different measurements made on the different silver membranes. The particle retention characteristic is taken from the manufacturer's data sheet, and may be broadly considered to be close to the pore diameter. The porosity was calculated by weighing a known geometric volume of membrane knowing the density of pure silver. The specific surface area calculated using Eq. 6.1 relates to an estimation of the surface area considering only the inside of each pore which is assumed to be a long cylinder (tortuosity = 1) where P is the membrane porosity, ρ the silver density and r the radius of the cylinder. It can be seen that silver membranes with 0.2 and 0.8 μm have the highest estimated surface area and therefore should give the best performance. This model provides only an approximate assessment of the specific surface area as clearly the tortuosity of the membranes is greater than one, Fig. 6.1.

$$A = \frac{2P}{\rho r(1-P)} \qquad \text{Eq. 6.1}$$

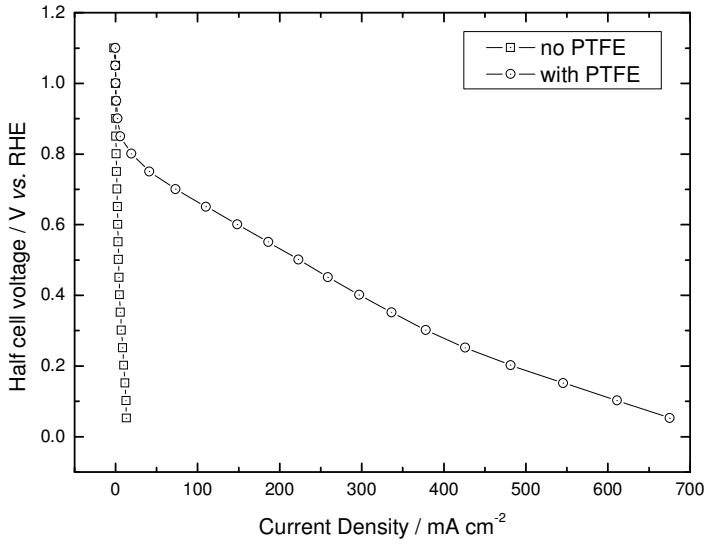
Particle retention / µm	Thickness / µm	Porosity / %	Specific surface area / $m^2 g^{-1}$
0.2	57	26.1	0.67
0.45	57	33.6	0.43
0.8	85	54.2	0.56
1.2	83	56.4	0.41
3	95	56.8	0.17
5	92	51.2	0.08

Table 6.1: Key characteristics of silver membranes.

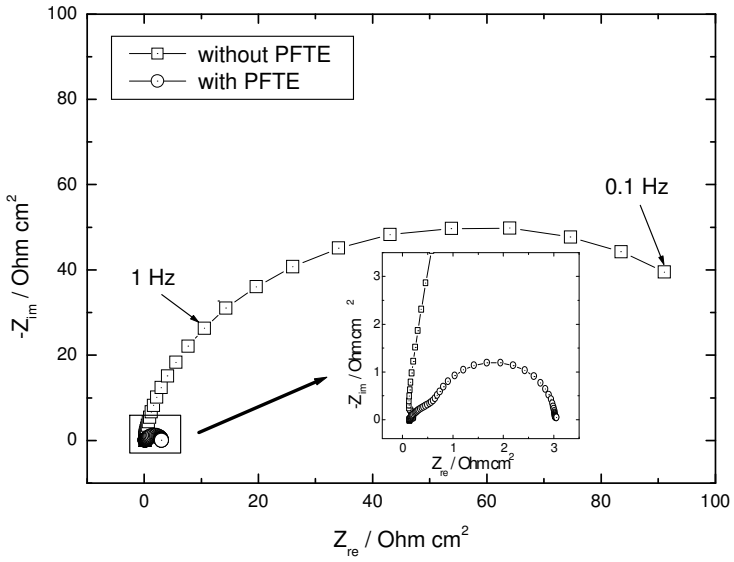
SEM images of the silver membrane surface (0.8 µm) before and after PTFE deposition are shown in Fig. 6.1. As can be seen in Fig. 6.1(a), the porosity of the membrane appears to be homogeneous with pores in the micron range. In Fig. 6.1(b), an excess of PTFE can be seen in the centre of the picture with smaller particles in the membrane pores.

6.4.2. Characterization of silver membranes cathodes

A silver membrane (1.2 µm) cathode was prepared with a PTFE coating following the procedure described in the experimental section. The half cell polarization curves of a cathode with PTFE and a cathode without PTFE coating under oxygen clearly demonstrate the importance of the PTFE coating to obtain good performance (Fig. 6.2(a)).



(a)



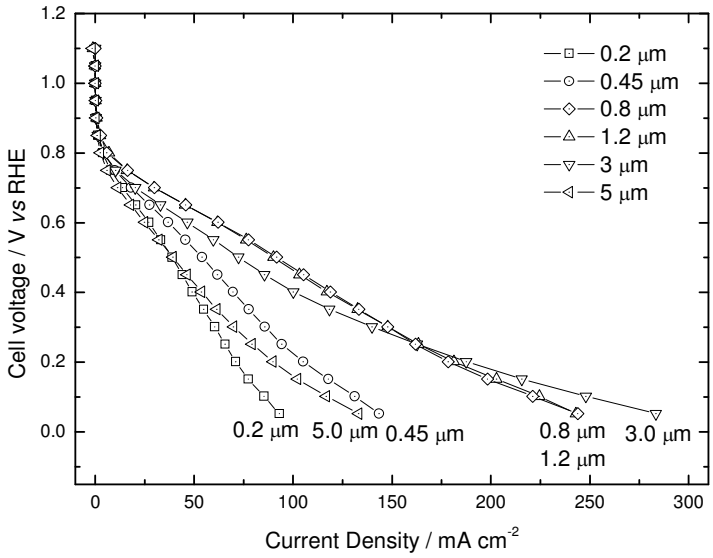
(b)

Figure 6.2: Polarization curves and impedance results for cathodes made of silver membrane (1.2 μm) with and without PTFE (12.3 mg cm^{-2} total amount deposited) under oxygen at 20°C in 30 wt. % KOH solution. (a). Polarisation results; (b) Impedance measurements at 0.8 V (cell voltage) from 10 kHz to 0.1 Hz. Inset is the same plot scaled to show the details of the scans at low Z.

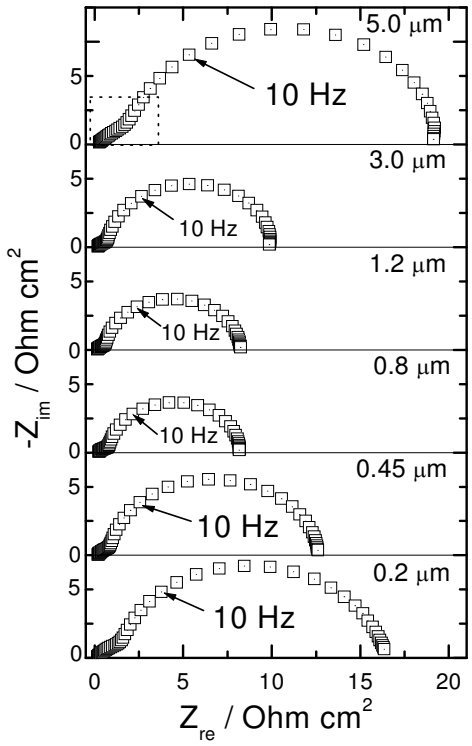
Impedance measurements were performed on cathodes prepared with and without PTFE (Fig.6.2 (b)). As can be seen, the cathode without PTFE exhibits a single large capacitive arc whereas the cathodes made with PTFE (Fig.2 (b) inset) shows a depressed arc at high frequency and a capacitive semi-circle at low frequency which are much smaller than for the cathode without PTFE. It is believed that the structure of the cathode without PTFE is completely flooded with electrolyte, making the mass transport resistance very high. The PTFE coating keeps the gas side of the electrode free of KOH solution which greatly improves the reactant gas accessibility, so decreasing the mass transport resistance.

The same PTFE treatment was applied to silver membranes with different pore sizes with a target PTFE loading of 13 mg cm^{-2}, and the resulting polarization curves and impedance results are shown in Fig. 6.3. As can be seen for the polarisation results, Fig. 6.3(a), the best performance was obtained for silver membranes with 0.8 and 1.2 μm pore size. The difference in surface area is obviously part of the reason for the improvement in performance for these electrodes but more importantly the PTFE loading seems to be important for optimizing performance (see below).

Impedance measurements were performed on these cathodes, the results of which are shown in Fig. 6.3(b). All the cathodes share the same impedance spectra features, with a depressed high frequency arc and a low frequency capacitive semi-circle. The decrease in size of the low frequency semi-circle on membranes with pore sizes between 0.2 and 1.2 μm is believed to be due to the increase in PTFE loading whereas its increase in size with membrane between 1.2 and 5 μm pore size is believed to be related to the decrease in surface area since the PTFE loading is similar for these cathodes. The best performing cathodes (0.8 and 1.2 μm) show the smallest low frequency semi-circle which is believed to be due to the fact that 0.8 and 1.2 μm pore size are both optimal if considering surface area and PTFE.



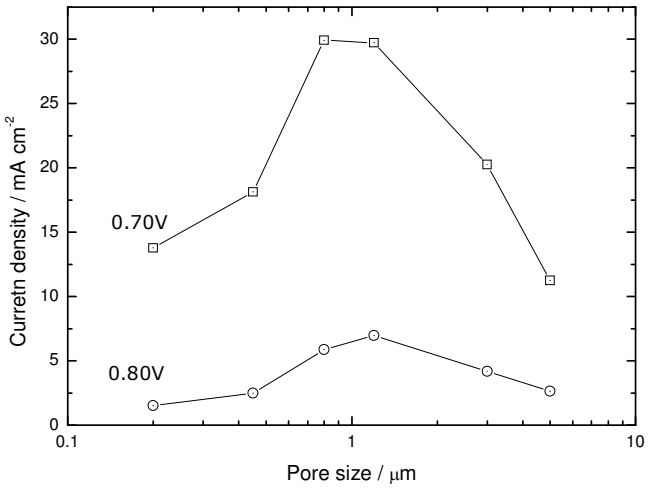
(a)



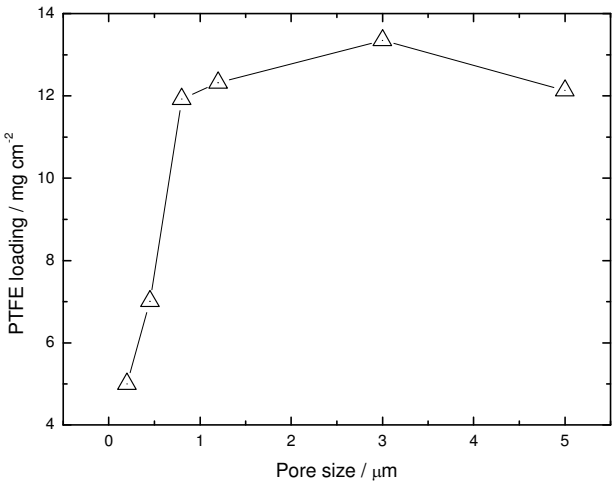
(b)

Figure 6.3: Polarization curves (a) and impedance measurements (b) of cathodes made of silver membranes with different pore sizes under air at 20°C in 30 wt. % KOH solution at 0.8V.

Indicative performance of the cathodes at two relevant potentials (0.70 V, 0.80 V) extracted from Fig. 6.3(a) is shown in Fig. 6.4(a). An improvement in performance with decreasing pore size is seen down to a pore size of 0.8 μm, although for smaller pores, there is a decrease in performance. As pore size decreases, the specific surface area of the membrane tends to increase (Table 6.1), and so we might expect performance to be highest for the smallest pore size, however this is not the case. Even though a consistent application technique was used, it was found that the PTFE loading for the different membranes was not the same, Fig. 6.4(b). Apparently, the inferior results from membranes with 0.2 and 0.45 μm pore sizes (Fig. 6.4(a)) can be explained by the poor PTFE loading after the hydrophobization step (see Experimental section). This could be due to the fact that the 0.2 and 0.45 μm membranes would have pores too small to allow PTFE particle infiltration, preventing the formation of hydrophobic areas within the membrane. It is to be noted that improved performance for the 0.2 and 0.45 μm membranes compared to the 0.8 and 1.2 μm membranes would be expected because of the increase in specific surface area were it possible to obtain a suitable PTFE coating.



(a)

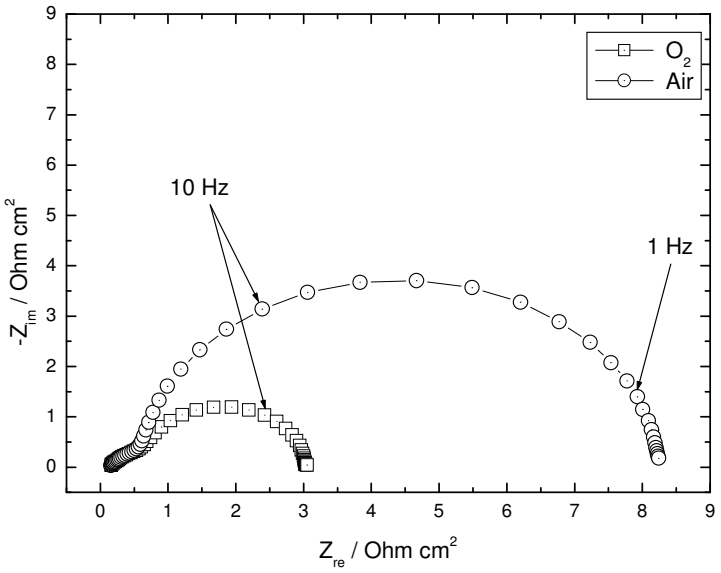


(b)

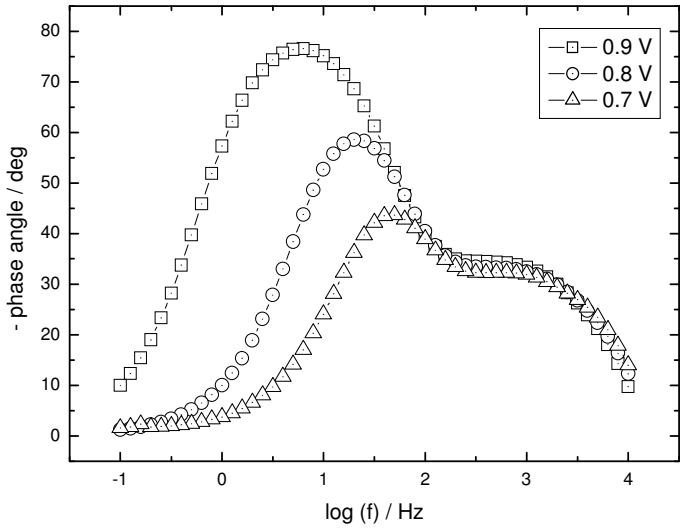
Figure 6.4: Current density at 0.70 and 0.80 V (a) [Data taken from Fig. 6.3(a)]; and PTFE loading (b) as a function of membrane pore size for a consistently applied PTFE treatment.

6.4.3. Assessment of performance under different conditions

In order to attribute physical significance to the features observed in the impedance spectra, measurements were taken under different experimental conditions using a 1.2 μm pore size silver membrane cathode (total PTFE loading: 12.3 mg cm^{-2}). Fig. 6.5(a) shows the impedance spectra of the cathode under air and oxygen at the same half cell voltage (0.8 V). It can be seen that the high frequency semi-circle is unchanged, whereas the low frequency feature is much smaller under pure oxygen. Fig. 6.5(b) shows the Bode phase-plot spectra of the same cathode at different cell voltages in an oxygen atmosphere. It can be seen that the high frequency semi-circle is again unchanged, whereas the size of the low frequency semi-circle decreases when increasing the polarization. Both results demonstrate that the low frequency semi-circle is related to kinetics (included charge transfer and mass transport) whereas the high frequency one seems to be related to the electrode structure (porosity).



(a)



(b)

Figure 6.5: Impedance measurements of silver membrane cathode (1.2 μm) at 20°C in 30 wt. % KOH solution from 10 kHz to 0.1 Hz. (a) Nyquist plot at 0.8 V showing the effect of reactant - oxygen and air ; (b) Bode phase-plot spectra under oxygen showing the effect of polarisation potential.

Impedance spectra of the same cathode were obtained in different KOH concentration (Fig.6.6). The low frequency arc increases in size when the KOH concentration increases. This could be due to the fact that at higher concentration KOH solution penetrates deeper into the membrane structure which hinders the reactant gas accessibility increasing the mass transport resistance.

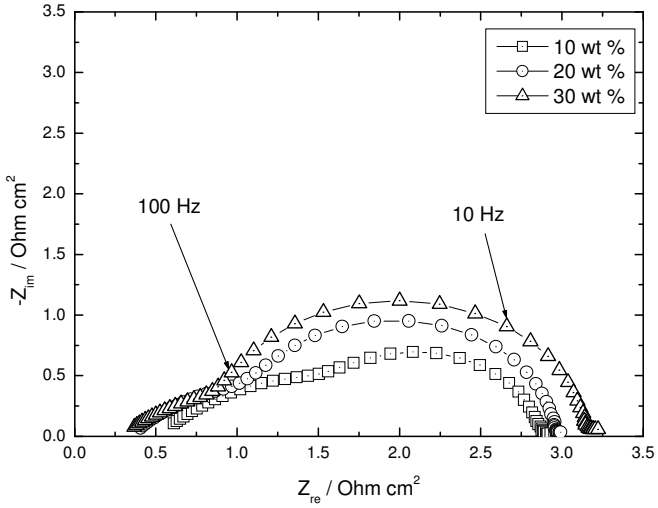


Figure 6.6: Impedance measurements of silver membrane cathode (1.2 μm) under oxygen at 20°C in different KOH concentration solutions at 0.8 V (cell voltage) from 10 kHz to 0.1 Hz.

R_Ω and the first constant phase element from equivalent circuit shown in Fig. 6.7 was used to fit the high frequency semi-circles.

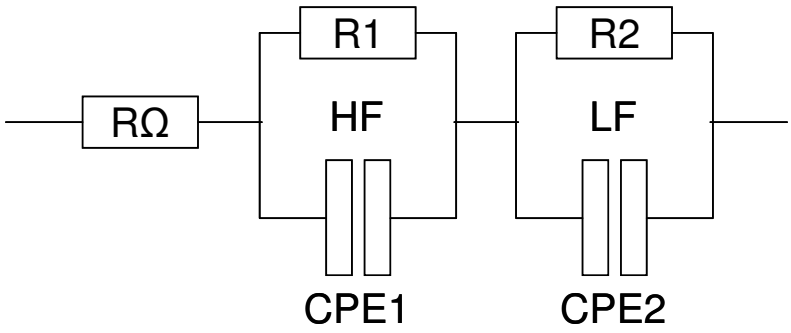


Figure 6.7: Equivalent circuit of the silver membrane cathode used to fit both the high frequency and low semi-circles.

A constant phase element (CPE) is introduced because the semi-circles show some depression which relates to the lack of homogeneity of the electrode capacitance [14]. The impedance of a constant phase element is given by:

$$Z_{CPE} = \frac{1}{Yo(j\omega)^n} \qquad \text{Eq. 6.2}$$

Where Y_0 is the admittance relating to the double layer capacitance and n is a constant between -1 and 1 giving information about the nature of the CPE. When n=1, Y_0 corresponds to the ideal capacitance C and the CPE behaves as a capacitance.

As can be seen in Table 6.2, R_Ω decreases when the KOH solution concentration increases (increase of the electrolyte conductivity) which was expected because R_Ω represents the Ohmic resistances of the electrolyte in the cell. Surprisingly, R_1 appears to decrease with the increase of the electrolyte concentration. If R_1 was only a structural (physical) related resistance, it should stay constant which is obviously not the case. The admittance of the constant phase element, representing the double-layer, also increases when the KOH concentration increases; this could again be due to the deeper KOH penetration into the electrode structure with greater KOH concentration. The low value of the parameter n (~ 0.5) suggests that the electrode consists of semi-infinite pores [15] and is in agreement with porosity effects [16].

KOH Concentration / %	R_Ω **(Ω)**	R_1 **(Ω)**	CPE_1	
			Y_1 (F)	n
10	0.516	2.14	1.14	0.56
20	0.342	1.96	1.63	0.56
30	0.290	1.77	2.32	0.52

Table 6.2: Fitted values of equivalent circuit parameters of the high frequency semi-circle for silver membrane cathode in different KOH concentration.

Impedance spectra of the same cathode were obtained at constant KOH concentration but different temperatures (Fig. 6.8). The low frequency semi-circle decreased when the temperature increased, which is expected since it is related to kinetics. The high frequency semi-circle also decreased when the electrolyte temperature increased. From both electrolyte concentration and temperature dependence studies, we can conclude that R_1 is strongly related to the electrolyte conductivity.

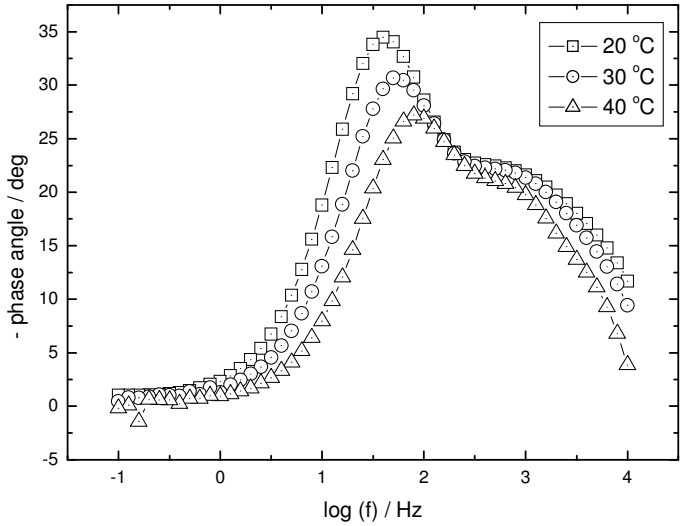


Figure 6.8: Bode plot spectrum of silver membrane cathode (1.2 μm) under oxygen at different temperature in 30 wt. % KOH solution at 0.8 V (cell voltage) from 10 kHz to 0.1 Hz.

The equivalent circuit shown in Fig. 6.7 is then proposed to fit the silver membrane cathodes impedance spectrum where R_Ω is the sum of electrolyte resistance (bulk), contact resistances and cell resistances; R_1 is the ohmic drop resistance of the electrolyte in active pores (or flooded pores) which depends on electrode porosity and wettability and finally R_2 is related to kinetics. Similar circuits have already been proposed in the case of cathode [17] and anode [18] in alkaline media.

6.4.4. Optimisation of PTFE loading

As described in the experimental section, PTFE was deposited twice on the membranes. In the first step, the PTFE dispersion penetrates throughout the entire membrane volume. In the second deposition step, the PTFE is only deposited on the surface of the membrane. The ability to tailor the PTFE distribution both within the membrane and on the membrane surface is crucial to obtaining good performance. A cartoon of the expected resultant configuration, in which a greater loading of PTFE is on the surface than in the body of the silver membrane is shown in Fig.6. 9.

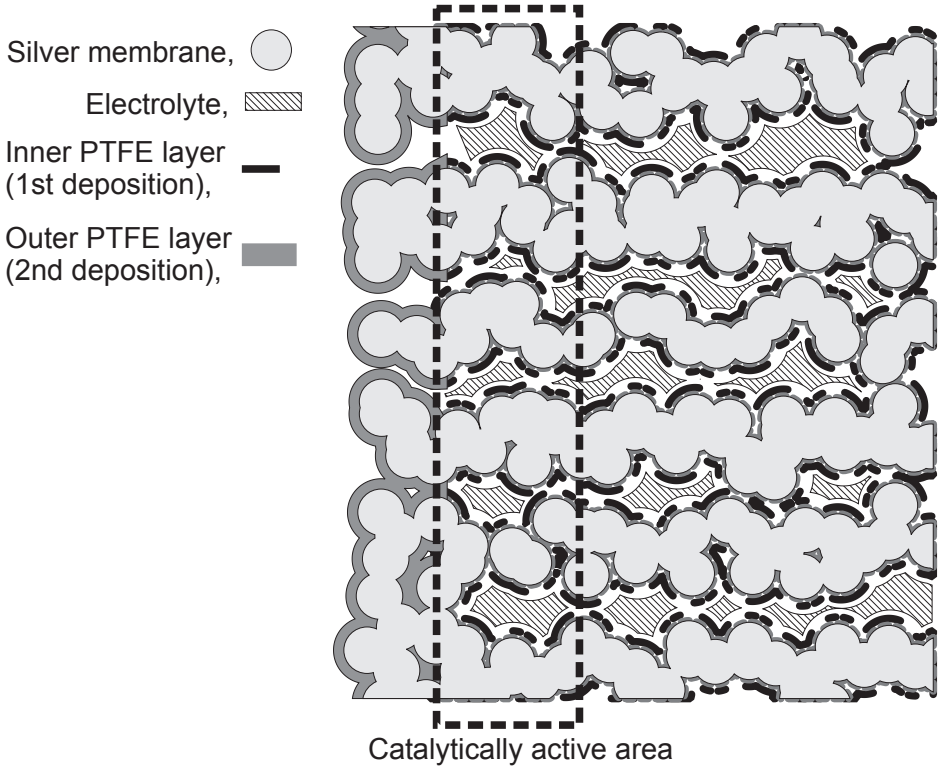
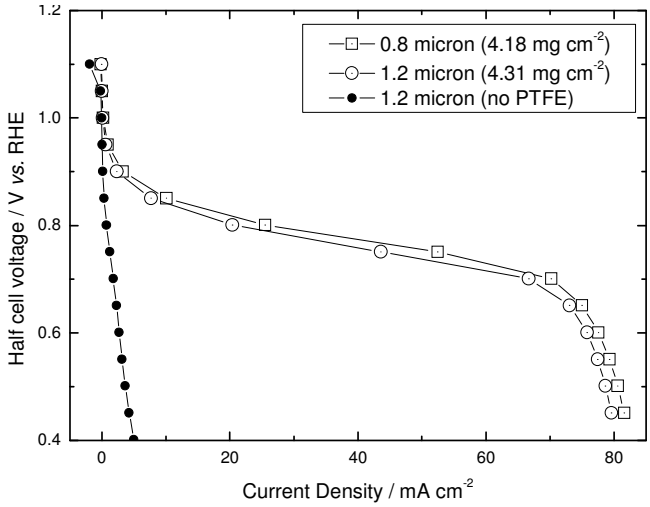


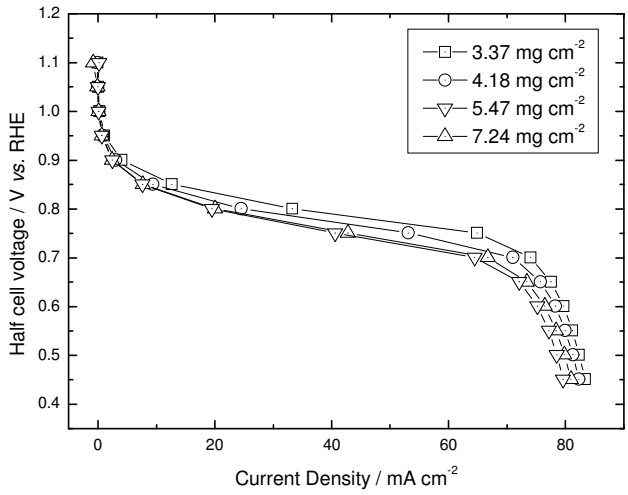
Figure 6.9: Cartoon showing the deposition of PTFE on the silver membrane and how this may affect wetting of the electrolyte. The first PTFE layer is deposited throughout the entire membrane structure whereas the second deposition occurs only on the surface. The catalytically active area immediately beneath the outer PTFE layer is highlighted.

In order to study this effect, we initially measured the performance of the two best performing membranes from Fig. 6.3(a) (0.8 μm, 1.2 μm) after only the ***first PTFE deposition*** with a loading of around 4 mg cm^{-2}, Fig. 6.10(a). The benefit of including this PTFE treatment is clearly seen for the 1.2 μm membrane compared to the same membrane with no PTFE. The cathode made with 0.8 μm pore size outperforms the one made with 1.2 μm pore size for the same PTFE loading. It is also clear why the second PTFE deposition step is important, as in its absence a significant mass transport limitation is seen at current densities of j>70 mA cm^{-2}.

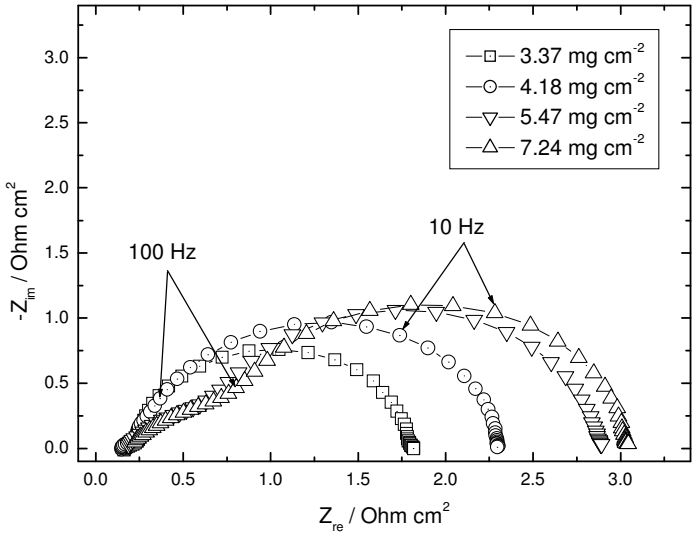
In order to optimise the first PTFE deposition step we looked at the performance of the 0.8 μm pore size silver membrane as a function of the PTFE loading in the first step, Fig 6.10(b). In order to assess only the effect of PTFE loading within the membrane, the second PTFE deposition (i.e. deposition of PTFE on the membrane surface) was not performed. For this reason the performance at high current density (j>70 mA cm^{-2}) is poor. As can be seen in Fig. 6.10(b), although PTFE is required in the inner structure its loading should be kept low because performance decreases when the PTFE loading is increased. As expected, the size and shape of the high frequency semi circle change with PTFE loading. It is more marked with higher PTFE loadings (Fig. 6.10(c)).



(a)



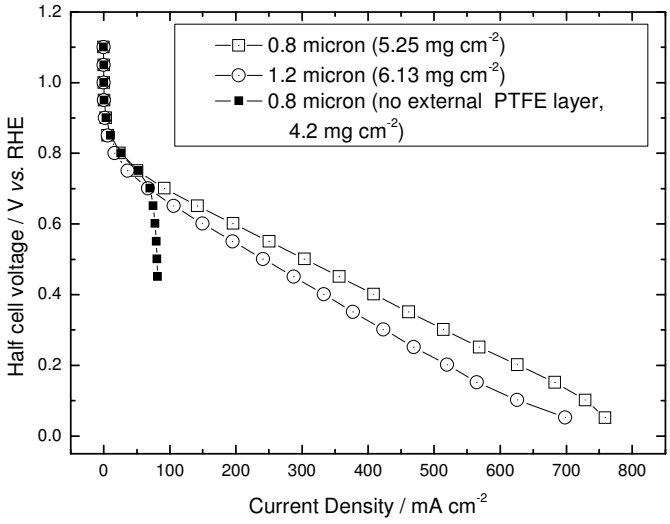
(b)



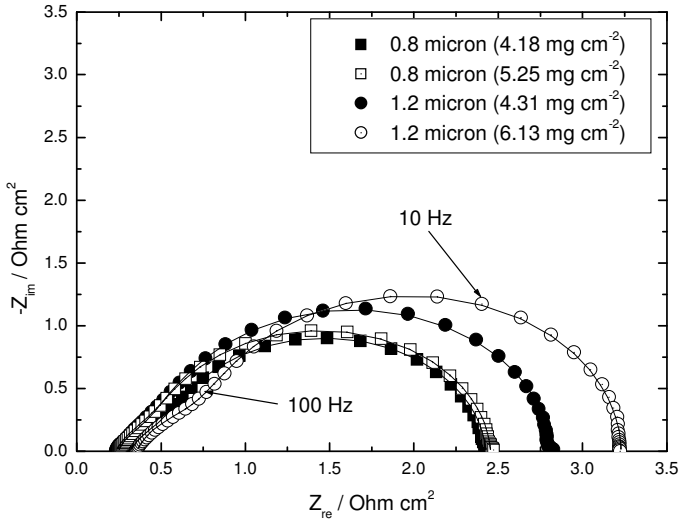
(c)

Figure 6.10: Effect of first PTFE deposition step on silver membrane performance under oxygen at 20°C in 30 wt. % KOH solution. No second PTFE deposition step was performed. (a) Polarization curve showing pore size effect for constant PTFE loading from the first deposition step (b) Polarization curves for 0.8 µm silver membranes showing the effect of the PTFE loading from the first deposition step; (c) impedance spectra for the membranes in (b) obtained at 0.8 V (cell voltage) from 10 kHz to 0.1 Hz.

Having determined the optimum first loading value (i.e. the amount of PTFE dispersed throughout the entire membrane volume), we also optimised the second PTFE amount (i.e. the amount of PTFE deposited on the membrane surface). Fig. 6.11(a) shows the resultant polarisation curves for two different pore size membranes (0.8 μm and 1.2 μm) utilising a first PTFE loading of 4.2±0.1 mg cm^{-2}. The PTFE loading displayed in Fig. 6.9 is the total PTFE loading (i.e. first+second PTFE loading). The effect of the second PTFE treatment is to remove the mass transport limitation seen at about 80 mA cm^{-2} for electrodes which only have the first (internal) PTFE treatment. Performance of the 0.8 μm cathodes are quite good with 196 mA cm^{-2} at 0.6 V and 408 mA cm^{-2} at 0.4 V, considering the fact that it is a very simple electrode design.



(a)



(b)

Figure 6.11: Performance of silver membranes after optimised first and second PTFE deposition steps. Polarization curves showing optimised 0.8 µm and 1.2 µm pore electrodes and for comparison a 0.8 µm pore size electrode with only the optimised first ptfe loading, (a). Electrochemical impedance results for cathodes made of silver membranes (0.8 and 1.2 µm) under oxygen at 20°C in 30 wt. % KOH solution, (b). Impedance data obtained at 0.8 V, from 10 kHz to 0.1 Hz (symbol: experimental data, line: fit). Total PTFE loadings are displayed for each electrode (first PTFE deposition step leads to a loading of 4.2±0.1 mg cm^{-2}).

In Fig. 6.11(b), impedance measurements of the same cathodes can be seen. The experimental data (symbols) are well fitted (lines) with the equivalent circuit shown in Fig. 6.7. Results are summarized in Table 6.3. The double-layer capacities of porous electrodes are proportional to their wetted areas. Y_1 (larger than Y_2) would be representative of the total flooded area of the cathode, whereas Y_2 would be representative of the catalytic active surface area of the cathode which is believed to be located just below the PTFE coating as seen in Fig. 6.7. It can be seen that the higher the PTFE loading, the lower Y_1. This is expected because less electrolyte floods the electrode structure which means a decrease of the double-layer capacitance. The PTFE loading does not have much effect on Y_2 and R_2 for both pore size cathodes because these parameters are related to the active surface area which is

believed to vary mostly with the structure of the membrane (pore size, roughness of the surface, etc.) but not much with the penetration depth of the PTFE (or loading) in the pore (considering the pore as a long cylinder).

Electrode Pore size / μm	PTFE Loading / mg cm^{-2}	R_Ω (Ω)	R_1 (Ω)	CPE_1		R_2 (Ω)	CPE_2	
				Y_1 (F)	n_1		Y_2 (F)	n_2
0.8	4.18	0.321	0.255	1.10	0.78	1.849	0.627	0.96
0.8	5.25	0.248	0.238	0.985	0.81	1.968	0.627	0.97
1.2	4.31	0.233	0.322	0.982	0.77	2.254	0.458	0.98
1.2	6.13	0.358	0.471	0.553	0.80	2.399	0.476	0.99

Table 6.3: Fitted values of equivalent circuit parameters (Fig. 6.6) for curves in Fig. 6.11(b).

In the same way, R_1 and R_2 are lower (Y_1 and Y_2 are higher) for the 0.8 μm pore size cathode than for the 1.2 μm case. This is because the surface area of the 0.8 μm cathode is higher than that of the 1.2 μm cathode. This increases the surface of the membrane in contact with the electrolyte decreasing R_1 and R_2 and increasing Y_1 and Y_2.

The double-layer capacitances were estimated by the means of Eq. 6.3 [18,19] using data listed in Table 6.3. Results of Eq. 6.2 and Eq. 6.3 are shown in Table 6.4 where it can be seen that the surface area of the 0.8 μm pore size electrode is higher than the 1.2 μm pore size electrode; this explains the superior performance for the 0.8 μm electrode. It is interesting to note that both results are in good accordance.

$$C_{dl} = \left(\frac{C_2}{\left((R_\Omega + R_1)^{-1} + R_2^{-1} \right)^{(1-n_2)}} \right)^{1/n_2} \qquad \text{Eq. 6.3}$$

Silver membrane pore size / μm	Estimated surface area / m^2 g^{-1}	Estimated double-layer capacitance / F cm^{-2}
0.8	0.56	0.60
1.2	0.41	0.47

Table 6.4: Estimates of the electrode surface area and double layer capacitance from Impedance data in Fig. 6.11.

In order to study the stability of the cathode ten successive polarization scans have been performed (after the 3 first scans) following immediately after by impedance measurement at 0.8 V. A decay of current density at different voltages was observed as can be seen from Fig.6.12 . The current density at each voltage decreased with the number of scan; the higher the polarization the higher the decrease in current density.

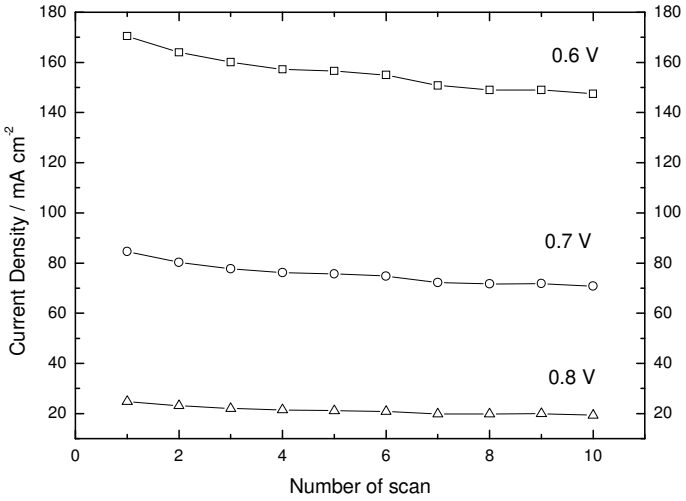


Figure 6.12: Current density decay at different half cell voltages of a cathode made of silver membrane (0.8 μm, PTFE: 5.25 mg cm^{-2}) under oxygen at 20°C in 30 wt. % KOH solution.

The equivalent circuit shown in Fig.6.8 was used to fit the impedance spectra obtained after each scan (Fig.6.13). R_Ω and R_1 increased slightly with the number of scans whereas Y_2 was relatively stable. R_2 and Y_1 increased significantly with scan number. The increase in Y_1 is believed to be due to increased flooding of the membrane structure. This hinders gas accessibility increasing mass transport resistance which can be related to the increase in R_2. This flooding or weeping effect is well known in liquid alkaline systems and is one of the main reasons for cathode performance degradation [8]. In future work we will test this cathode design with an anionic membrane as in this case no movement of the electrolyte interface is seen, and a stable three-phase contact region is formed.

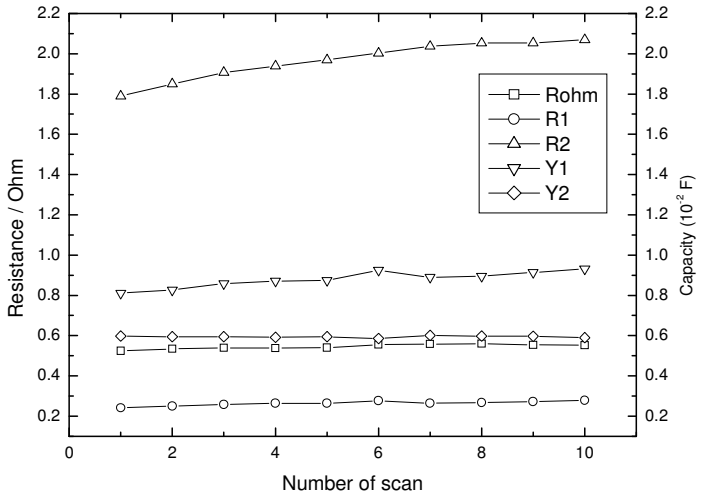
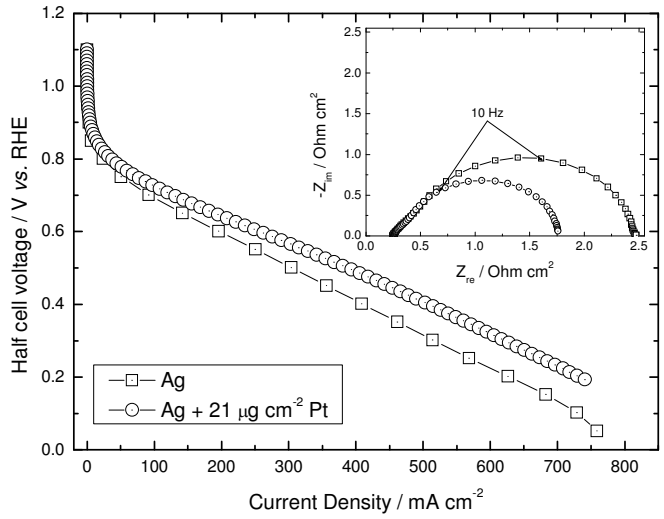


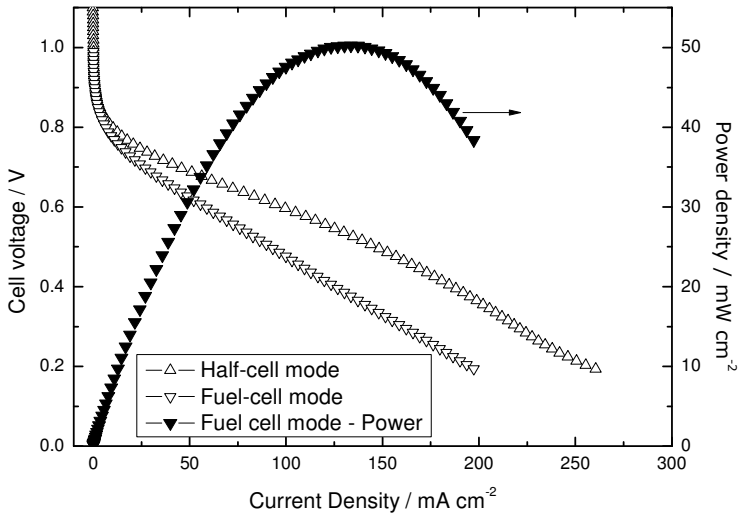
Figure 6.13: Equivalent circuit parameters fitted from impedance measurement of a silver membrane cathode (0.8 μm, PTFE: 5.25 mg cm^{-2}) under oxygen at 20°C in 30 wt. % KOH solution from 10 kHz to 0.1 Hz.

6.4.5. Testing membranes within a fuel cell

In order to improve the activity of the electrode, 10 nm of Pt was sputtered on one side of a 0.8 μm silver membrane, equivalent to a loading of 21 μg cm^{-2}, followed by the standard PTFE treatment. Two different cathodes were fabricated: in one of them the Pt coating was on the gas side and in the other the Pt coating was on the electrolyte side of the membrane. Only the cathode with the Pt coating on the gas side showed an improved performance meaning that most of the electrode structure is flooded with electrolyte and the thickness of the membrane could be greatly reduce without any effects on cathode performance. The performance of the membrane with Pt on the gas side is shown in Fig. 6.14(a). A clear improvement can be seen with a performance of 260 mA cm^{-2} at 0.6 V and 500 mA cm^{-2} at 0.4 V. In the low current regime, 0.1 mA cm^{-2} – 100 mA cm^{-2}, where the potential is dominated by electrokinetics, a 30 mV positive shift in the curve is seen. At higher current densities the improvement in performance is even greater, suggesting that mass transport to the Pt Layer is enhanced compared to transport to the silver electrode. This is to be expected if the platinum layer is immediately below the outer PTFE layer.



(a)



(b)

Figure 6.14: (a) Half-cell polarization curves of cathodes made of silver membrane (0.8 μm) and silver membrane with 10 nm of Pt (20 μg cm^{-2}) under oxygen at 20 °C. Inset – Electrochemical Impedance spectroscopy of each electrode at 0.90 V from 10 kHz to 0.1 Hz. (b) Hydrogen-air fuel cell test of silver membrane with 10 nm of Pt (21 μg cm^{-2}) utilising 30 wt. % KOH solution as electrolyte and 1 mm electrode separation. Pt on carbon paper (0.4 mg cm^{-2}) used as anode. For comparison, the same cathode operating under half-cell operation in the same cell is shown.

The improvement in performance is assumed to be due to the higher catalytic activity of Pt compared to Ag. This was confirmed by electrochemical impedance spectroscopy (Fig. 6.14(a), inset) for which only the low frequency kinetic semi-circle was seen to reduce in size when Pt was introduced onto the cathode. Tafel analysis of the polarization curves in the kinetic region (E>0.8V) gives a slope of 105 mV dec^{-1} for Ag and 93 mV dec^{-1} for the Pt on Ag electrode.

Testing of the new cathode in a 4 cm^2 cylindrical hydrogen-air fuel cell was also performed to see if good results could be obtained utilising the silver membrane (0.8 μm pore size) with 10 nm of Pt (21 μg cm^{-2}) as cathode. Under these conditions the silver membrane functions as both mechanical support, sole current collector (>1 cm maximum current path), and electrocatalyst. We were able to show good performance of the fuel cell utilising our optimised PTFE loading with the cathode open to the air, (i.e. without any back-pressure), and without weeping of the electrolyte through the cathode membrane. For comparison, the cathode was also tested potentiostatically in the same cell and under the same conditions (passive air breathing mode). As can be seen from Fig. 6.14(b), performance of the fuel cell is slightly reduced compared to the results obtained in the half-cell configuration, yet still attain a peak power of 50 mW cm^{-2} at a cell voltage of 0.4 V under passive self-breathing operation. This is an impressive performance considering that no backpressure or forced air convection is applied, and the cathode is open to the laboratory air. The reduction in performance compared to the half-cell results could be explained by the presence of the spacer between the cathode and the anode. Comparison of impedance spectra (not shown) did not show any increase in Ohmic resistance between the half-cell and fuel cell mode but an increase in the low-frequency kinetic semi-circle. This could be due to the higher resistance to species (H_2O, OH^-) to migrate from anode to cathode induced by the spacer (since there was no difference in air flow rate or electrode structure).

The silver loading of the new cathode design (using a membrane with 0.8 μm pores) is estimated at 45 mg cm^{-2}. Such a loading has been used before in test cathodes for alkaline fuel cells. For instance, Wagner et al. utilised 0.4 mm thick electrodes with a silver loading of greater than 47 mg cm^{-2} to study the longevity of electrode performance [20]. In our case the electrodes are only ~85 μm thick, $^1/_5{}^{th}$ of those mentioned above. This reduction of thickness may be beneficial for the transport

properties of gases. Indeed, we estimate that the membranes could be reduced to maybe 20 μm thickness whilst retaining mechanical stability. In such a case, the loading would be reduced by a factor of 4 with a total cost of 100 $ m^{-2} for combined electrocatalyst + current collector + mechanical support which is not far away from the cost of nickel mesh alone (60 $ m^{-2}) in the conventional design – to which would still have to be added the cost of the electrocatalyst.

6.5. Conclusion

Porous silver membranes, which are commonly used as filter membranes in diverse chemical processes, have been successfully demonstrated as substrates for fuel cell cathodes in alkaline media. These membranes are useful as they have a consistent structure which allows parametric analysis of a wide range of variables whilst keeping the general structure of the electrode constant. Hence it has been possible to test pore size effects in a way which is much more difficult to achieve using standard electrodes. A treatment process, consisting of the application of PTFE dispersion both within and on one side of the electrode, is necessary to obtain good electrochemical performance. The PTFE loading has been optimized to get optimal results from the porous silver structure in a two steps process which is necessary to avoid any mass transportation limitation. The membrane with 0.8 μm pore size appeared to be the more adequate for high performance because of its high surface area. Performance obtained are quite good with 196 mA cm^{-2} at 0.6 V and 408 mA cm^{-2} at 0.4 V and with 260 mA cm^{-2} at 0.6 V and 500 mA cm^{-2} at 0.4 V under oxygen using a very thin (10 nm) Pt coating on top of the Ag. Utilised in passive air-breathing mode, a hydrogen air fuel cell utilising the above-mentioned platinum on silver cathode attains a power density of 50 mW cm^{-2} at a cell potential of 0.4 V utilising the silver membrane also as mechanical support and current collector.

6.6. References

[1] B.B. Blizanac, P.N. Ross, N.M. Markovic. Electrochimica Acta 52 (2007) 2264-2271.

[2] M. Chatenet, L. Genies-Bultel, M. Aurousseau. J Applied Electrochem. 32 (2002) 1131-1140.

[3] V. Hacker, E. Wallnofer, W. Baumgartner, T. Schaffer, J.O. Besenhard, H. Schrottner, M. Schmied. Electrochem. Comm. 7 (2005) 377-382.

[4] N. Furuya, H. Aikawa. Electrochimica Acta 45 (2000) 4251-4256.

[5] K. Smrcek, J. Beran, J. Jandera. J Power Sources 2 (1978) 273-286.

[6] M. Al-Saleh. J Applied Electrochem. 24 (1994) 575-580.

[7] F. Bidault, D.J.L. Brett, P. H. Middleton, N. Abson, N, N.P. Brandon. Int J Hydrogen Energy 34 (2009) 6799-6808.

[8] O. Akhavan, E. Ghaderi. Current Applied Physics In Press, Accepted Manuscript.

[9] S.A. Glazier. J Microbiological Methods 20 (1994) 23.

[10] Y. Lv, H. Liu, Z. Wang, S. Liu, L. Hao, Y. Sang, D. Liu, J. Wang, R.I. Boughton. J Membrane Science 331 (2009) 50-56.

[11] A. Pérez Padilla. Desalination 114 (1997) 203.

[12] I. Sondi, B. Salopek-Sondi. J Colloid and Interface Science 275 (2004) 177-182.

[13] S. Srinivasan. Fuel Cells: From Fundamentals to Applications, Springer, 2006, pp.692.

[14] A. Lasia. J Electroanalytical Chem. 397 (1995) 27-33.

[15] R. de Levie. Electrochimica Acta 9 (1964) 1231-1245.

[16] H. Keiser, K.D. Beccu, M.A. Gutjahr. Electrochimica Acta 21 (1976) 539-543.

[17] D. Thiele, A. Züttel. J Power Sources 183 (2008) 590-594.

[18] P.-L. Cabot, F. Alcaide, E. Brillas. J Electroanalytical Chem. 626 (2009) 183-191.

[19] J. Kubisztal, A. Budniok, A. Lasia. Int. J. Hydrogen Energy 32 (2007) 1211-1218.

[20] N. Wagner, M. Schulze, E. Gulzow. J Power Sources 127 (2004) 264-272.

Chapter 7: Conclusions and future work

Fuel cells have a great potential in reducing CO_2 emissions for a greener future. Their commercial success will depend mostly in their cost reduction. Alkaline Fuel cells appears to have inherent advantages which could lead to mass production and low cost compared to other fuel cell types. This work has demonstrated how the use of a new kind of electrode substrate could lead to new AFC designs and in turn cost reduction, while maintaining acceptable performance.

Nickel foam has been investigated as a potential electrode substrate for AFC electrodes because of its lower cost compared to the commonly used nickel mesh. Both nickel foam and silver plated nickel foam have been characterized and used as electrode substrate. Cathodes made of silver plated nickel foam showed enhanced performance compared to cathodes made of uncoated nickel foam due to the reduction of the Ohmic and charge transfer resistance.

A new electrode design has been developed and studied for the oxygen reduction cathode in an alkaline fuel cell which exhibited a considerable improvement over previous designs. The addition of an extra active layer, comprising a MnO_2 catalyst supported on carbon black, significantly improved the cathode performance, especially at high potential. Electrochemical impedance spectroscopy was performed on the latest electrode design showing one high frequency depressed semi-circle which is believed to be related to porosity and KOH wettability and one low frequency semi-circle related to kinetics.

Porous silver membranes have been successfully demonstrated as substrates for fuel cell cathodes in alkaline media. A treatment process, consisting of the application of PTFE dispersion both within and on one side of the electrode, is necessary to obtain good electrochemical performance. Utilised in passive air-breathing mode, a hydrogen-air fuel cell attained a power density of 50 mW cm^{-2} at a cell potential of 0.4 V utilising the silver membrane as both mechanical support and current collector.

If we compare performance between the cathode developed with nickel foam as substrate material (chapter 5) and the cathode developed with the porous silver membrane (chapter 6), it is clear that the cathode made of nickel foam outperforms the cathode made of silver membrane (at 0.6 V under air at 25°C, 80 mA cm^{-2} for silver membrane cathode and 375 mA cm^{-2} for the nickel foam cathode). More interestingly, both systems gives similar impedance spectra which can be modelled by the same equivalent circuit (Fig.6.7) where R_Ω is the sum of electrolyte resistance (bulk), contact resistances and cell resistances; R_1 is the ohmic drop resistance of the electrolyte in active pores (or flooded pores) which depends on electrode porosity and wettability and finally R_2 is related to kinetics. This could lead to a better understanding of the more complex system (nickel foam cathode) knowing exactly what are the effects of structural properties on the much simpler one (silver membrane cathode) helping the improvement of performance.

Comparing performance from the literature to the silver membrane cathode developed in this study, the only system close enough is the work by Wagner et al. (Reference 20 in Chapter 6) where pure silver powders are mixed with PTFE. They obtained almost 900 mA cm^{-2} at 0.6V, well above the 200 mA cm^{-2} at 0.6V of our system, but it ust be noted that the temperature of the electrolyte was at 70°C (compared to 20°C in this case), and that the curve presented in their work is Ir-drop corrected which is not the case for our work. Finally, it has to be noted that the use of very fine silver powder would give a much larger surface area compared to the system used in this study.

Concerning the nickel foam cathode, the closest system found is the one described in Yang et al (Reference 153 chapter 2) where MnO_2 on carbon black is used as the catalyst and nickel foam is used as the current collector. At 0.6V, they obtained 200 mA cm^{-2} for a static electrolyte with a mixture of carbon nanotube/carbon black, and only 90 mA cm^{-2} when using only carbon black as the catalyst support. This is a lot less than has been reported in this study for cath4 at the same potential (375 mA cm^{-2} with circulation of the electrolyte, and 650 mA cm^{-2} with a static electrolyte as shown in Fig 3.4 chapter 3). But it has to be noted that in this study the catalyst loading is 5 times more greater than their catalyst loading.

Recommendations for future work

- Porous silver membrane cathodes:

  - Use different PTFE suspension (with smaller particle size) in order to see if better performance with smaller pore size than 0.8 μm can be obtained.
  - Study/model with EIS the effect of electrolyte penetration in the cathode structure on performance and try to link with the nickel foam cathode behaviour.

- Nickel foam cathodes:

  - Optimization of MnO_2 loading
  - Try to use carbon nanotubes in the active layer
  - Study the catalytic activity of different carbon blacks toward ORR, trying to link performance to the physical characteristics such as surface area, porosity and chemical composition of the surface.
  - Study the electrolyte circulation effect on cathode performance, and how to better control where the reaction occurs to maximise the TPB and reduce degradation due to weeping effects.

The development of liquid electrolyte systems has been shown to have advantages which could open the way to the commercialization of the alkaline fuel cell technology. However, leakage, parasitic power losses, CO_2 poisoning and degradation due to weeping are problems which are inherent to the liquid electrolyte form. These problems could be overcome by using an alkaline anion-exchange membrane which combines advantages of AFCs and advantages related to the solid form electrolyte. In future work, it will also be interesting to try cathodes developed in this thesis with these alkaline membranes.